POLITECNICO
MILANO 1863

SCUOLA DI INGEGNERIA INDUSTRIALE
E DELL'INFORMAZIONE

A probabilistic algorithm for the survivability analysis of an upper stage vehicle reentering into the Earth's atmosphere

Tesi di Laurea Magistrale in
Space Engineering - Ingegneria Spaziale

Author: **Alessio Barzaghi**

Student ID: 841741
Advisor: Prof. Pierluigi Di Lizia
Co-advisors: Dr. Niccolò Faraco
Academic Year: 2021-22

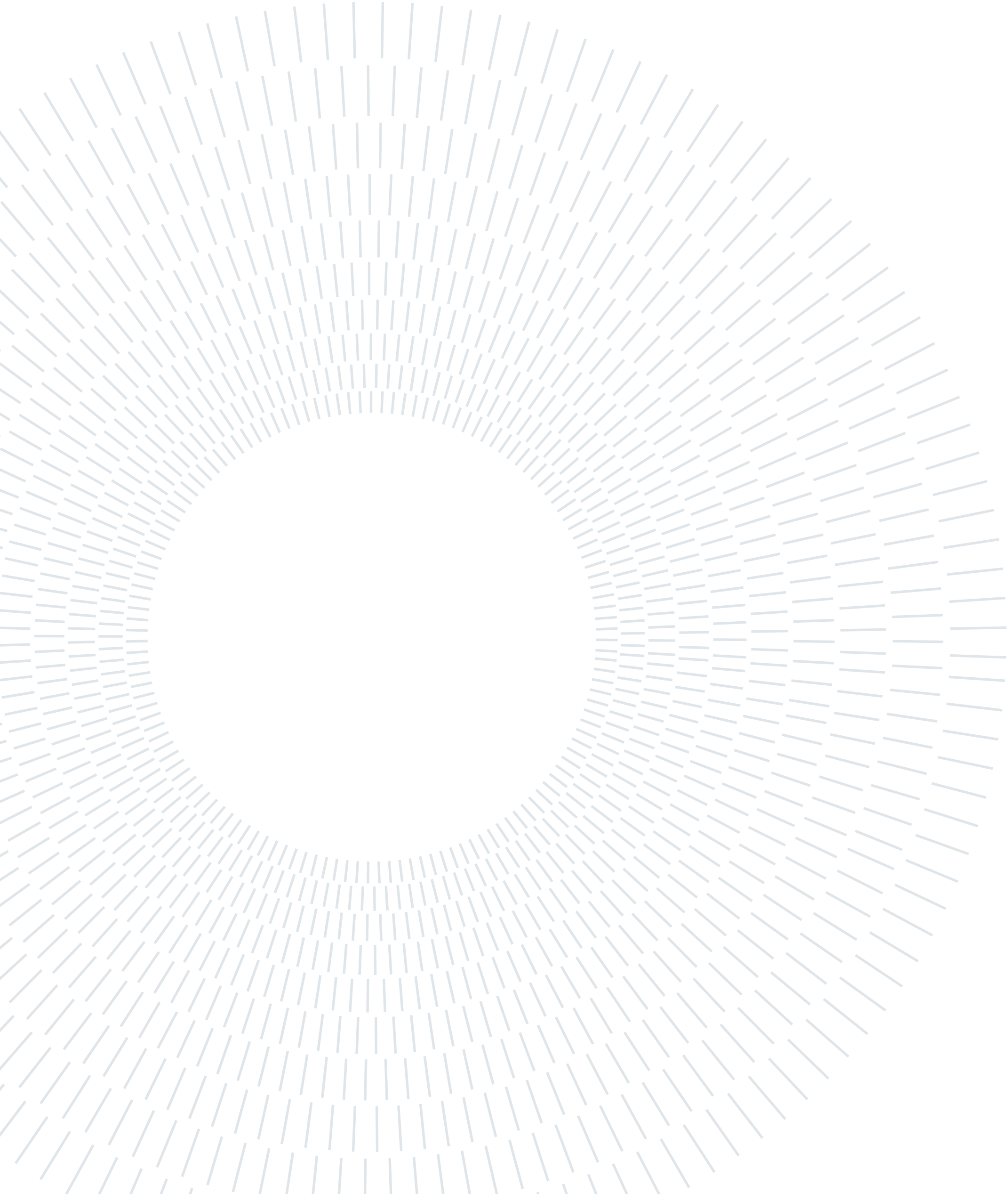

Abstract

After over 60 years from the beginning of the space era, the number of missions has increased exponentially due to the contribution of more and more countries and private companies. At the same time, the problem of space traffic has arisen, mainly on low orbits, and with it the generation of the so-called *space debris*, coming from ceased satellites, waste materials and fragments generated by collisions on orbit. It is important to remark that a debris is not only a small fragment, but it could be an object of big dimensions such as an upper stage of a launcher or even a whole satellite. This thesis aims to implement a tool that, exploiting a probabilistic analysis of the reentry into the atmosphere of a big debris, is able to assess its survivability, to determine the footprint of impacting fragments and to estimate the consequent risk level. In particular, an upper stage has been analyzed because it is the object that has the highest frequency of reentries over the years. Such a probabilistic tool allows to demonstrate and investigate the very uncertain nature of the reentry problem. In fact, the developed algorithm includes the treatment of those uncertainties that come from the lack of knowledge of precise values of parameters or from highly variable phenomena. One of the most interesting contribution of the thesis is the combination of breakup model and location of impact points. In such a way, it is possible to quantify the casualty expectancy associated to a certain geographical area on the Earth. Moreover, the breakup model exploits a structural element that drives the separation of all the other components, representing what actually happens after the main breakup event. The proposed method has a wide range of applicability, since it is able to evaluate different reentry scenarios with varying initial conditions, categories of the object and types of orbit. The ultimate goal would be a campaign of simulations that accounts for all the possible reentry cases of a certain category of space vehicle, in order to fill in a database with the probability distributions of the main results.

Keywords: upper stage reentry, probabilistic breakup model, casualty risk, fragmentation, sensitivity analysis

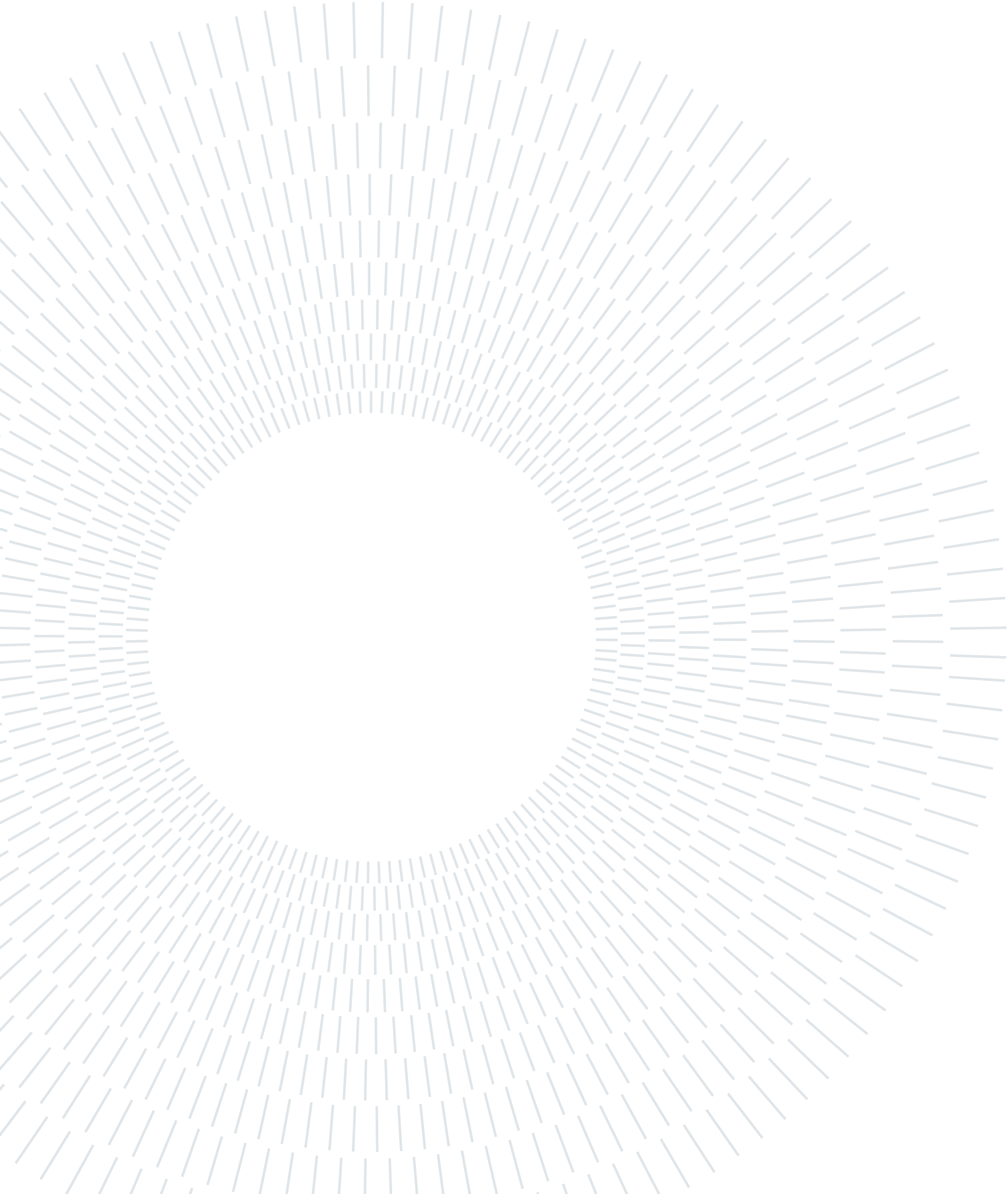

Sommario

Dopo oltre 60 anni dall'inizio dell'era spaziale, il numero di missioni è aumentato esponenzialmente attraverso il contributo di numerose nazioni e compagnie private. Allo stesso modo ha preso forma il problema del traffico spaziale, soprattutto in orbite basse, e con esso la formazione dei *detriti spaziali*, dovuti a satelliti non più operativi, materiale di scarto e frammenti generati da collisioni. E' importante tenere presente che un detrito non è solo un piccolo frammento, ma può essere anche un oggetto di dimensioni notevoli come lo stadio superiore di un lanciatore o un intero satellite. Questa tesi ha come obiettivo la realizzazione di uno strumento che, tramite un'analisi di tipo probabilistico del rientro in atmosfera di un grande detrito, sia in grado di valutare la sua sopravvivenza, determinare la zona di impatto al suolo dei frammenti e quantificare il rischio che ne consegue. In particolare viene analizzato lo stadio di un lanciatore poichè è il tipo di oggetto spaziale che più frequentemente rientra in atmosfera. Tale strumento probabilistico consente di dimostrare e investigare la natura incerta del processo di rientro, infatti l'algoritmo è stato costruito in modo da includere la trattazione delle incertezze legate a quei parametri i cui valori sono poco conosciuti oppure soggetti a forti cambiamenti. L'accoppiamento del modello di distruzione con le coordinate dei punti di impatto è uno dei più interessanti contributi della tesi, poichè permette di stimare il numero di possibili vittime in una certa area geografica. Inoltre, il modello di distruzione si avvale di un elemento strutturale per determinare la rottura primaria, cioè il momento in cui il veicolo si separa in diverse parti. Il metodo proposto ha un vasto campo di applicabilità e può essere quindi usato per valutare casistiche di rientro differenti per condizioni iniziali, categorie di oggetto e forme di orbita. Il fine ultimo sarebbe quello di utilizzare l'algoritmo per simulare tutte le possibili eventualità che potrebbero accadere durante il rientro di una certa categoria di oggetto, in modo da compilare un database con le distribuzioni di probabilità dei risultati post-rientro.

Parole chiave: rientro stadio di lanciatore, modello di distruzione probabilistico, valutazione del rischio, frammentazione, analisi di sensitività

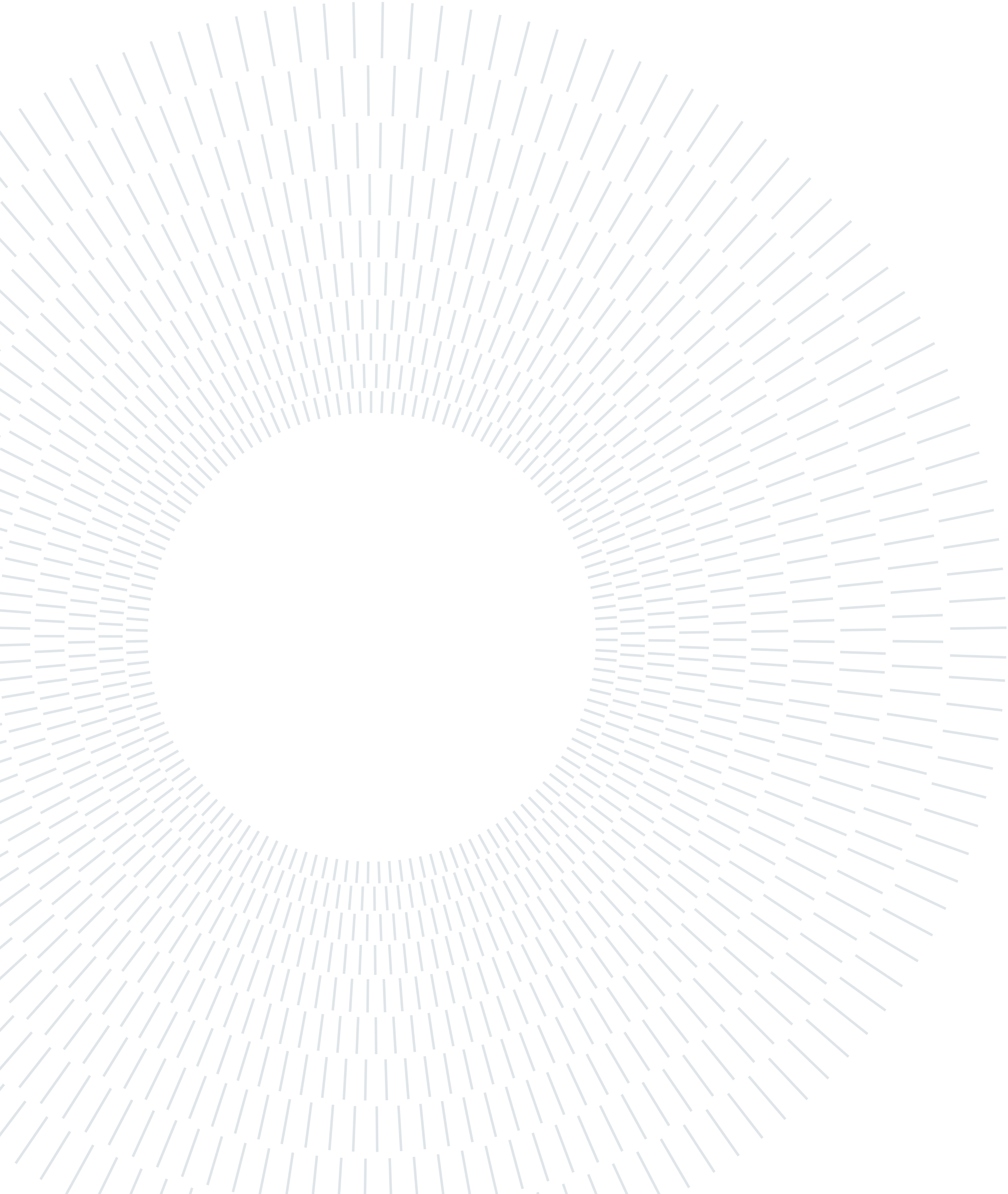

Ringraziamenti

Ringrazio, prima di tutti, il professor Di Lizia per la disponibilità e professionalità con cui mi ha guidato e supportato nel lavoro di tesi. Grazie alla sua impostazione e organizzazione, ho potuto affrontare e sviluppare l'argomento proposto al meglio delle mie possibilità e con serenità e fermezza. Inoltre mi ricorderò sempre del sincero riconoscimento ricevuto al termine della tesi ed, in particolar modo, della sua frase: "se fossi un datore di lavoro, ti assumerei per quanto hai realizzato".
Ringrazio anche il dottor Faraco per il supporto, i consigli e le risposte sempre puntuali e complete.

Un grande e doveroso ringraziamento va ai miei genitori, Massimo e Giovanna, che non mi hanno fatto mai mancare nulla e hanno sempre agito nel migliore dei modi per il mio bene e per la mia crescita. Senza il loro supporto e la loro comprensione non avrei mai potuto essere quello che sono oggi e non avrei mai potuto avere quello che ho oggi. Vi ringrazio per avermi insegnato il rispetto, la serietà e l'educazione e per essere stati delle figure fondamentali nei momenti più difficili e deludenti del passato. Mi avete dimostrato che i veri genitori sono sempre presenti incondizionatamente.

Ringrazio Luisa, l'amore della mia vita, per avermi supportato, sopportato, incitato e aver creduto in me ogni giorno da quando ci conosciamo. Grazie per essermi stata vicino e aspettato in questi anni, che con te a fianco si sono rivelati meno amari di quanto fossero. Questa laurea è un traguardo molto importante che ho raggiunto anche grazie a te e finalmente chiude un oltremodo lungo capitolo personale, ma allo stesso tempo apre la strada a molteplici prospettive e possibilità per la nostra vita.

Un pensiero particolare va anche a tutti i miei nonni, in vita e non, per tutto il tempo e l'affetto che mi hanno dedicato. Grazie a loro ho capito quanto sia importante tramandare alle generazioni future le proprie conoscenze ed i propri ricordi.

Ringrazio i miei parenti per l'affetto e la discrezione con cui mi sono stati vicino in questi anni. In particolare, grazie per la considerazione che avete di me.

Ringrazio anche la famiglia di Luisa, che ormai da diversi anni mi ha accolto e mi è sempre stata vicina e solidale. Grazie per le giornate spensierate trascorse insieme.

Un ringraziamento va anche ai tanti compagni di corso, con cui ho trascorso momenti piacevoli e condiviso le difficoltà e le preoccupazioni del percorso universitario. Grazie a loro ho arricchito il mio spirito di condivisione ed ho imparato a giudicare le persone per quello che valgono e non per quello che mostrano.

Infine, un grazie anche a tutte quelle persone, opportune e inopportune, che mi hanno fatto capire che, anzichè pensare a cosa dicono gli altri, bisogna concentrarsi su se stessi per riconoscere i propri difetti, identificare i propri limiti e perseverare per superarli.

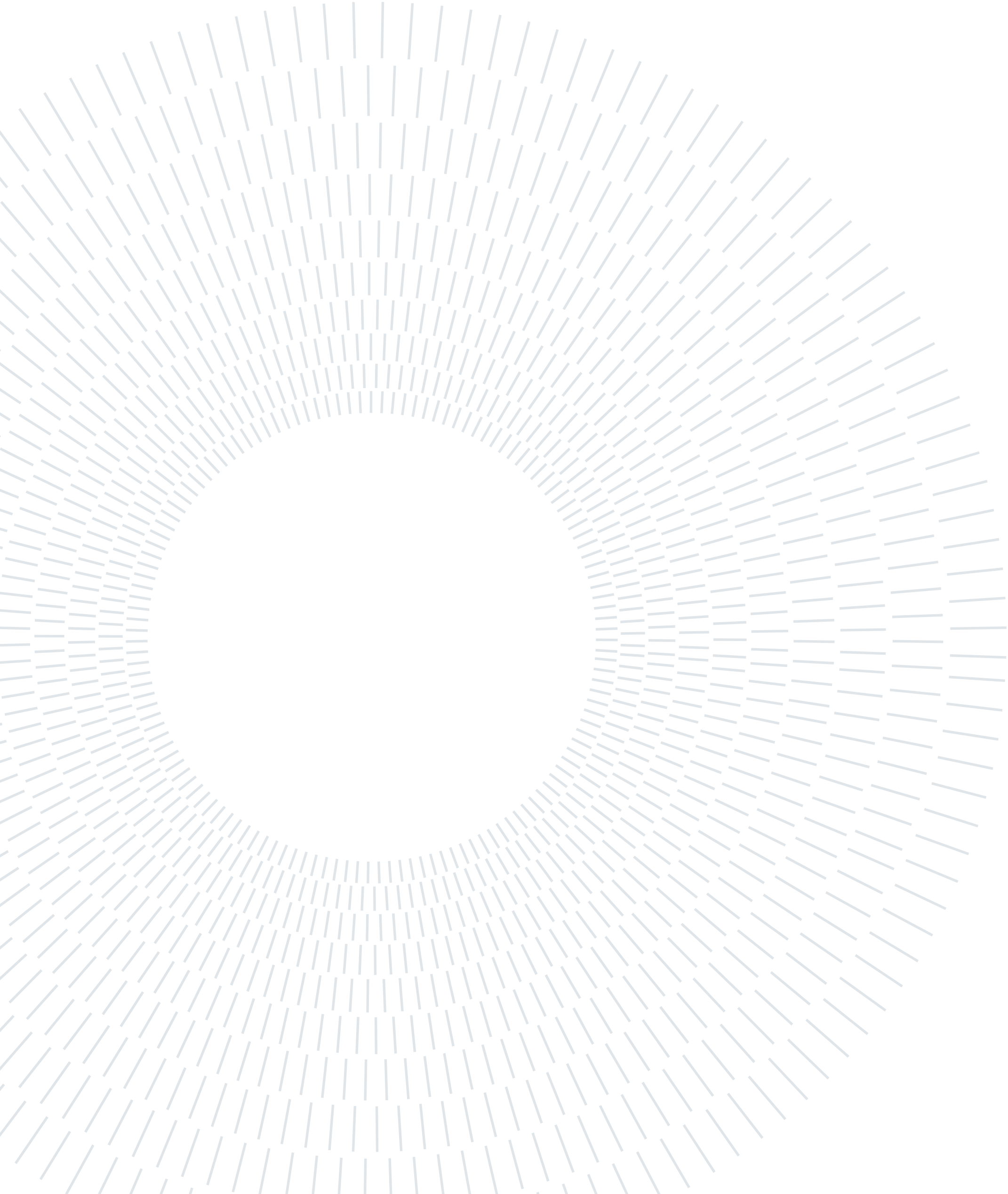

Contents

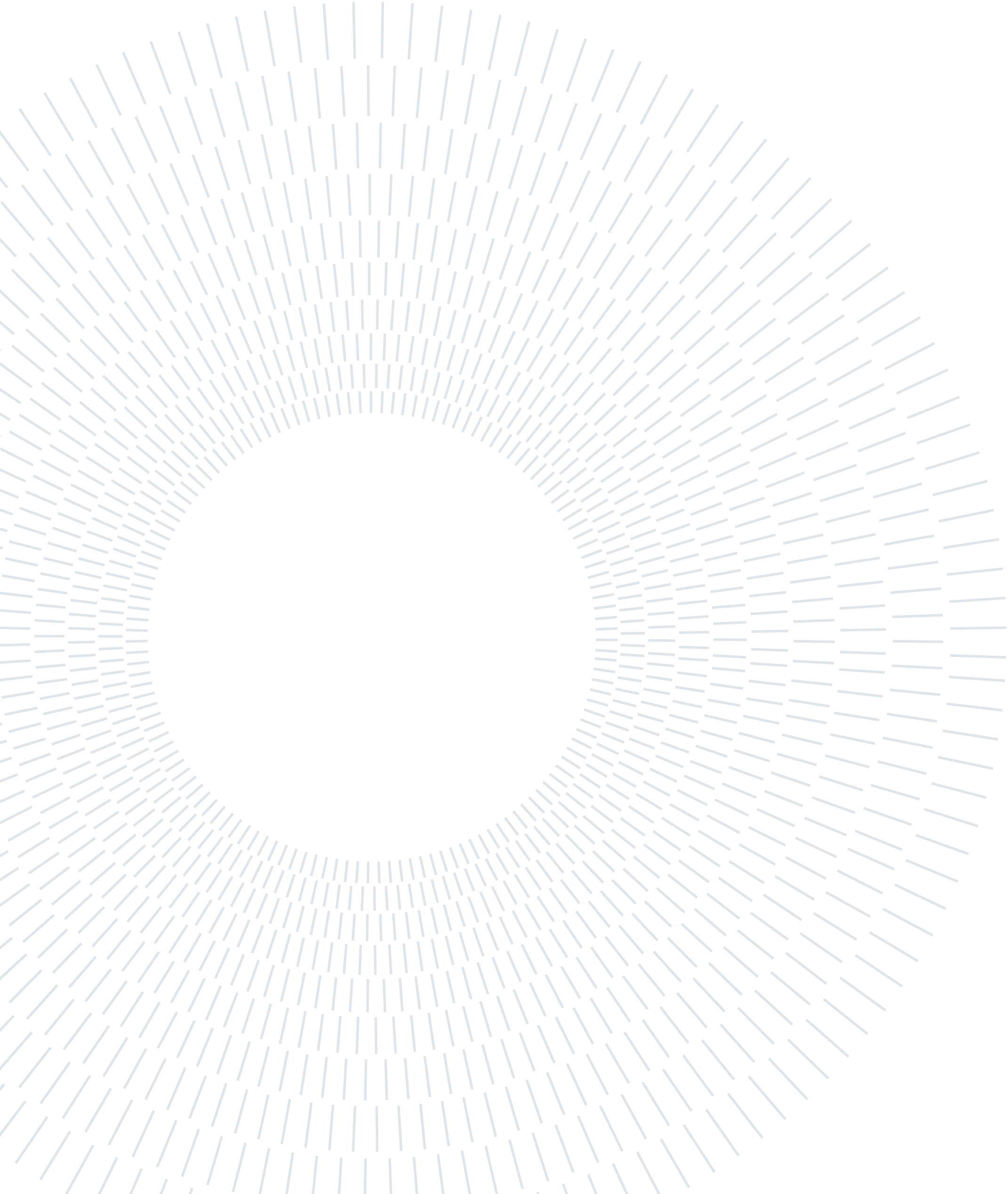

1 | Introduction

1.1. Context

After more than 50 years of space activities, the number of satellites has grown significantly and so did the number of them which ceased their operations and are now orbiting around the Earth without the possibility to be controlled from ground stations. Satellites that are no longer operational, together with upper stage rocket bodies and fragments generated by collisions with meteoroids or other artificial satellites, constitute the so-called *space debris population*. Space debris could stay on orbit for many years, representing an hazard for active satellites and encumbering on the design of new launches. Moreover, when the orbit of one debris decays, mainly due to atmospheric friction, the object can pass through the atmosphere and pose risk to public safety, striking people and properties on ground.

From the decay of the Sputnik 1 launch vehicle core stage on 1 December 1957, more than 25,000 catalogued orbiting objects have reentered the Earth's atmosphere. It is possible to identify two types of reentry. Random reentry is the term used for orbiting objects that do not have the ability to deorbit on a controlled trajectory that avoids populated areas. Controlled reentry is the term used when there is an attempt to drive the reentry such that the bulk of the spacecraft will land in water or known unpopulated land areas. Currently, approximately 70% of the reentries of intact orbital objects are uncontrolled, corresponding to about 100 metric tons per year, and on average there is one spacecraft or rocket body uncontrolled reentry per week, with an average mass around 2000 kg [1].

For these reasons, the main institutions in the industry have defined standards for the calculation of the overall risk of a space mission and maximum admissible values for such a risk. In terms of mass, number and components survivability, the uncontrolled reentries of spent upper stages generally present a higher risk compared to payloads and, except for very specific accidental cases, the bulk of the recovered reentry fragments comes from rocket bodies. This was one of the reasons, together with orbital debris mitigation, leading to the increasing practice of upper stage controlled deorbiting during the last few years. According to their importance in the reentry topic, upper stages are selected as the exemplary vehicles for the reentry analysis performed in this thesis.

The present work is focused on the probabilistic analysis of the uncontrolled atmospheric reentry of an upper stage vehicle, with the aim of estimating the associated risk and impact on ground. The developed algorithm exploits the paradigm proposed by Frank, Weaver and Baker [2], trying to refine the way in which breakup altitude of the main vehicle, fragmentation of released components and location of impact points are treated.

1.2. Motivation of the work

In the past few years there has been a steady rise in the number of space launches as well as the privatization of launch capabilities. With the increasing number of space missions, it comes out also an increased interest in safety analysis to address possible risk to the population. The design-for-demise strategy has been implemented to conceive space objects for safe reentry when a controlled reentry is not feasible.

The standards assume that casualty area of a randomly reentering spacecraft can be calculated relatively precisely and show that for random reentries the casualty expectation per unit casualty area depends only on the orbital inclination angle. This is due to the fact that available calculation paradigms are mainly deterministic. Deterministic tools are based on complex mathematical and computational models and rely on accurate vehicle debris fragment models to estimate the probability of a human casualty. However, the reentry problem has an almost unknown nature and it is characterized by an intrinsic stochastic variability. Therefore, a probabilistic method may be more promising to investigate the effects of epistemic uncertainties on results.

The main objective of this thesis is to provide a tool that is able to determine the probability distributions of casualty area and casualty expectancy associated to a reentry event, replacing common assumptions with uncertainty distributions on main reentry parameters. The inclusion of uncertainties treatment enables the investigation of different reentry scenarios and extends the range of applicability of the reentry algorithm to various categories or assemblies of space objects and to various types of orbit. The ultimate goal of such a method is to provide a probability function that directly relates the state of a vehicle at the epoch of reentry to the impact location and casualty expectancy. This would be used to understand the most probable and hazardous impact regions, so that further detailed analyses can be performed to refine the risk estimation.

1.3. Contribution of the thesis

The computational algorithm detailed in this thesis combines several well established models for earth geometry, gravitational acceleration, atmospheric properties, trajectory propagation and aero-thermal demise tailored for reentry debris. Through the introduction of a fictitious element that represent the structure of the vehicle, the breakup altitude is better estimated as the altitude at which all the element are released, as actually happens in the main breakup event.

The fragmentation model has been revised in order to better define the properties of generated fragments. Not only the number of fragments is obtained from the percentage of mass ablation, but also geometric and aerodynamic properties are set through the definition of categories according to the initial mass of the fragment itself.

The overall method is based on simple equations and assumptions, but it accounts for uncertainties. Thus, it is appropriate for investigation of the effects of such uncertainties on the quality of results. An extensive sensitivity analysis has been carried out to demonstrate the variation in results associated with the uncertainties.

Finally, in order to improve the estimation of casualty expectancy, a better prediction of the impact probability of each fragment is made thanks to the computed distributions of casualty area, fragmentation altitude and breakup altitude. In fact, such quantities combined together allow to connect the impact event to the probability of existence of the corresponding fragment.

1.4. Structure of the thesis

Chapter 2 presents an overview of the literature available on the topic of uncontrolled reentry of space debris. The modeling challenges, the existing tools and the importance of considering uncertainties when dealing with reentry analysis are described. Then the most promising methods for estimate the debris dispersion are reported, with highlights on results obtained and limitations. As a reference, standards and definitions related to the risk associated to the reentry event are also reported.

Chapter 3 introduces the model used for the probabilistic analysis of this thesis. After a general description of the structure of the model, every module and its assumptions are described in detail. The last section explains the way in which uncertainties are treated.

Chapter 4 describes in detail the architecture of the algorithm. After an overview of the main structure, the initial conditions and parameters needed for the execution are presented. Then, the working principle of each specific module is explained and input and output variables are listed.

In Chapter 5, results of performed simulations are shown. In particular, probabilistic outcomes of the base case simulation on the Delta II 2nd stage are represented through histograms and footprint dispersion images. In addition, variability of the nominal impact point is investigated and casualty risk analysis is applied to the most hazardous locations. Finally, a sensitivity analysis is performed on all the parameters in order to find out which ones cause the greatest changes in results. Consequently, only the effects of the most relevant parameters are described.

Finally, in Chapter 6, conclusions on the work are drawn and considerations are made on improvement of critical aspects and on future research topics.

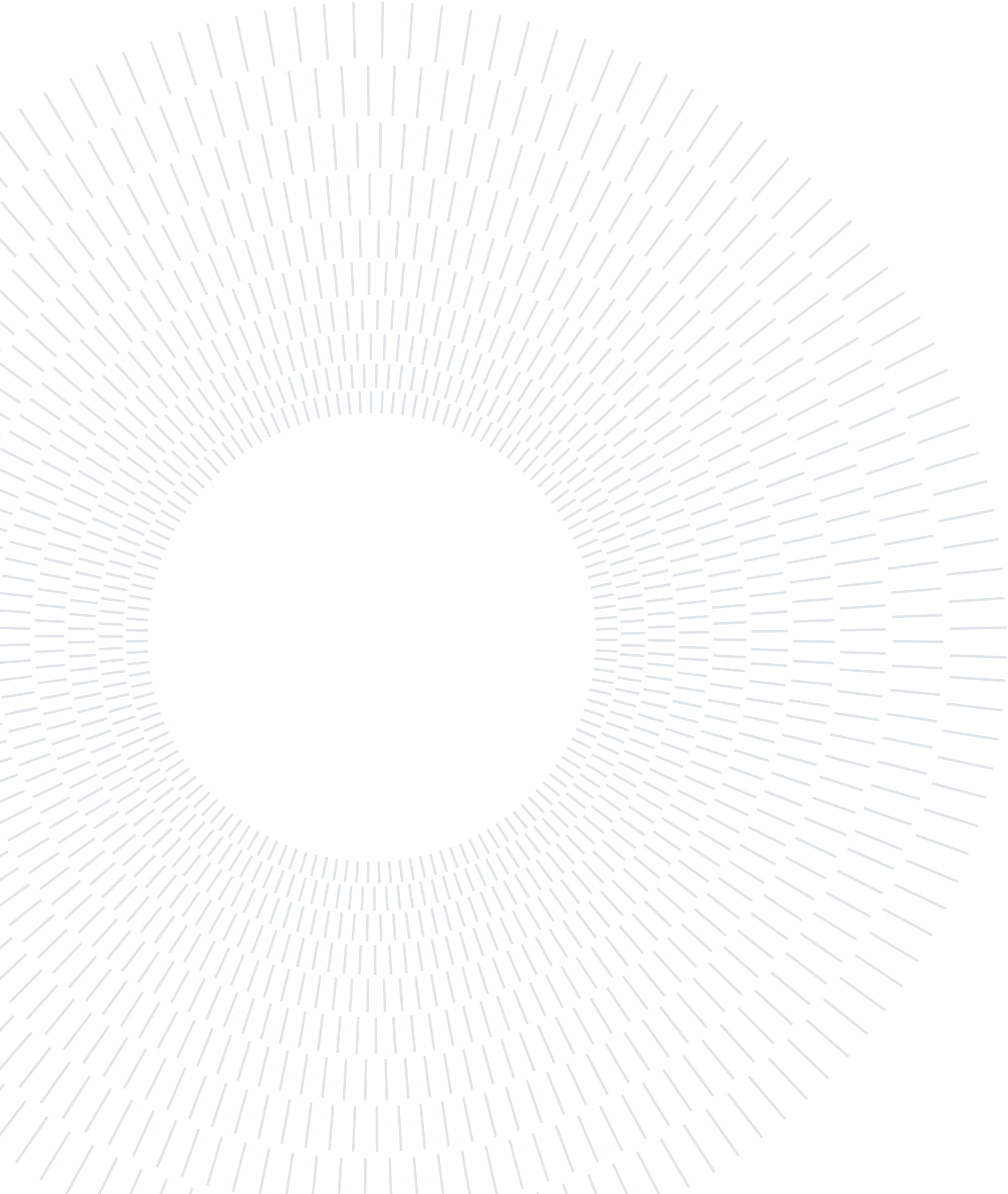

2 | Space debris and footprint characterization

Decaying satellites, upper stage rocket bodies and fragments generated by collisions with meteoroids or other artificial satellites constitute the so-called *space debris population*. Most of the debris usually suffer complete demise during reentry, but surviving ones can cause serious damage on ground to people, buildings and natural ecosystems. The ground footprint of the surviving debris is difficult to predict and can be tens of kilometers wide and hundreds of kilometers long.

In this chapter an overview of the literature available on the topic of uncontrolled reentry of space debris is presented. The first section illustrates the modeling challenges, the existing tools and the importance of considering uncertainties when dealing with reentry analysis. Then the most promising methods to estimate the debris dispersion are described, with highlights on results obtained and limitations. Finally standards and definitions related to the risk associated to the reentry event are reported.

2.1. Uncontrolled reentry of a space debris

Uncontrolled reentry is the term used for orbiting objects that do not have the ability to deorbit on a controlled trajectory and, hence, pose risk to public safety, striking people and properties on the ground as well as aircraft in the air.

Nowadays, nearly 70% of the reentries of intact objects are uncontrolled. About one hundred large space systems, either satellites or rocket upper stages, reenter the Earth's atmosphere annually [1]. With the increasing of the space activity, the number of objects in orbit is destined to grow rapidly and, with it, the frequency of reentries. Reentry tools have been developed all over the world in order to simulate the destruction processes and to assess the resulting ground risk.

2.1.1. Modeling challenges

Over time, the orbits of space objects in low Earth orbit decay and tend to circularize due to the higher drag experienced close to the perigee region, since part of the orbital energy is lost because of the interaction with the atmosphere. A fraction of the energy goes into heating the space object itself, according to the aerodynamic shape and motion during reentry. If the heating rate is sufficiently high, the space object skin or outer components can melt or vaporize. The heating rate depends mostly on the speed at which the object descends through the atmosphere, which can reach more than 7 km/s and depends on the ballistic coefficient. Vehicle survivability prediction is complicated by vehicle breakup, which exposes shielded components to direct atmospheric heating. Thus, internal components of various ballistic coefficients are released after breakup and follow separate trajectories and heating profiles. Secondary breakups of released components are possible, and a cascade of secondary breakups can occur.

In order to treat the reentry process the following subjects have to be discussed:

- flight dynamics of the vehicle,
- analysis of the aerodynamic and aerothermal loads,
- analysis of local heating and the resulting melting process,
- analysis of the fragmentation/deformation processes,
- fragment tracking till ground impact.

The flight dynamics concerns the computation of the orbital path till the reentry epoch and then the ballistic trajectory through the atmosphere. Due to the various sources of orbital perturbation, a precise propagation of the orbital path is not possible and the reentry trajectory is translated into predictions of the reentry epoch. Reentry predictions are affected by various sources of inevitable uncertainty due to sometimes sparse and inaccurate tracking data, complicate shape and unknown attitude evolution of the reentering object, biases and stochastic inaccuracies affecting the computation of the atmospheric density at the altitudes of interest, magnitude, variability and prediction errors of solar and geomagnetic activity, and mismodeling of gas-surface interactions and drag coefficient. This means that even predictions issued 3 hours before reentry may be affected by an along-track uncertainty of 40,000 km (corresponding to one orbital path in HEO), possibly halved during the last hour. The time and location of impact points could not be accurately predicted due to unpredictable variations in high-altitude atmospheric density that alter the drag and orbital decay rate. Much of this variation is caused by unpredictable solar activity. Moreover, the trajectory in the denser layers of the atmosphere is mainly affected by the aerodynamic drag, winds contribution and attitude changes of the main vehicle and also of its fragments. An accurate knowledge of ballistic coefficient, atmospheric density and winds profile can improve the trajectory determination.

The analysis of the aerodynamic and aerothermal loads is directly related to the shape of the object and the knowledge of the properties of the flow. Current aerodynamic and aerothermal models in continuum flow regime are suitable for hypersonic flow past clean blunt object, where only a detached shock wave exists away from the object. However, for complex spacecraft or multi-object systems, the shock wave interaction phenomenon may appear, which could induce high pressure and heating regions; the breakup and ablation processes may be significantly altered as a consequence. For sure, a trade off between approximations in the modeling of the object shall be performed. A distinction is made between three flow regimes: free molecular flow, rarefied transitional flow and hypersonic continuum flow. Each regime corresponds to a different way to determine the drag coefficient of the object.

The analysis of the thermal behaviour of the space object is needed to understand the amount of heat absorbed and to predict the breakup altitude, if a temperature based criterion is followed. Heating environment models used for reentry survival analyses rely on well-established theory backed by experimental data, mostly from ground testing. The computation of the thermal balance is affected by the knowledge of flow regime, material properties, object shape and attitude. Despite correlations for convective heat estimation are available for simple shape and under well defined boundary conditions, it's difficult to compute heat flux for every phase of the reentry even if the shape of the objects is coarsely approximated and the attitude is kept fixed. In addition, since the temperature profile over the object surface is not uniform, a detailed thermal analysis is required and this can be done only by advanced tools, such as CFDs.

The occurrence of primary and secondary breakups during reentry makes possible the deformation or fragmentation of the elements of the space vehicle. Deformation can significantly change the aerodynamic properties of a falling element with direct influence on the evolution of the reentry trajectory and increased uncertainty in the impact point on the ground. In addition, the formation of a fracture or a hole can augment the area exposed to the heating flux, increasing the ablation rate, and at the same time reducing the mechanical resistance of the element itself, therefore increasing the probability of further deformations. Fragmentation can happen in many phases of the reentry: for example when an element detaches from the main structure, when the level of induced mechanical stress overcomes the material resistance, which also depends on the temperature reached by the element, or when the amount of mass ablation is so high that the element could no longer be intact. Even if the event is assumed somewhere during the reentry, it is extremely difficult to define the characteristics of each fragment of uncontrolled debris after the breakup. For these reasons, both phenomena are difficult to predict if dedicated breakup model or failure modes are not implemented. Moreover, the distribution of fragments after the breakup and their evolution till ground impact require the redefinition of the initial conditions and the recalculation of the whole process.

Relying on previous considerations, a complete analysis requires a multi-disciplinary system in which various modules continuously exchange the individual results for a stepwise analysis of the spacecraft reentry and the resulting destructive process. Finally, the great variability of the reentry problem requires an accurate modeling effort and a complete investigation of the uncertain variables and parameters, always taking into account that very little is precisely predictable and the overall topic is mainly epistemic.

2.1.2. Uncertainties affecting the reentry

Uncertainties are caused by inexact modeling capability, parameter variability, and uncertainties in parameters state-of-knowledge.

The accuracy of reentry predictions is influenced by many factors, such as the initial conditions (in the form of reentry velocity, altitude, flight path angle, etc.), the ballistic coefficient of the object, the modelling of the atmosphere, the aerothermal heating experienced by the object, the modeling of the spacecraft and its elements and approximations needed to make the problem tractable and computationally sustainable.

The breakup instant and trajectory evolution are stochastic and depend on the object's physical characteristics, orbital elements and environment including the perturbing gravitational influences, exosphere state, and space weather characteristics. During the final stages of a debris object's orbital life, the perturbations from atmospheric drag may equal or exceed any gravitational perturbations. Uncertainty in the dominant perturbing force induces significant uncertainties in any reentry path prediction. In addition, breakup and demise are affected by attitude and orientation of the spacecraft, number, mass, shape and heating area of fragments, shielding by other parts and tumbling modes. Physical and thermochemical properties include material properties, structural strength and its variation with temperature, chemical effects such as eutectic formation, dissolution, surface oxide layer effects, heat of fusion and ablation energy.

2.1.3. Deterministic tools

Many reentry analysis tools have been developed all over the world in order to calculate the destructive process and to assess the resulting ground risk, such as Debris Assessment Software (DAS)[1], Object Reentry Survival Analysis Tool (ORSAT)[2], Debris Risk Assessment and Mitigation Analysis (DRAMA)[3] and SpaceCraft Atmosphere Reentry and Aerothermal Breakup (SCARAB)[4]. Note that these tools are based on a deterministic approach and their capability to handle the uncertainty associated with the reentry quantitatively is limited, which is one of their important disadvantages.

Lips, et al. [5] classified the analysis methods into two categories: the object-oriented method and the spacecraft-oriented method. *Object-oriented* tools can be operated quite easily and do not need much computing capacity. However, these tools have to rely on a user-defined fragment list describing all potentially surviving fragments as simple-shaped geometric objects (e.g. spheres, boxes, cylinders, flat plates). The breakup process itself is not analyzed or predicted by these tools, but it is subjected to the assumptions and experience of the tool operator. *Spacecraft-oriented* tools try to predict the fragmentation process, providing more information about breakup altitudes, number of fragments, and fragment shapes. This requires a more detailed description of the reentering spacecraft and more sophisticated analysis algorithms. The time and costs for spacecraft-oriented analyses can be about one order of magnitude higher than for object oriented reentry analyses. The much higher computing time for such an analysis prevents the application of this approach in real Monte Carlo type safety assessments.

Therefore, object-oriented tools are usually adopted in the first project phases when multiple trade-offs have to be considered. They provide valuable inputs for the definition of the mission and system architecture with initial identification of elements that are likely to survive the reentry and that could pose risk for population and properties. With this information, the system engineers can steer the spacecraft design towards safer solutions, implementing mitigation measures early in the project development, and save costs. In more advanced project phases, as the system definition gets into more details, spacecraft oriented tools are usually adopted to verify that the mission and system design solution is compatible with the casualty risk requirements.

The deterministic approach may be questionable because it is not thought to account for uncertainty sources which may affect the analytical results significantly.

---

[1] DAS `https://orbitaldebris.jsc.nasa.gov/mitigation/debris-assessment-software.html`

[2] ORSAT `https://orbitaldebris.jsc.nasa.gov/reentry/orsat.html`

2.1.4. Probabilistic tools

As stated above, the problem of uncertainties treatment is crucial in spacecraft and debris reentry analysis, thus a probabilistic approach is more appropriate than a deterministic one. In fact, it is important to have an accurate estimate of not just the deterministic impact location but also the statistical distribution due to the uncertainties involved. In essence, probabilistic tools attempt to replace assumptions used by deterministic tools to compensate uncertainties related to models and parameters with probability distributions that represent the range of knowledge and the inherent stochastic variability of the phenomena.

Few probabilistic tools are available in literature and the most valued one is the work by Frank, Weaver and Baker [2], in which a probabilistic paradigm is exploited to calculate the uncertainty in casualty area of randomly reentering debris from orbital objects. The underlying principle is that a method based on simple equations, which also accounts for uncertainties, allows for an investigation of the effects of such uncertainties on the quality of results, and demonstrates the variation in results associated with the uncertainties. The resulting insights might then highlight the areas of research that will ultimately improve the accuracy of the prediction.

2.2. Estimation of debris dispersion

The final purpose of the reentry analysis is to determine the consequences that falling debris have on ground and also on air traffic. A lot of methods able to compute the debris dispersion are available in literature. In the following the most promising ones are introduced.

2.2.1. Monte Carlo analysis

A Monte Carlo (MC) campaign is the most intuitive approach available for uncertainty quantification and propagation. With this approach, a large number of simulations over randomly sampled states allow the estimation of the joint Probability Density Function (PDF) through a frequentist approach. As the quality of the results of MC simulations is strongly affected by the number of samples, a reliable uncertainty analysis can only be obtained through computationally expensive simulations, especially for multi-dimensional and non-linear dynamics such as the ones associated with reentry scenarios.

2.2.2. Covariance propagation

Reyhanoglu and Alvarado [6] introduced a covariance propagation method for estimating the debris dispersion from the breakup of a space object, assuming little or insufficient knowledge of key parameters. Their approach predicted a dispersion area similar to that obtained by a Monte Carlo simulation but required shorter computational time, indicating greater efficiency. The falling debris is simulated and resulting data are analyzed to derive the probability of debris evolution at different altitude layers over time. The concept of positional probability ellipsoids has been employed for the visualization of the results. After deriving the 3D translational equations of motion relative to a spherical rotating planet, a nominal trajectory is obtained by using the state vector right before the breakup as the initial state and the average ballistic coefficient. The equations of motion are linearized around the nominal trajectory and the problem is formulated as a continuous Gauss–Markov process. Finally, a covariance propagation approach is introduced to estimate the positional probability ellipsoids. Dispersion around the nominal trajectory can then be quantified through the ellipsoids representing the level curves of the Gaussian probability density function. There are some limitations in this approach: the breakup instant is assumed, the ballistic coefficient is kept fixed and only one debris at a time is propagated.

2.2.3. Chance-constrained optimization problem

Falsone and Noce [7] formulated a chance-constrained optimization problem to determine the 4-dimensional debris footprint; they used a stochastic debris dynamics and obtained the footprint through a simulation-based approach. The goal is to determine the minimum size 4D region of the airspace where all trajectories except a set of predefined probability are confined. This has been formulated as a chance-constrained optimization problem and solved through a randomized method. The resulting approach to determine the 4D footprint rests on running multiple realizations of the reentry trajectory and imposing that they belong to the footprint. For this reason, it is called simulation-based method. The resulting randomized algorithm for footprint calculation is shown to outperform the covariance propagation approach and to be of more general applicability. The main limitation of this method is that the breakup instant is assumed a priori.

2.2.4. Correction of the down-range and cross-range positions of the nominal impact points

The paper by Kim, et al. [8] proposes a two-phase framework to predict the impact dispersion area of a reentering space object. A semi-analytic approach that predicts the dispersion area by combining an analytic impact point sensitivity model with corrections to account for aerodynamic drag has been developed. The dispersion area is then described using a formulation composed of the center point prediction and the downrange/crossrange corrections. The first phase of the framework (preparation phase) generates a database storing the coefficients used in the correction model; this applies the least-squares method to the results of numerical experiments on the space object reentry for various initial states (position and velocity) and aerodynamic characteristics (i.e., ballistic coefficient). The second phase (execution phase: during the reentry event) predicts the dispersion area of the falling object using the correction coefficients database generated in the preparation phase. The comparative study demonstrates that the proposed framework can predict the footprint of the reentering space object effectively with small computational resource consumption. In addition, it can be used for runtime reentry monitoring, because it adopts a simple but effective dispersion model based on the impact point's sensitivity, calling on a massive parameter database that was populated beforehand. For the simulation, it is assumed that the breakup of the space object takes place at a certain altitude, where the fragmented elements start falling with variations in position, velocity, and ballistic coefficient. Moreover, it is assumed that the range of ballistic coefficients of the parts after break-up of reentering object is known, and can be used as an input.

2.2.5. Propagation of the joint probability distribution and reconstruction of the uncertainty density

The work presented in the contribution by Trisolini and Colombo [9] has outlined a methodology to propagate and reconstruct reentry uncertainties using the continuity equation and Gaussian Mixture Models. In addition, using the method combined with the NASA Standard Breakup Model (SBM), the introduction of uncertainties due to the breakup of the parent spacecraft on the release of internal components have been taken into account in the reentry process. The SBM is used to model the ejection velocity of internal components at breakup through a log-normal distribution. The continuity equation is coupled with the reentry dynamics to obtain the actual value of the probability density as it evolves over time through the characteristics of the system. Since the value of the density is only known at discrete points in the state space, a reconstruction methodology must be used to obtain the uncertainty distribution in the entire domain. Therefore, a fitting is performed using the Starling suite developed at the Politecnico di Milano, which is based on Gaussian Mixture Models. Finally, the marginal distribution in longitude and latitude can be readily obtained and used for the prediction of the on-ground casualty risk. Limitations consist in neglecting uncertainties in the atmospheric quantities, uncertainty in the break-up altitude and the demise of the components. In addition, the outputs of the NASA SBM have been specifically developed for orbital fragmentation after collisions or explosions and therefore have a limited validity in the reentry environment.

2.3. Risk analysis

For many years, man-made objects reentering the Earth's atmosphere have not been viewed as a hazard because the heat generated during reentry was expected to completely destroy them and the statistical likelihood of a collision was considered small. Over recent years, the rising population of space debris has been increasingly recognized as a serious issue for the space-faring community. Mitigation is required, either by moving satellites to a safe very stable orbit at the end of their active life, or by disposing of them by reentering the Earth's atmosphere. For energetic reasons, the former option is preferred for spacecraft in MEO or GEO, and the latter for LEO objects. However, the side effect of reentry is the risk to human population and properties from surviving objects. Therefore, guidelines and technical standards for limiting and mitigating the amount of debris in orbit and defining the acceptable levels of risk to the population on the ground have been published by all the major space agencies, including NASA and ESA [10].

2.3.1. Safety standards

In accordance with NASA safety standard [11], a threshold of total casualty probability E_C of 1:10000 per reentry event is proposed, below which the reentry hazard could be accepted. If the casualty expectation of a reentering satellite exceeds the limit, a controlled deorbit is strongly recommended. Compliance with this requirement can be achieved by a controlled deorbit, where the safety concern is not the survivability of elements but the size of the footprint in order to fit it into a safe area, usually the open ocean, with sufficient clearance of landmasses and traffic routes. However, the effects in mass and cost of a controlled reentry can be prohibitive, and hence the alternative is to ensure passive and safe reentry within a 25-years time frame. As uncontrolled reentries are fully passive, they do not rely on the operability of the satellite at end of life, and therefore they maximise the operative life by avoiding the need to deorbit a still-functioning satellite. Larger spacecrafts cannot generally reduce the risk adequately for uncontrolled entries, and must therefore be designed to have a controlled landing in the ocean. Smaller satellites can be assumed to demise fully on entry without any changes being needed. In between, there are satellites which may have a casualty risk above 1:10000, but low enough that risk could potentially be reduced below this level by design changes.

The calculation of the on-ground casualty risk covers three aspects. First, the surviving fragments have to be determined and their size, mass and impact velocity characterized. Fragments with impact energy less than 15 J are not expected to cause injury and so are usually ignored. Second, the casualty area, which represents the collision cross-section between a fragment and an unsheltered human body, has to be calculated. Finally, the casualty area must be transformed into casualty risk. Particular attention shall be given to small fragments that are non-hazardous for people on the ground but are potentially hazardous for aircraft due to relative velocity at impact, and because of aircraft structures and systems vulnerability. A fragment of 300 grams is considered catastrophic for an airplane by FAA norms [12].

2.3.2. Casualty definitions

The human casualty risk associated with an uncontrolled reentry can be subdivided in primary and secondary. The primary risk derives from the possibility of a direct hit of people in the open by a falling fragment. The secondary risk is instead associated with a potential debris impact on a building, a shelter, a high risk industrial plant (e.g. chemical or nuclear) or a vehicle (e.g. aircraft, ship, or train), possibly leading to indirect human casualties.

In order to evaluate the hazard and ground risk due to a single surviving debris, the NASA safety standard NSS 1740.14 [11] introduces an equivalent casualty area A_{C_i} of a single debris, which is composed by the final cross-section area A_i of the debris and a projected cross-section area of a standing human A_h of 0.36 m^2. The total casualty area A_C of a reentry event is the summation over all surviving fragments,

$$A_C = \sum_{i=1}^{n} (\sqrt{A_h} + \sqrt{A_i})^2 \tag{2.1}$$

The casualty probability E_C is a statistical measure of people that may be struck by reentry debris. Generally the overall casualty expectancy E_C is estimated using the following relationship (2.2):

$$E_C \approx \frac{N \cdot A_C}{4\pi^2 \cdot \sin\left(L_{max}\right)} \tag{2.2}$$

where L_{max} is the maximum latitude, north or south, overflown by the reentering satellite, $4\pi^2 \sin\left(L_{max}\right)$ is the area of the latitude band overflown by the satellite, N is the total population resident there and A_C is the total effective casualty area for the impacting fragments.

The casualty expectancy for people in the open might be slightly refined taking into account winds, trajectory path angle, sliding, skidding or bouncing at ground impact, and splattering or cratering. In addition, debris carrying explosive, toxic or radioactive substances can significantly increase the casualty area. Concerning sliding, bouncing or splattering at ground impact, the three effects are generally exclusive and, because soft soil tends to be more common than hard surfaces, the effective casualty area computed using Eq. (2.1) might be, at most, enhanced by a factor 2.

The expression of casualty expectance can be modified to include the concept of probability that each possible reentry event could affect a region of the Earth surface limited in longitude and latitude as follows:

$$E_C = \sum_{i=1}^{N_g} A_C \cdot P_i \cdot \frac{N_{p,i}}{S_{p,i}} \tag{2.3}$$

where N_g is the number of grid subdivisions used in discretizing the longitude-latitude area covered by the predicted landing location, $N_{p,i}$ and $S_{p,i}$ are the population count and surface area relative to the i^{th} grid subdivision respectively, P_i is the probability of the object landing in the area identified by the i^{th} grid subdivision and again A_C is the total effective casualty area.

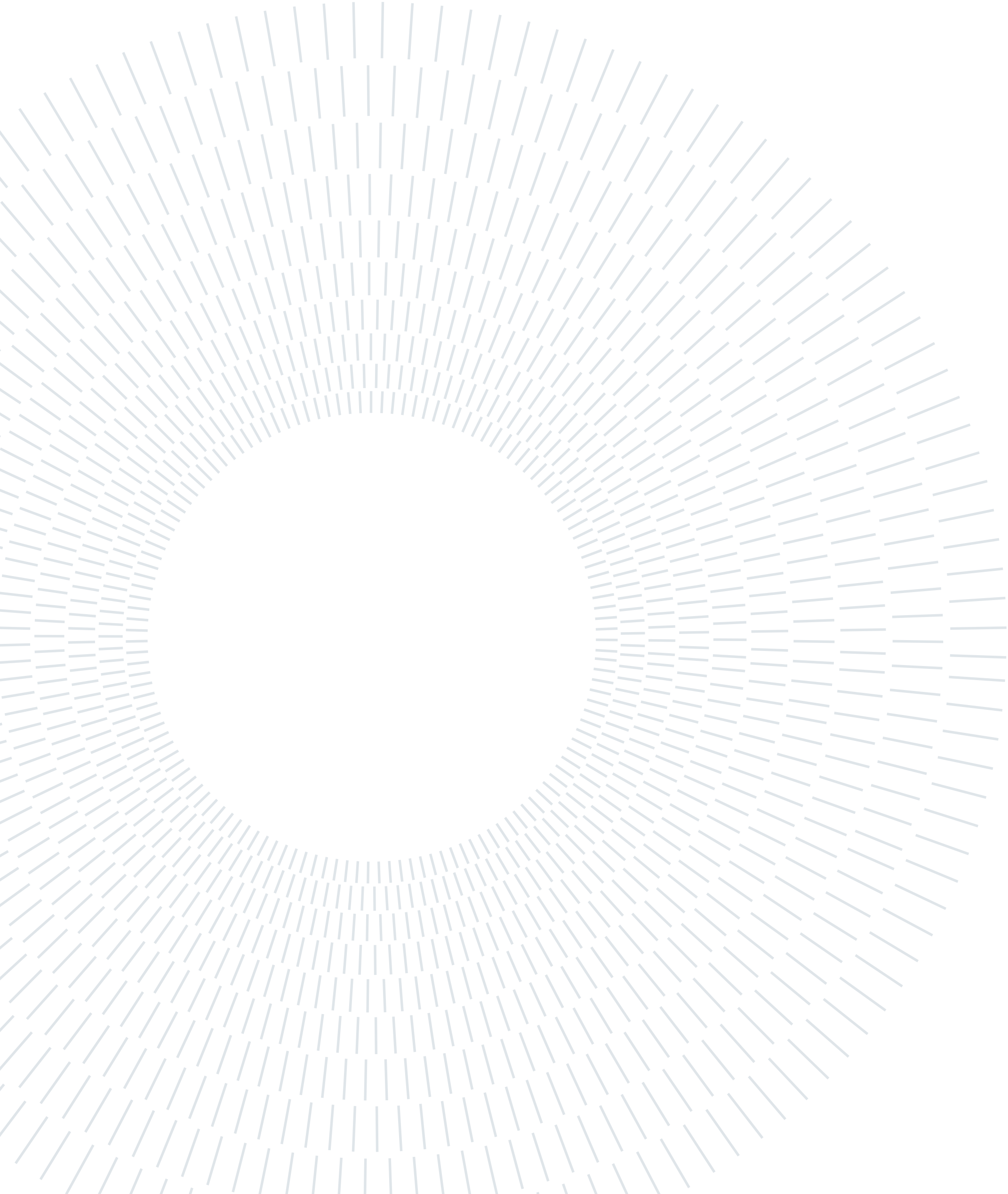

3 | Adopted model

This chapter introduces the model used for the probabilistic analysis of this thesis. After a general description of the structure of the model, every module and its assumptions are described in detail. The last section explains the way in which uncertainties are treated.

3.1. General description

After a deep review of the available literature, the paradigm proposed by Frank, Weaver and Baker [2] is chosen as a guideline for this thesis as it is able to provide the probabilistic distribution of the breakup altitude and in addition it includes the quantification of mass loss due to ablation and the possibility of fragmentation of the elements of the reentering vehicle. The reference work is replicated and analysed in order to have a complete awareness of its capabilities and to understand what aspects could be improved.

Since in the original model, the reentry trajectory is described by the equations of particle motion over a spherical non-rotating planet, a more rigorous trajectory propagator is added, so that the vehicle path can be calculated from the orbital motion till the ground taking into account the effects of non-uniform gravity field, third body attraction, winds and a more sophisticated atmosphere model. In this way, it is possible to combine a probabilistic approach for the prediction of uncontrolled reentry consequences with a refined computation of the nominal trajectory followed during the reentry. In addition, the breakup criterion and generation of fragments are revised.

The adopted model computes the footprint and casualty area of surviving debris starting from the final orbital passages of the vehicle. It is conceptually divided into four modules: the reentry dynamics, the heating process, the ablation process and the fragmentation. Actually modules are interconnected since outputs of one module can be inputs of another one and vice versa according to each phase of the reentry.

The simulation process takes as input the reentry vehicle initial conditions, such as position, velocity, ballistic coefficient, geometric parameters and material properties. Firstly, the nominal trajectory is computed and the heating module is applied to assess at which altitude the vehicle breaks up. Next, the trajectory is recomputed for each element of the original object with initial conditions coincident with position and velocity at the breakup instant and properties of the element itself. Then, heating and ablation modules are applied to determine whether the element demises or not. Demise means that an element completely ablates and it is discarded from the bulk of impacting debris. Fragmentation module considers the possibility that elements can also fragment into smaller pieces that fall independently. Consequently, heating and ablation modules are again applied to each fragment. Finally, the area and landing coordinates of impacting fragments are stored for further risk estimation.

The probabilistic approach consists in including in the simulation the uncertainties related to the most important parameters and replace them with probability distributions. Hence, the model simulates a lot of reentry events, each with different values of parameters sampled at the beginning and kept constant for each trial. In this way, a probabilistic range of output variables is obtained.

3.2. Reentry dynamics

The flight dynamics of the vehicle is computed exploiting the propagator AIDA (Accurate Integrator for Debris Analysis) developed at the Department of Aerospace Sciences and Technologies of the Politecnico di Milano [13]. The tool is able to compute position and velocity of the spacecraft at any time instant from the initial state and epoch till the ground. The numerical integrator used in AIDA is a version of the Dormand and Prince implementation of Runge-Kutta method (8^{th} order solution for propagation, 7^{th} order solution for step size control). The perturbations modeled in AIDA propagator are atmospheric drag, using density model NRLMSISE-00, geopotential acceleration, using EGM2008 model, solar radiation pressure with dual-cone shadow and Sun and Moon gravitational attractions.

NRLMSISE-00 is an empirical, global reference atmospheric model of the Earth from ground to space. It models the temperatures and densities of the atmosphere's components. The model, developed by Mike Picone, Alan Hedin, and Doug Drob, is based on the earlier model MSISE-90, but updated with actual satellite drag data [14]. It also accounts for the contribution to the drag caused by the presence of atomic oxygen and its ions in the ionosphere, the so called anomalous oxygen. Anyway,the atmospheric drag computation takes also into account the rotation of the Earth.

EGM2008 is a spherical harmonic model of the Earth's gravitational potential, developed by the National Geospatial-Intelligence Agency (NGA). This gravitational model is complete to degree and order 2159, and contains additional coefficients up to degree 2190 and order 2159. It provides a maximum accuracy approaching 10 cm. EGM2008 can be truncated to have fewer coefficients with lower resolution. [15]

As compared to the original work, modeling of atmospheric variables and gravitational potential as previously described represents a significant improvement. In fact, in [2], the trajectory module is relatively simple and relies on exponential density model and inverse square gravity law.

3.2.1. Focus on integration time

The drawback of using a more sophisticated model is the increasing of computational time. This is not a problem if a single reentry is simulated but in a probabilistic framework, where the quality of the results is enhanced by increasing the number of trials, it is better to keep the computational burden as low as possible without decreasing the accuracy. Therefore, the following adjustments are made with the aim of reducing the time needed to perform computations. Firstly, integration tolerances are relaxed of a couple of order of magnitudes. This modification fixes also some problems related to infinite time integration when altitude approaches ground level. Then, having identified that the NRLMSISE-00 density model is quite heavy from a computational point of view, the atmospheric values computed during a certain trajectory integration are stored and reused in those modules that apply to the same trajectory. If necessary, values are interpolated for altitudes different from the ones that correspond to the discretization of the primary trajectory. Finally, for the trajectories of falling elements or fragments that pass through lower altitudes, the integration scheme *ode87* is changed into *ode45*. This substitution gives a quite good time saving and at the same time preserves the accuracy on the calculated points.

3.3. Break-up model

The breakup event coincides with the disintegration of the vehicle, but it is far from being instantaneous. As a space object enters the Earth's atmosphere, it encounters a steadily increasing aerodynamic load that causes a sequence of failures, thus generating multiple fragments. The breakup instant coincides with the first massive breakup of the main body. Generally, elements with high area to mass ratio (e.g., solar panels or large antennae) detach at high altitudes due to dynamic loads, while the other components will each be exposed to the heating environment, then melt and come apart. Aluminum parts are completely consumed, empty steel and titanium tanks or the casings of solid rocket motors have instead a very good probability to reach the ground.

During the descent through the atmosphere, the combined effect of intense heating and aerodynamic load causes separation of elements. The effect on the material is twofold since the increasing temperature reduces the strength and the aerodynamic forces induce stress. Using a thermal criterion, an element disassociates when its average temperature reaches the melting point of the material. Using the stress/strength interference criterion, an element disassociates when the calculated aerodynamic stress exceeds the material strength. A combination between the two criteria would be more realistic but its applicability is arduous because there is lack of knowledge in relevant material properties such as room temperature strength and variation of strength with temperature. Moreover, aerodynamic stress is difficult to calculate and only a sort of proportionality with velocity and density could be assumed.

In this work, the thermal criterion is applied according to the assumption that an element that reaches the melt temperature undergoes mechanical failure due to a severely diminished strength modulus.

3.3.1. Breakup criterion

In the original work [2] elements are treated as independent. Thus, each element comes apart when it reaches its own material melt temperature. However, there would be a strong correlation among the separation altitudes of each element. If one element separates at a high altitude, for a particular set of parameter values, then other elements will tend to do the same. This is more evident if the exemplar case of the Delta II second stage is considered. The propellant tank is a massive component positioned at the center of the whole assembly and it is quite daring to conclude that it can disassociate while the rest of the vehicle remains intact.

According to this, the concept of structure is added to the model and the phenomenon of main breakup is simulated. The structural element is an approximation of the structure of the vehicle and represents connections between the main elements. The vehicle disassociation is initiated when the structure, typically made of aluminum, is heated to its melting temperature. Thus, the structure is no more able to keep together the components of the vehicle and they continue to fall independently.

3.4. Heating model

During the aero-braking process in the atmosphere, the initial potential and kinetic energy of the vehicle are converted into thermal energy which is consumed to the larger extent by the ambient atmosphere and to a smaller extent by the body. The aerothermal heating calculation methods can be divided into the following categories:

1. Semi-empirical/analytical correlations based on hypersonic boundary layer theory and developed from initially simple Newtonian theory, experimental data, and analytical developments of heat flux transfer.
2. Higher order methods including Direct Monte-Carlo Simulations for rarefied regime and completing Navier–Stokes with thermo-chemistry modeling associated with structural and thermal Finite Element Analysis (FEA).

Both methods require extensive testing in hypersonic facilities for validation. A simplified computational process with low calculation burden is more appropriate for a probabilistic analysis in a reentry mission scenario. Thus, the method of correlations is preferred. Aerodynamic heating will be considered only for the case of laminar hypersonic continuum flow. The reentry objects are assumed as random tumbling and with infinite heat conductivity resulting in a uniform heat load and a uniform temperature distribution on the overall surface. Also the conductive heat flux from the shell to the internal structure is neglected. The chosen model neglects chemical reactions at the surface of the object such as metal oxidation or molecular recombination.

3.4.1. Stagnation point heating

Stagnation point heating is the main mode of heat transfer for bodies reentering the atmosphere and arises from a combination of thermal and aerodynamic effects. Many of the correlations for stagnation point heating find their roots in Fay and Riddell's theory and the work of others at Avco Research Laboratory since the 1950's. The Fay-Riddell theory, which usually assumes boundary layers which were either in chemical equilibrium or frozen with the wall considered to be either fully-catalytic or non-catalytic, reduces a set of general boundary-layer equations for stagnation point heating into nonlinear ordinary differential equations for a broad flight regime. The cold-wall heat flux is averaged over the surface of the debris fragment by the fraction of instantaneous cold-wall flux at the stagnation point. Such fraction is quantified by an area averaging factor, that is assumed from available data according to the shape and tumbling mode of reentry debris. [16]

3.4.2. Detra, Kemp and Riddell correlation

Detra, Kemp and Riddell have proposed an interpolation formula fitted with the AVCO shock tube data. The heat transfer coefficient for the convection term is:

$$h_{conv} = \frac{D}{\sqrt{R}(T_0 - 300)} \cdot \left(\frac{\rho}{\rho_{ref}}\right)^{0.5} \cdot \left(\frac{V}{V_{ref}}\right)^{3.15} \tag{3.1}$$

where D is the Detra–Kemp–Riddell coefficient, R is the heating radius, T_0 is the air total temperature, ρ is the free-stream density, ρ_{ref} is the reference density, V is the free-stream velocity and V_{ref} is the reference velocity.

The correlation is recommended for theoretical predictions of the laminar, hypersonic, convective stagnation point heating rate of spherical nose shapes in a continuum flow. It is an exact formulation that takes into account the high temperature dissociation phenomena. The equation has an accuracy of ± 10% for velocities above 2000 m/s from sea level to altitudes at which the continuum flow assumption is still valid. [17]

3.4.3. Heat balance

The thermal destructive process of an object will depend on the heat input profile during reentry and on the thermal response of the object. The latter combines heat storage and heat loss. A complete heat balance equation should include in addition to convective and radiative heat transfer, the effects of conduction through the material if it is not isothermal, loss of heat to the interior by conduction through joints and structural members, loss of heat by radiation to and convection in any interior space. For many purposes it is sufficient to balance the aerodynamic convective heating of the surface and the radiative cooling effect and thus obtain an upper limit to the equilibrium temperature. [18]

Assuming infinite heat conduction within the body, the energy balance equation for a local wall element is:

$$\dot{q} = \dot{q}_{conv} + \dot{q}_{rad} \tag{3.2}$$

where $\dot{q}_{conv}$ is the convective heat flux and $\dot{q}_{rad}$ is the radiated heat flux.

Temperature change with convective heating and radiative cooling is governed by the equation (3.3):

$$\dot{T} = \frac{A}{m \cdot c_P} \left[OF \cdot h \cdot (T_0 - T) - \varepsilon \cdot \sigma \cdot T^4 \right] \tag{3.3}$$

where T is the wall temperature, A is the heating (wetted) area, m is the item mass, c_P is the material specific heat, OF is the heat transfer orientation factor, h is the convective heat transfer coefficient, T_0 is the air total temperature, ε is the material emissivity and σ is the Stefan–Boltzmann constant.

The wall temperature, because of the lumped-mass assumption, is coincident with the temperature of the body. The air total temperature is computed using the equations for an isoentropic flow and calorically perfect gas. Even if this is a bad approximation because air is calorically imperfect in the hypersonic regime, the difference between values is small especially for low Mach number [19].

3.5. Ablation model

Ablation is a complex process that begins when the external surface of the body has reached the melt temperature. At that point, the additional absorbed heat triggers the mechanism of sublimation of external layer of material and melting of the subsequent layer. Despite the phenomena of thermal and chemical interactions between layers, the mass loss is determined taking into account only the external net heat flux and the heat of fusion of the material. Thus, the heat of ablation is the heat required to melt the entire body, once its bulk temperature has raised from the initial temperature to the melt temperature.

The rate of mass loss due to ablation is:

$$\dot{m} = -\frac{\dot{q}}{H_f} \tag{3.4}$$

where $\dot{q}$ is the net heat flux and H_f is the heat of fusion.

The net heat flux, once the material reaches melt temperature T_m, is given by:

$$\dot{q} = A \cdot [OF \cdot h \cdot (T_0 - T_m) - \varepsilon \cdot \sigma \cdot {T_m}^4] \tag{3.5}$$

The ablation process is stopped either if the remaining mass is zero or the net heat flux becomes negative. For a body ablating during reentry, molten material will be removed from the body in some fashion by aerodynamic forces. The removed material is assumed to demise due to augmented thermal exposure. During the ablation process, it is assumed that the shape, area and ballistic properties of the body do not change.

3.5.1. Demise criterion

The term *demise* denotes when a reentering body or a fragment thereof has completely melted. This is of practical interest because a body that has melted away cannot strike the ground and contribute to the casualty area. In this analysis, demise happens when the amount of mass loss due to ablation is equal to the initial mass of the considered element.

3.6. Fragmentation

Elements may also fragment into smaller pieces. The number of fragments and their area may be treated as a random variable in that different reentries would be expected to produce different fragments of the same element.

According to the original work [2], fragmentation of an element is assumed to occur at the altitude at which the parent element separates from the vehicle. Actually, the implemented model identifies the separation of an element at the altitude of structural disassociation, though the element itself has not reached the melting temperature. In order to maintain the agreement with the original argumentation, the altitude at which fragmentation occurs is set equal to the altitude at which a separated element reaches the fusion temperature. This assumption matches the concept of secondary breakup and fragmentation event, since an element, that reaches the melting temperature of its material, can no longer sustain the stress caused by aerodynamic loads. This is why all the fragments generated from the same element are propagated starting from a common altitude, i.e. the fusion altitude of the parent element.

Practically, the trajectory of each separated element is propagated till ground, then the heating module is applied to determine at which altitude the element reaches the melting temperature. Finally, the ablation module is applied to determine whether the element demises or reaches the ground. The final mass is stored because it will be used to estimate the number and properties of fragments. Having determined the range of fragments from each element–altitude pair that might survive to hit the ground, the reentry model is again applied to each fragment. Thus, the fragmentation module determines if each fragment within the range does indeed survive. The surviving size and projected area onto the ground of each potential fragment of each altitude–element pair are recorded for further risk analysis.

3.6.1. Number of Fragments

The problem of estimating the potential number of fragments is solved by the definition of a uniform probability distribution connected to the knowledge of calculated element ablation from the above modules. Supposing that calculations found that a certain percentage of an element had ablated, the lower bound number of fragments an element can break into and still survive to hit the ground is one, while the upper bound number may be estimated as a function of the calculated amount of ablation. In particular, it would be possible that fragments of total mass equal to the final mass of the corresponding element have survived. This statement complies with the result of the ablation module, since for the single reentry the total mass of surviving fragments should not be higher than the final mass of the parent element. So, the maximum number of fragments for each element can be defined as:

$$n_{max}^{frag} = \frac{1}{1 - p_{abl}} - 1 \tag{3.6}$$

where p_{abl} is the percentage of ablated mass with respect to the element initial mass. The adopted formula states that if the amount of mass ablation from the parent element is high, then the number of fragments would be high too. This is supported by the assumption that an hollow element with very lowered thickness of its surface would not be able to sustain the external aerodynamic loads due to reduced structural strength. Conversely, if the percentage of ablation is small, the structural integrity of the element is preserved and it would be more likely to remain intact or produce few fragments during reentry.

3.6.2. Fragments properties

Fragments properties shall be redefined because they are different from the corresponding element properties. The fragmentation event randomly divides the element in parts, that have the same material but different shape and mass, even between them.

The initial mass of each fragment is defined inside an iterative process, sampling its value from a uniform distribution that goes from zero to a variable upper bound, with extremes excluded. The upper bound is the residual mass that comes out from the difference between the initial mass of the element and the total mass of previously defined fragments.

The definition of the geometric and ballistic properties of each fragment depends on the value of initial mass of the fragment itself. In particular, a fragment can belong to three categories according to the level of mass percentage with respect to the initial mass of the parent element, as shown in Table 3.1.

mass %	**0 → 20**	**20 → 70**	**70 → 100**
shape	plate	hemisphere	as element
$\boldsymbol{C_d}$	1.4	0.93	as element
$\boldsymbol{A_{cross}}$	A_{tot}^{frag}	$\frac{1}{2}A_{cross}^{ele}$	A_{cross}^{ele}
$\boldsymbol{A_{tot}}$	proportional	proportional	proportional

Table 3.1: Categories for selection of fragment properties

The first category approximates the fragment as a plate, because a mass percentage under 20% corresponds to a piece of the parent element with a small curvature. The drag coefficient is set equal to the one of a thin plate in hypersonic flow and the cross section is set equal to the wetted surface of the plate. The second category applies to values between 20% and 70% and considers fragments to be similar to an hemispherical shell. The drag coefficient is set equal to an average value of an hemisphere in hypersonic flow and the cross section is set equal to one half the one of the element. The last category corresponds to values above 70% in mass and considers fragments so similar to the element that ballistic coefficient and cross sectional area are taken as the same. In all categories, the value of wetted area used in thermal calculations is computed with a geometric proportion based on the fragment mass to element mass ratio.

3.7. Uncertainties treatment

The probabilistic framework is built such that a large number of reentry trajectories is simulated, each with a different randomly selected set of variables and parameters. Calculations, therefore, involve uncertainties in the models as well as in the physical properties and model parameters. These uncertainties are reflected in a large variation over casualty area, impact location and other intermediate outcomes such as disassembly altitude. Uncertainties are included replacing assumptions with probability distributions that represent the range of knowledge and the inherent stochastic variability of the reentry problem.

Some of the most significant unknowns are the trim orientations of the spacecraft and of the independently falling elements. Orientation of a ballistic body means the way it is moving on its axes and the way it is moving relative to the free stream velocity vector. For example, a cylinder-shaped tank may be spinning on its long axis with its velocity vector normal to this axis (broadside spinning), tumbling end over end on its short axis, spinning and tumbling and/or precessing, not spinning such that it presents a single face of the cylinder to the air-stream (either broadside stable or end-on stable), or angled end-on such that the stable trim orientation yields an acute angle between the plane perpendicular to the cylinder axis and the air stream. In order to capture the uncertainty in orientation, the parameters for drag coefficient and heat transfer orientation are used. The sampling procedure selects an orientation at the beginning of a trial and then the trajectory, heating and disassembly associated with this orientation are simulated. A large number of trials results in a large number of possible trajectories.

Table 3.2 shows the set of uncertain parameters used in this study along with the basis for estimating median values and uncertainties. The meaning of each parameter is explained in the next sections.

Parameter	Distribution	Median value	Limits
Drag coefficient (vehicle)	Fixed	According to nominal impact point location	-
Drag coefficient (element)	Uniform	Reference shape in hypersonic flow	±10% of median
Specific heat	Normal	Reference alloy	±10% of median
Melt temperature	Normal	Reference alloy	±10% of median
Heat of fusion	Normal	Reference alloy	±10% of median
Emissivity	Normal	Reference alloy	±10% of median
Orientation factor (inside)	Triangular	Assumed vehicle orientation	Variations owing to possible alternative orientations
Orientation factor (outside)	Triangular	Assumed element orientation	Variations owing to possible alternative orientations

Table 3.2: Uncertain parameters treated in the algorithm

3.7.1. Ballistic properties

The ballistic coefficient is a critical parameter since it directly affects the calculation of aerodynamic drag force. A small variation in the ballistic coefficient results in a large variation in the trajectory path and impact point location. Ballistic properties depend on drag coefficient, cross section and mass of the considered body. In this model, only uncertainty in the drag coefficient is considered, because its variability depends on orientation, flow properties and regimes that actually could change a lot during the whole reentry path. Also mass and shape values are subjected to variability due to partial knowledge of spacecraft properties, but their definition has the purpose of identifying a class of vehicle rather than a specific one.

As shown in Table 3.2, two values of drag coefficient are set. The first represents the intact reentry vehicle and its variability will affect the nominal trajectory. The second represents the generic element and its variability will affect the trajectory after the separation event. Fragments, as explained in Section 3.6.2, will have a value of drag coefficient according to their initial mass.

It is important to remark that a simulation performed by this reentry model considers the variability of the drag coefficient of the elements while keeping fixed the one of the reentry vehicle. The reason of this choice lies firstly in the fact that the main purpose of the work is to investigate the uncertainty of one reentry event defined by a certain nominal trajectory and secondly in the attempt to reduce the computational burden of the simulation. Anyhow, a sensitive analysis could be done on the effect of spacecraft drag coefficient variability on the nominal trajectory and then run the entire simulation only for specific cases of interest such as those in which the nominal impact point is located near critical regions or near the coastline.

3.7.2. Thermal properties

Thermal parameters directly affect the results of heating and ablation modules. A different initial set modifies the profile of body temperature or mass loss during reentry, producing a completely different outcome of the reentry event. In fact, considering an element that in a previous trial has demised, different initial parameters could make it reach a different percentage of ablation or not even reach the melting temperature, impacting the Earth while still intact. For these reasons, it is fundamental for the validity of the probabilistic model that uncertainties on thermal parameters are included. The most important are specific heat, melt temperature, heat of fusion, emissivity and heat transfer orientation factor.

Material properties are dependant on the selection of the proper material for each component. The reentry vehicle could be classified or its components not completely known, therefore classes of vehicle are simulated. Anyhow, even if the material for each element is set, many alloys and treatments of the same material or different surface finishes exist, so uncertainties in material properties shall be considered.

The heat transfer orientation factor requires a separate discussion. The orientation of a spacecraft, as well as an element, is highly variable and therefore poorly predictable. As shown in Table 3.2, two distributions are actually set to distinguish the phase in which the element is still attached to the main vehicle (*inside*) from the phase in which it is falling on a separated trajectory (*outside*). In addition, the sampling procedure of the orientation factor of an element still inside the vehicle is repeated for each element, so that the values in each trial are different among the elements and also different from the one of the vehicle itself, even if the base distribution is the same. This distinction is done to account for the different heat flux that hits each element according to its position on the main vehicle and the possibility of shielding or shadowing. Moreover, the thermal model computes the temperature variation of the element even when it is still attached to the vehicle considering it directly exposed to the external flux. This is done because the structural element could be of various forms, for example a motor casing or simply a truss structure, as in the case of Delta II 2nd stage, but in the present model it is a fictitious item for the breakup instant determination.

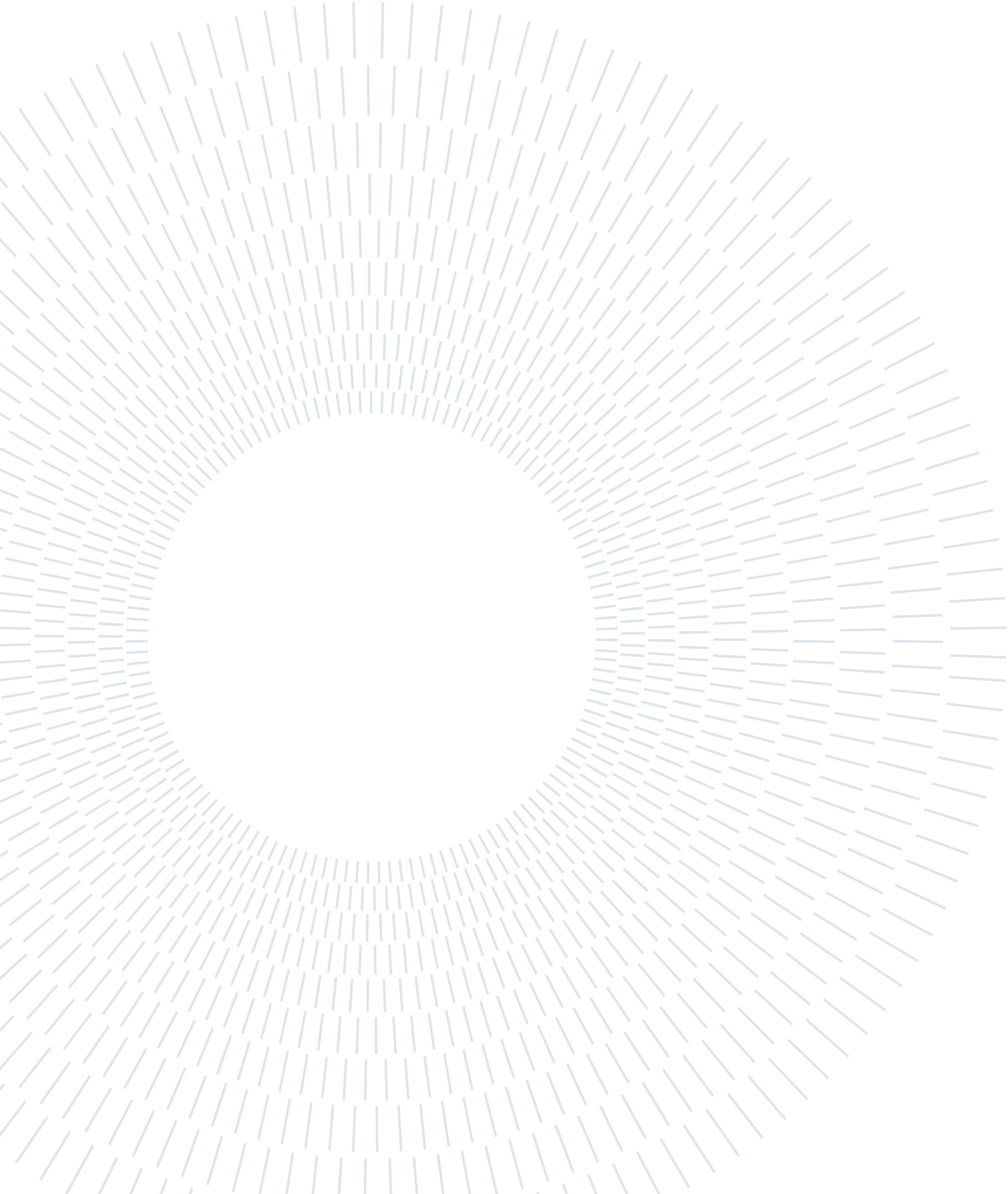

4 | SARUS algorithm

This chapter describes in detail the architecture of the Survivability Analysis of Reentering Upper Stages (SARUS) algorithm. After an overview of the main structure, the initial conditions and parameters needed for the execution are presented. Then, the working principle of each specific module is explained and input and output variables are listed.

4.1. Main structure

The structure of SARUS is shown in Figure 4.1.

The first part is devoted to loading and defining all the parameters needed for the execution of the main modules. Before starting the simulation phase, a preparatory procedure defines the properties of each element collecting values from a database, samples and stores the uncertain parameters that will be used in each iteration, computes and stores the nominal trajectory of the vehicle and then sets the number of trials. For each simulated reentry, firstly the separation module is run twice to compute the breakup altitude of the structure and the instants at which both the structure and the element reach the melt temperature. Then the instants are compared because there are two options: an element separates when the structure breaks or an element separates before the structure breakdown. The former means that the element has not reached the melting temperature, hence the next steps are checking if it reaches the fusion temperature before impacting, computing the percentage of ablation and, if the element does not demise, applying the fragmentation module. The latter corresponds to separation of the element from the main structure of the vehicle because its material reaches the melt temperature. Therefore, the ablation module is run right after the separation and then, if the element does not demise, the fragmentation module is applied. The second option is more likely to occur at components made of aluminum well exposed to the external flux, such as a guidance navigation box. Finally, the outcomes are stored for each element and for each trial in order to reconstruct the trend of quantities of interest over the entire simulation for the whole vehicle rather than for each single component. If an element does not reach the fusion temperature during reentry, it will impact following the nominal trajectory with initial values of area and mass.

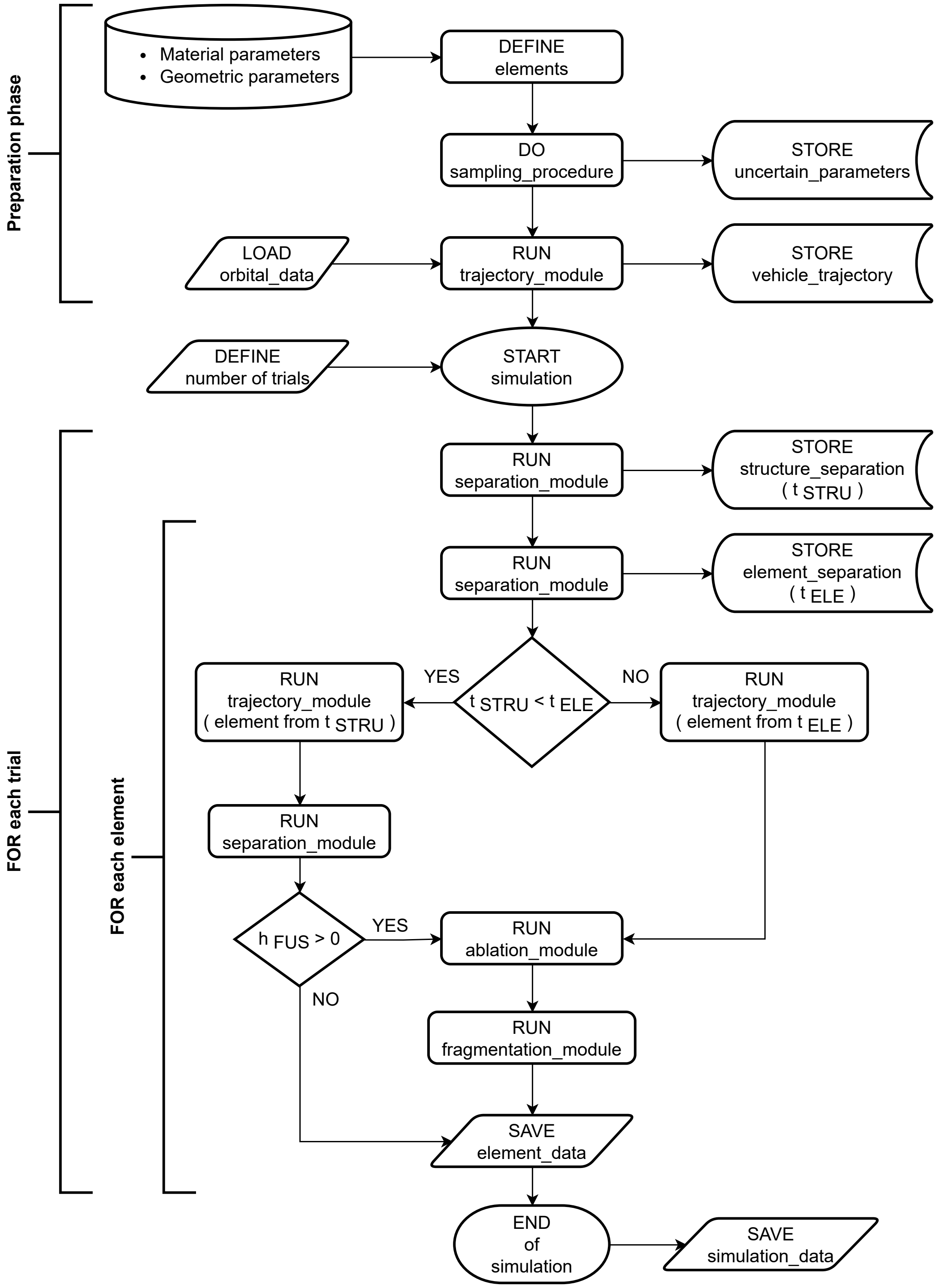

Figure 4.1: Main structure of SARUS

The logic of the implemented code is shown in Algorithm 4.1.

Algorithm 4.1 SARUS: Survivability Analysis of Reentering Upper Stages

```
Initial instructions
Load orbital data
Load geometric parameters
Load materials parameters
Define the list of elements
Define the number of reentries
Sampling of parameters for elements and structure
Trajectory module → vehicle
for each reentry do
    Load structure parameters
    Separation module → structure
    for each element do
        Load element parameters
        Separation module → element
        if $t_{sep}^{STR} < t_{sep}^{ELE}$ then
            Trajectory module → element ← $t_{sep}^{STRU}$
            Separation module → element
            if element melt temperature then
                Ablation module → element
                Fragmentation module
            end if
        else
            Trajectory module → element ← $t_{sep}^{ELE}$
            Ablation module → element
            Fragmentation module
        end if
        Save element outcomes
    end for
    Save simulation outcomes
end for
```

4.2. Initial conditions

The initial instructions are essential for defining the working parameters of the modules of the algorithm. Moreover, the components of the reentry vehicle shall be stated in terms of geometry and material before the simulation starts.

The orbital data are the epoch at which the simulation will start and the corresponding state vector of the vehicle, consisting of position and velocity in ECI frame. Geometric parameters define size, mass and ballistic properties of each element. In particular, they can be grouped in quantities for general purpose such as initial mass, largest cross section area and average drag coefficient in hypersonic flow and quantities for the thermal calculations such as wetted area, nose radius and heat transfer orientation factor. The list of materials contains the most common alloys used for components of upper stages. The parameters needed for each material are specific heat, thermal emissivity, melting temperature and heat of fusion. Elements are defined as a combination of geometry and material. In particular, the shape of a component is modeled as the most similar geometry among the simple ones (cylinder, sphere, box or plate).

4.3. Trajectory module

The module that computes the trajectory is applied to three different types of object and in two different contexts during reentry. Before the simulation framework, it computes the nominal trajectory of the intact vehicle from the initial orbital position to ground. Inside the iterative loops, it calculates the trajectory of each element from the altitude of separation and, eventually, of each fragment generated.

The numerical integration of the trajectory is performed by the AIDA propagator. The following assumptions are made for the analyses: the degree and order of the gravitational spherical harmonics is set to 10 and tides are disabled; the atmospheric drag accounts for the rotating atmosphere, but winds are not considered; third bodies attraction and solar radiation pressure are not considered. Integration tolerances are set to 10^{-10} (absolute) and 10^{-11} (relative).

4.3.1. Reentry phases

The overall trajectory is conceptually divided into orbital phase and reentry phase. The former refers to the phase in which the vehicle is still on its orbit and the perigee is gradually lowered by the effect of atmospheric drag. The latter coincides with the parabolic path of the vehicle, once it has definitely left its orbit, beginning the descent through the atmosphere. The threshold between the two phases is chosen to be the altitude at which conventionally the reentry begins (120 km). Such distinction allows to treat the two phases with a different integration step. The orbital motion is computed at every minute, because it can takes many orbital passages to decay, so the time between each calculated position is extended to reduce the computational effort. Instead, the reentry phase lasts less than an hour and it is characterized by critical events that shall be analyzed in detail. Therefore, the trajectory is computed at each second. This time lapse could seem inadequate since the speed is in the order of thousands of meters per second and so between one position and the next there would be some kilometers. This is true for the first part of the reentry trajectory but there the path is also smooth and so the decrease in altitude is anyhow low. Likewise the last part of the reentry path is steep but the speed becomes subsonic.

4.3.2. I/O variables

The trajectory module takes in input the initial state and epoch, the integration span and the geometric properties of the item. The outputs are the vectors containing time, position and velocity at all the computed points. In addition the module gives the vectors of temperature and density of the atmosphere along the trajectory as function of geographical coordinates and altitude. A condition is set on the altitude over the ellipsoid in order to stop the integration when the item impacts on ground.

4.4. Separation module

The separation module has the purpose of computing the altitude at which an element or fragment comes apart from the main body, exploiting a thermal criterion. Actually, the module can be applied in two different ways: if an element reaches the melt temperature before the main breakup event, it outputs the separation altitude, otherwise, if an element already detached due to the breakup of the structure, it can be used to compute the altitude at which the fusion temperature is reached.

The structure of the module is shown in Figure 4.2.

The module integrates the equation of temperature variation defined by the heating model. The stagnation temperature and the convective heat transfer coefficient are computed at any time step. Since these two variables depend on trajectory dependant quantities, the separation module needs to be connected to the trajectory one. For practical reasons and computational efficiency, the two modules are distinct but the outputs of the trajectory module are provided to the separation one and interpolated with respect to time because the integration time step can be different. In order to preserve the validity of the Detra, Kemp and Riddell correlation, a lower bound is set on the velocity. Values of heat transfer coefficient that correspond to values of speed under 1.5 km/s are set to zero. The integration scheme is ode45, since it is faster, and tolerances are set to 10^{-10} (absolute) and 10^{-11} (relative).

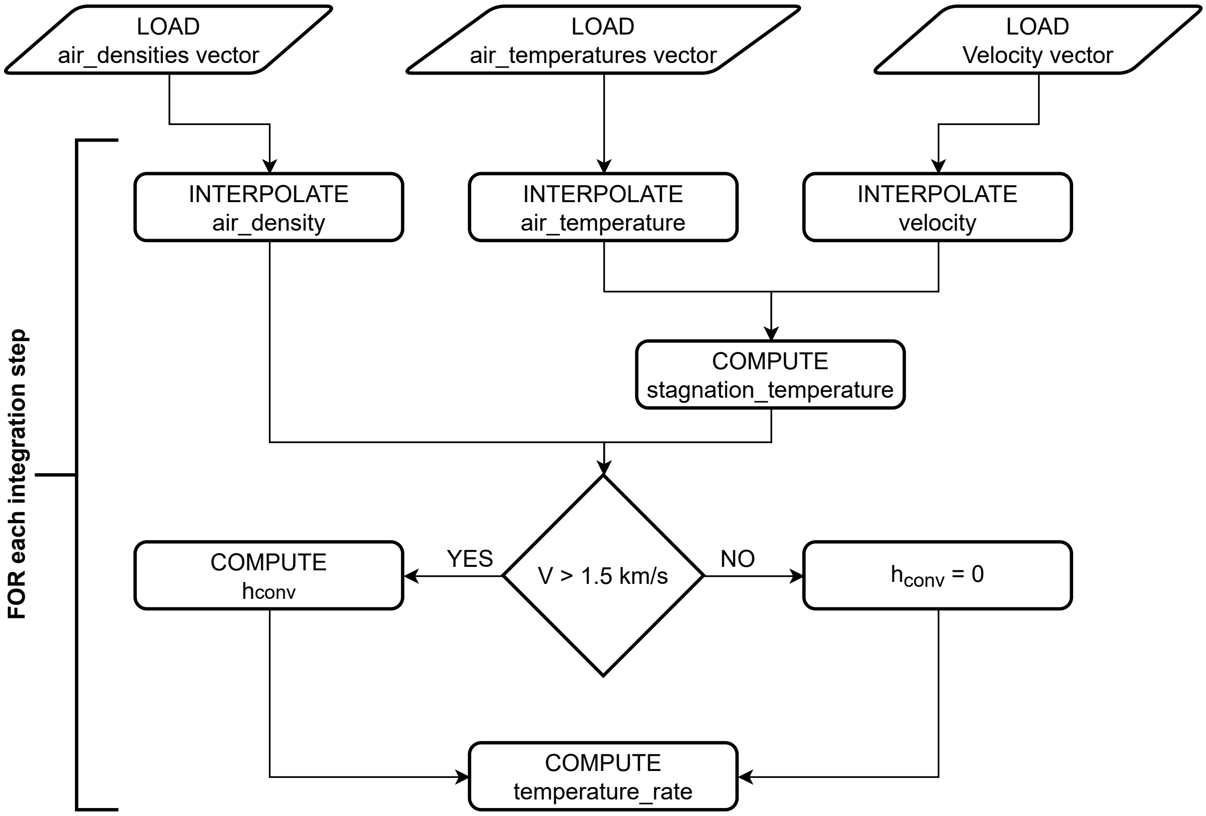

Figure 4.2: Structure of the separation module

4.4.1. I/O variables

The input variables are the initial temperature, the item properties and the vectors of velocity, air temperature and air density computed by the trajectory module along with the corresponding vector of times. In addition, the module accepts the values of specific heat, emissivity and heat transfer orientation factor sampled at each trial in order to account for uncertainties in the heating model. The initial temperature shall be specified according to the phase of the reentry. If the element is still attached to the vehicle, the initial temperature is set to 300 K, otherwise the initial temperature is equal to the one reached at the instant in which the structure breaks. The same dualism reflects on the orientation factor that belongs to different ranges according to the fact that the element is attached at or detached from the main body, as explained in Section 3.7.2. The stop condition is based either on an altitude limit or on a temperature limit. Hence, the integration ends either if the material melt temperature is reached or the element impacts on ground. The module gives in output the values of temperature at each time step till the stop condition.

4.5. Ablation module

The ablation module applies after an element or a fragment has reached the melting temperature. The underlying principle is that additional heat absorbed by the item causes a mass loss according to the material heat of fusion. According to this, only positive values of the net heat flux are considered, otherwise the mass loss rate is set to zero.

The structure of the module is shown in Figure 4.3.

The module integrates the equation of mass variation defined by the ablation model. The stagnation temperature and the convective heat transfer coefficient are computed at any time step, relying on the outputs of trajectory module with the same method described in the section of separation module. In this case, the previously computed trajectory is related to the item alone. As the previous module, a lower bound is set on the velocity and also the same integration scheme and tolerances are used.

4.5.1. I/O variables

The module takes in input the initial mass, the item properties and the vectors of velocity, air temperature and air density computed by the trajectory module along with the corresponding vector of time and the sampled thermal parameters in order to account for uncertainties. The orientation factor assumes two different values whether the element is still attached at or detached from the main body, as explained in Section 3.7.2. The stop condition is based either on an altitude limit or on a mass limit. Hence, the integration ends either if the item demises, thus the mass reaches zero, or the element impacts on ground. Moreover, the net heat flux is also monitored and when it is no more positive the module is ended. The module gives in output the values of mass at each time step till the stop condition.

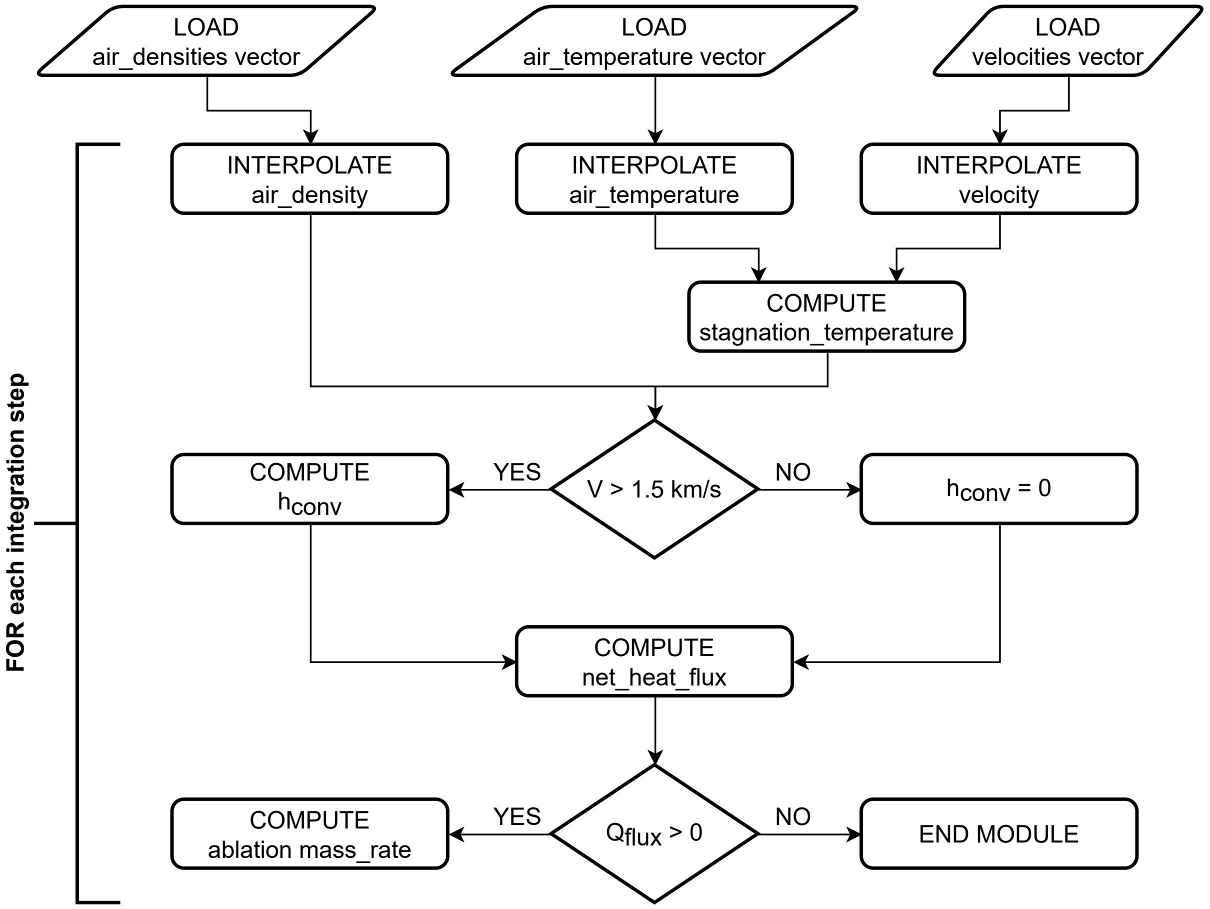

Figure 4.3: Structure of the ablation module

4.6. Fragmentation module

The fragmentation module is activated only if an element undergoes ablation. In fact, fragments can generate according to the phenomenon of mass loss from the parent element. A trigger condition is set: the final mass of the element must be higher than zero and lower than the initial value.

The structure of the module is shown in Figure 4.4.

Firstly, the number of fragments are sampled from a uniform probability distribution whose upper limit is dependent on the percentage of ablation the element would suffer if it was not allowed to fragment. Then for each fragment the initial mass is sampled from a uniform probability distribution whose upper limit is dependent on the residual mass. Hence, the properties of the fragments are determined starting from sampled values of mass and corresponding element properties, as explained in Section 3.6.2. In particular, drag coefficient, initial cross section and wetted area are computed for each fragment. Then, the trajectory module and ablation module are applied in sequence in order to understand if each fragment demises or impacts the ground. The initial state of a fragment is defined by the position and velocity at which the parent element reaches the fusion temperature, as explained in Section 3.6. The separation module is not applied in this phase because the initial temperature of each fragment is already the melting temperature. If the condition on the final mass is satisfied, the final state of the fragment is stored, otherwise it is discarded and so it does not contribute to the casualty computation.

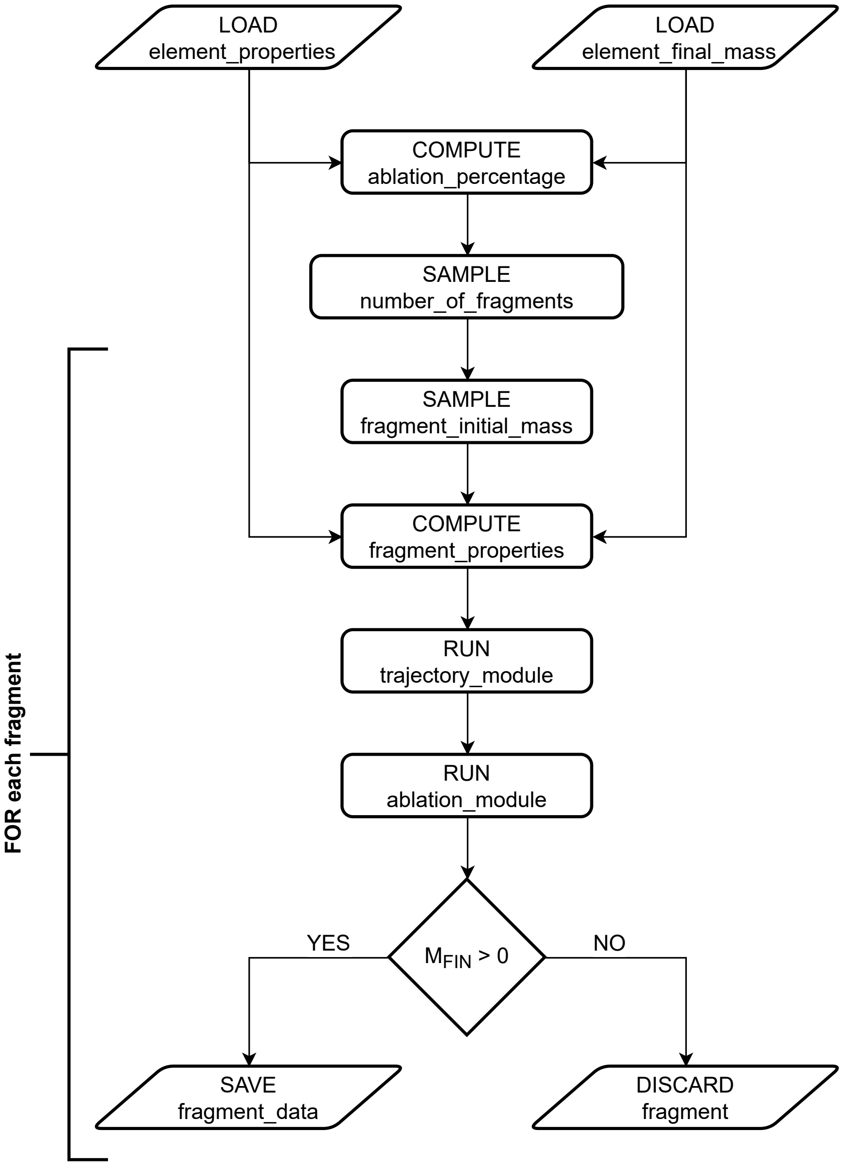

Figure 4.4: Structure of the fragmentation module

4.6.1. I/O variables

The inputs of the module are initial and final mass of the element, the epoch and state vector of the parent element as it reaches the fusion temperature, the properties of the element. The integration scheme is ode45, since it is faster, and tolerances are set to 10^{-10} (absolute) and 10^{-11} (relative). Similar to the ablation module, the stop condition is based either on an altitude limit or on a mass limit. Hence, the integration ends either if the item demises, i.e. the mass reaches zero, or the element impacts on ground. The module outputs the list of generated fragments with the corresponding values of initial and final mass, the initial cross section, the coordinates and altitude of the end of the trajectory.

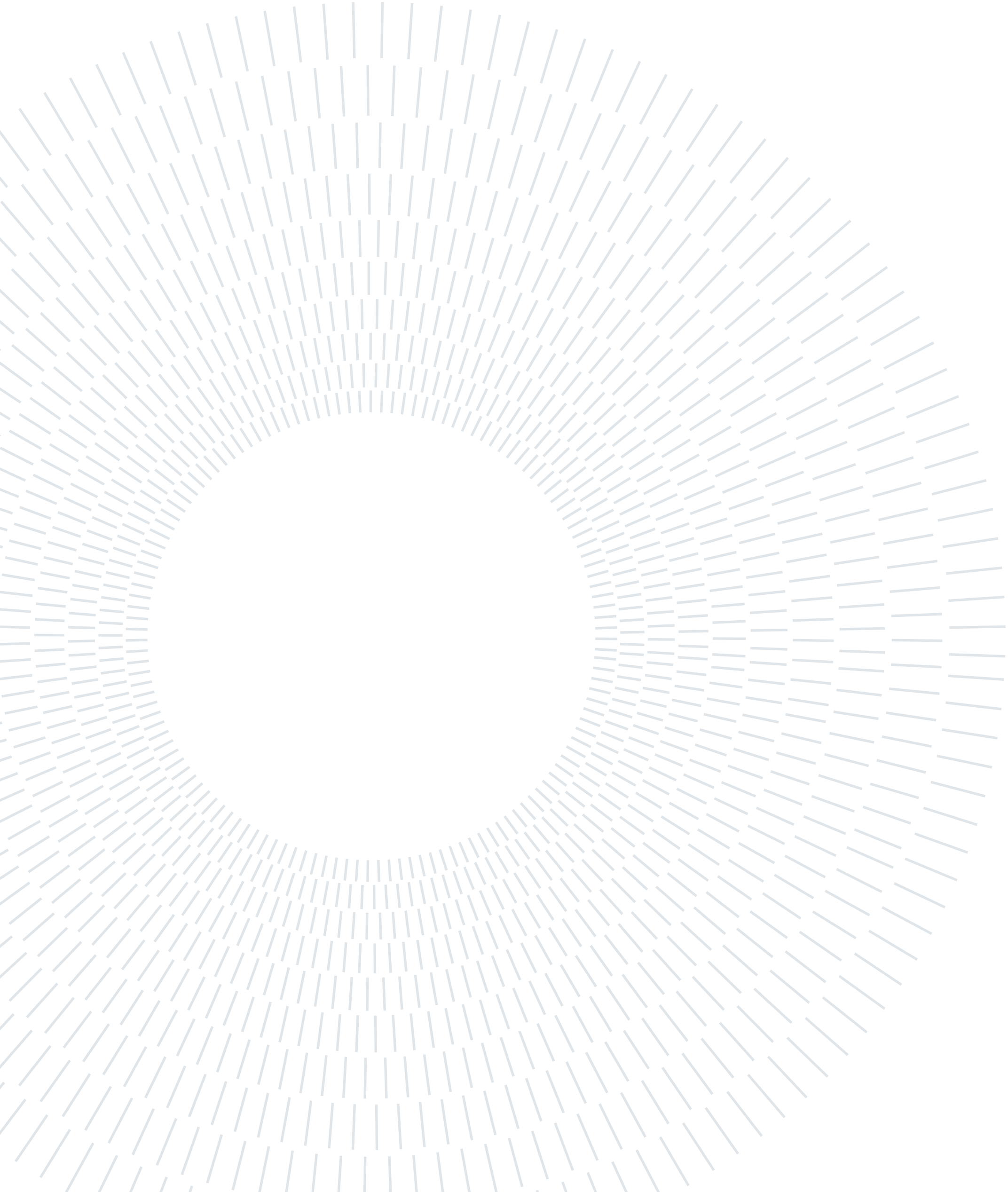

5 | Results

5.1. Simulation environment

This section contains all the parameters and initial conditions that represent the base case used for testing the algorithm. The simulation is based on the Monte Carlo method. In particular, keeping fixed the nominal trajectory, one-hundred trials are run. Each trial differs from the others according to parameters sampling, so that for one reentry event many possible outcomes are computed. The target of the simulation is the prediction of the casualty area and footprint distributions of a reentering upper stage vehicle. Once coupled, these two results grant the estimation of casualty risk associated to the analyzed reentry event. In order to account for the lack of knowledge in the precise values of parameters, the model relies on some assumptions. The most critical ones come from the vehicle modeling and the selection of ballistic and thermal parameters.

5.1.1. Vehicle model

The typical Delta II second stage vehicle, also called the Delta-K stage, is characterized by a large propellant tank in the middle of the vehicle with the guidance system and miniskirt mounted of the forward end, and the Aerojet AJ10-118K engine mounted on the aft end. Four helium and nitrogen pressurized vessels are also mounted on the aft end. The components are modelled in the following way: the guidance system as a cylindrical box, the propellant tank as a cylinder with two hemispherical caps, the pressurized tanks as spheres and the combustion chamber as an hollow cylinder. Moreover, connections and structural elements are combined in a single structural element that partially surrounds the vehicle and it is modelled as an hollow cylinder. Only one for each couple of pressurized spheres is considered in the simulation. The list of components is shown in Table 5.1.

Component	**Material**	**Shape**	**Mass** $[kg]$	**Diameter** $[m]$	**Length** $[m]$
Propellant Tank	AISI-410	Cylindrical	250.0	1.74	2.73
Large Sphere	Ti-6Al-4V	Sphere	30.4	0.59	-
Small Sphere	Ti-6Al-4V	Sphere	10.0	0.41	-
Combustion Chamber	AISI-410	Cylinder	50.0	0.30	0.60
Guidance Box	Aluminum	Cylindrical Box	100.0	1.20	0.50
Structural element	Aluminum	Cylinder	150.0	2.20	0.80

Table 5.1: List of simulated components from Delta II second stage

The weights of steel tank and titanium spheres are taken from data sheets. Instead, for each of the other components the weight is deduced from the total dry weight of the stage, that is about 920 kg, following a criterion based on proportions and range of values from available known components.

Regarding the engine of the stage, the nozzle is not considered because it should be designed to undergo complete ablation at the end of the burning phase. Instead, the combustion chamber is usually protected by an ablative coating, so only the main material will remain after the engine burn out and here it is assumed stainless steel. Materials and dimensions are taken from [20, 21].

5.1.2. Trajectory parameters

The initial state and epoch for the vehicle are taken from an historical reentry and adapted to reduce the number of orbital passages before the actual reentry event. Table 5.2 shows the initial conditions inferred from the initial state vector at the given epoch.

Date	**Position** $[km]$	**Velocity** $[\frac{km}{s}]$
2020 May 07 07:07:30	$[-2879.4, 5560.5, 1839.7]$	$[-6.0994, -1.6842, -4.6855]$

Table 5.2: Trajectory initial conditions

As already explained, the simulation performed by this reentry model considers the variability of the drag coefficient of elements while it keeps fixed the one of the reentry vehicle. Table 5.3 shows the mean values of drag coefficient assigned to each component and the resulting ballistic coefficient. In particular, the C_D value for the whole stage is a commonly used initial guess in trajectory analysis of unknown bodies. The values for spheres are taken as an average of the typical values assumed by such a shape in hypersonic continuum flow. Instead, the values for cylinders are calculated using a dedicated formula (5.1) based on the radius to length ratio, taken from [22].

$$C_D = 0.720 + 0.326 \cdot \left(\frac{2R}{L}\right) \tag{5.1}$$

	Drag Coefficient	**Ballistic Coefficient** $[\frac{kg}{m^2}]$
Stage	2.20	42.13
Propellant Tank	1.20	50.81
Large Sphere	0.92	120.86
Small Sphere	0.92	82.33
Combustion Chamber	1.50	185.19
Guidance Box	1.50	58.95

Table 5.3: Ballistic parameters of components

5.1.3. Thermal parameters

The most important thermal parameters are specific heat, melt temperature, heat of fusion, emissivity and heat transfer orientation factor. All but one depend on the material and their main values are indicated in Table 5.4. Instead, the orientation factor depends on the attitude that an item takes during the path through the atmosphere. Each trial considers one possible orientation factor, thus over the whole simulation many different values are investigated in order to effectively produce a range of all the possible attitudes. The distributions assumed for each modeled shape are reported in Table 5.5. The base case assumes that the most probable orientation of the spacecraft is a randomly tumbling hemisphere corresponding to a heat transfer orientation factor of 0.3 with an upper bound corresponding to a combination of a stable broadside and spinning sphere and a lower bound corresponding to a random spinning and tumbling cylinder. This distribution is assumed for all the elements when they are still attached to the main body. Instead, the probability distributions of the heat transfer orientation factor for elements falling apart is specified for each shape. The highest probability orientation of cylinders was broadside spinning corresponding to a heat transfer orientation factor of 0.3 with an upper bound corresponding to a broadside stagnation orientation and a lower bound corresponding to random spinning and tumbling. The highest probability orientation of spheres is stable broadside and spinning with an uncertainty of 20% around that value.

	AISI-410	**Ti-6Al-4V**	**Aluminum**
Specific Heat $[\frac{J}{kg \cdot K}]$	460	750	875
Melt Temperature $[K]$	1810	1900	933
Heat of Fusion $[\frac{J}{kg}]$	$2.75 \cdot 10^5$	$4.00 \cdot 10^5$	$3.00 \cdot 10^5$
Emissivity	0.38	0.30	0.14

Table 5.4: Thermal properties of selected materials

OF	**Distribution**	**Median value**	**Lower bound**	**Upper bound**
Vehicle	Triangular	0.3	0.2	0.4
Cylinder	Triangular	0.3	0.2	0.7
Sphere	Triangular	0.4	-20%	+20%

Table 5.5: Distributions of Orientation Factor

5.1.4. Sampling procedure

The sampling phase is done before the simulation starts. For each element a matrix of sampled parameters is built. Each matrix has as many rows as the number of uncertain parameters and as many columns as the number of trials. The procedure is repeated for the structural element. Then, inside the simulation, the columns of the matrix are recalled according to the current element and the number of the trial.

Since the simulation is of Monte Carlo type, the accuracy of results distribution is directly connected with the number of trials. The original work [23] relies on an amount of 2000 simulated reentries. In the present work, the number of trials is significatively lower, due to limited computational resources and available time. So, to understand the goodness of such a limited simulation, the distributions of sampled parameters are graphically analyzed and compared with the relative assumed distributions. Figures 5.1 and 5.2 show the distributions of sampled parameters for the structural element and the steel tank element respectively, highlighting the difference between assigned mean value and actual average value.

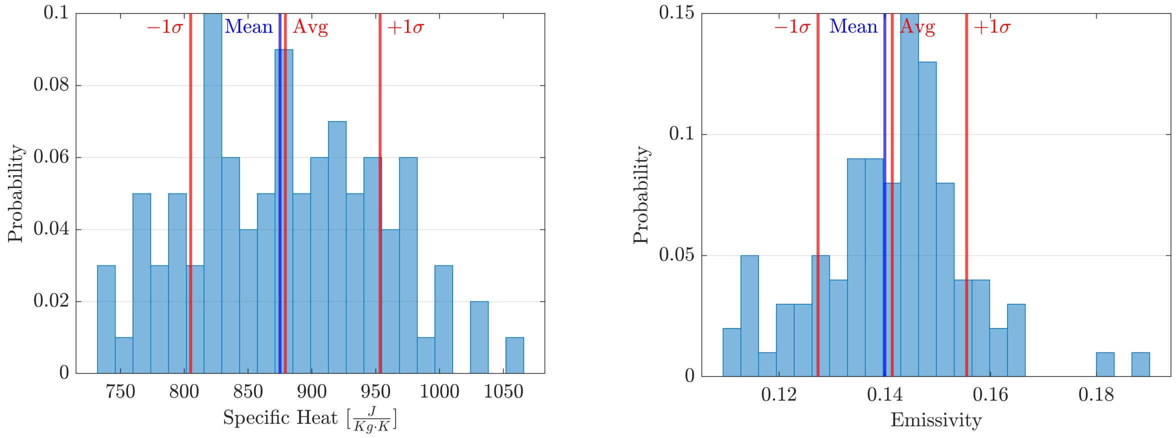

(a) Specific heat (b) Thermal emissivity

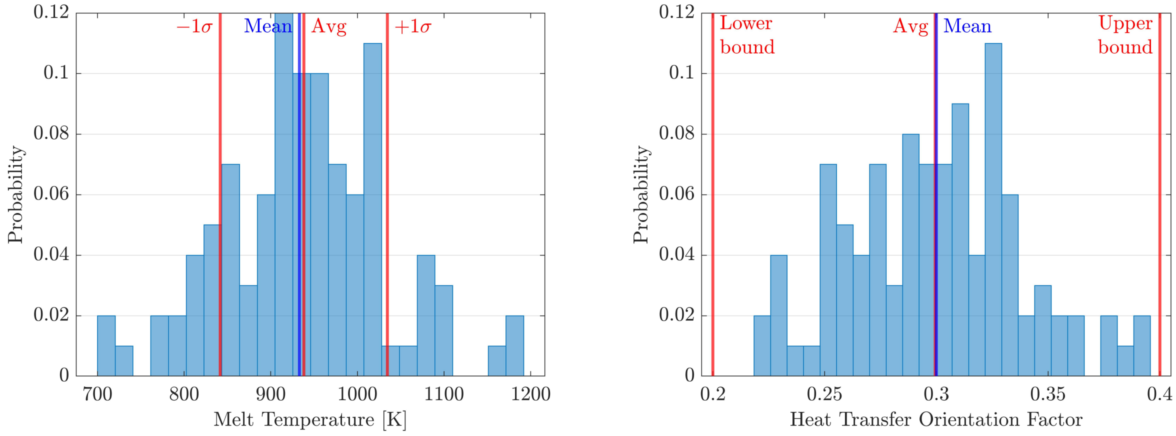

(c) Fusion temperature (d) Orientation Factor

Figure 5.1: Sampled parameters for the structural element

Despite the low number of samples, the distributions are quite acceptable and the mean and average values are always sufficiently close. Parameters in Figures 5.1a,b,c and 5.2a,b,c,d follow a normal distribution, while Figures 5.1d and 5.2f follow a triangular distribution that keeps the values between the specified edges. Finally, Figure 5.2e follows a triangular distribution but with the mean value shifted towards the left bound.

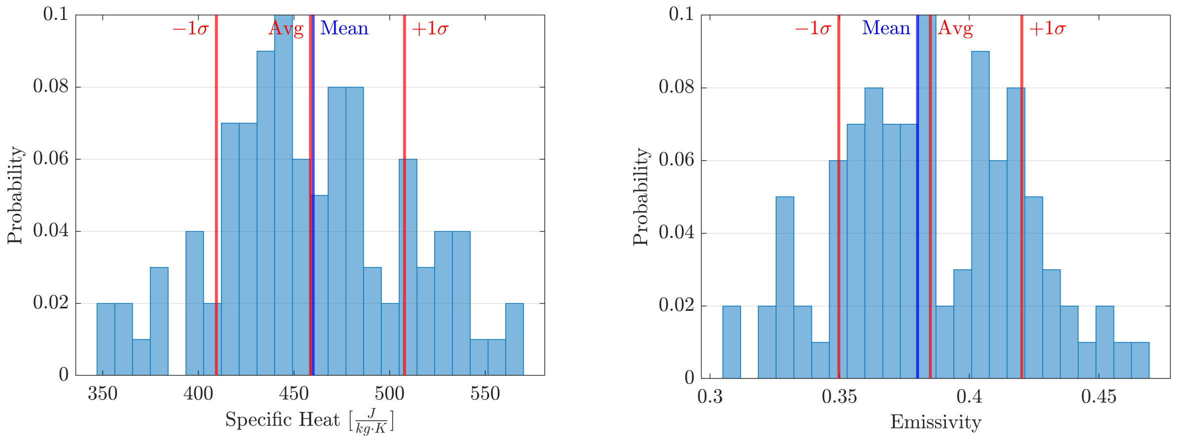

(a) Specific heat (b) Thermal emissivity

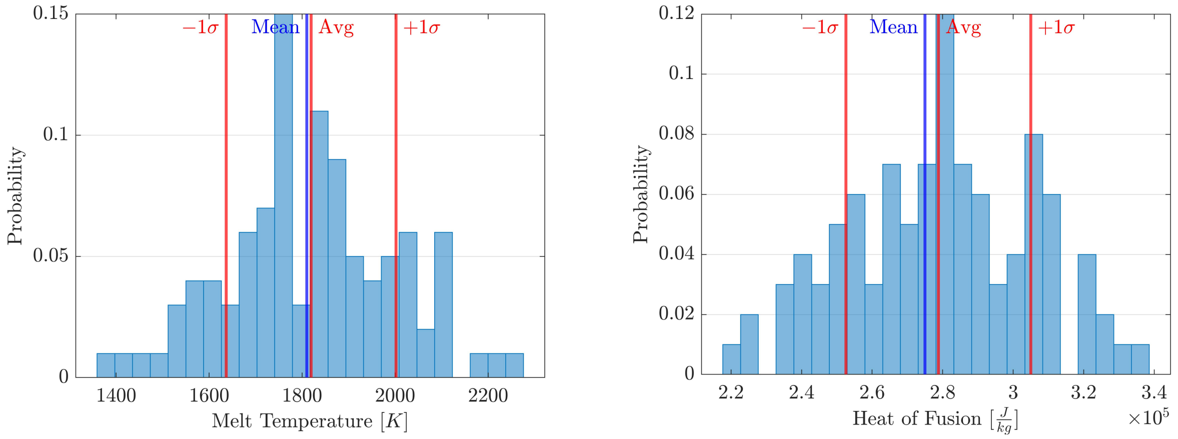

(c) Fusion temperature (d) Heat of fusion

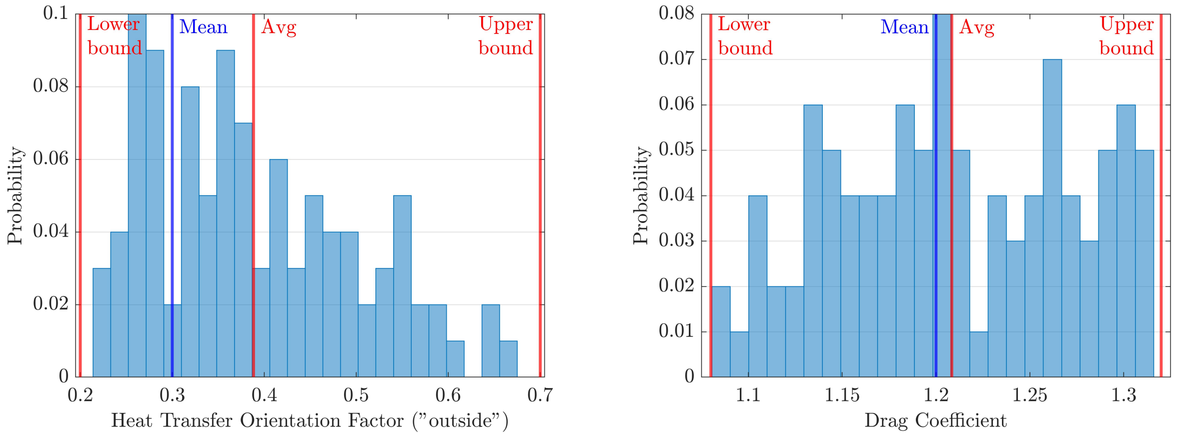

(e) Orientation Factor (f) Drag coefficient

Figure 5.2: Sampled parameters for the steel tank element

5.2. Nominal reentry trajectory

The base case of the simulation sets the initial conditions of Table 5.2 and a value of 2.2 for the drag coefficient of the reentering vehicle. The nominal reentry trajectory is calculated starting from those conditions accounting for the effects of gravitational attraction and drag perturbation. Figure 5.3 shows the altitude profile over the nominal reentry.

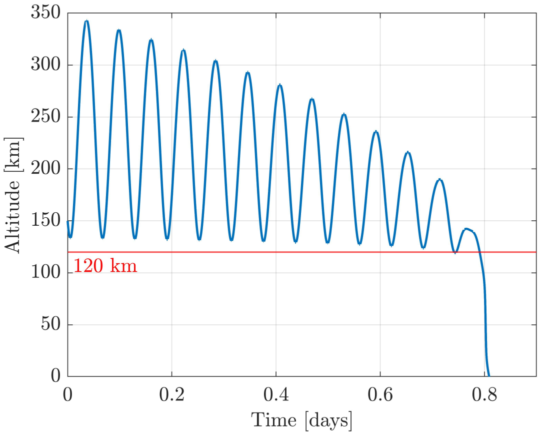

Figure 5.3: Altitude profile from the initial point to ground (base case with $C_D = 2.2$)

The orbital motion of the vehicle continues for about twelve revolutions, while the action of atmospheric drag lowers the apogee and tends to circularize the orbit. After the crossing of the common reentry altitude ($120km$) and the last perigee passage, the trajectory converts into an almost parabolic path, that identifies the reentry phase through the denser layers of the atmosphere.

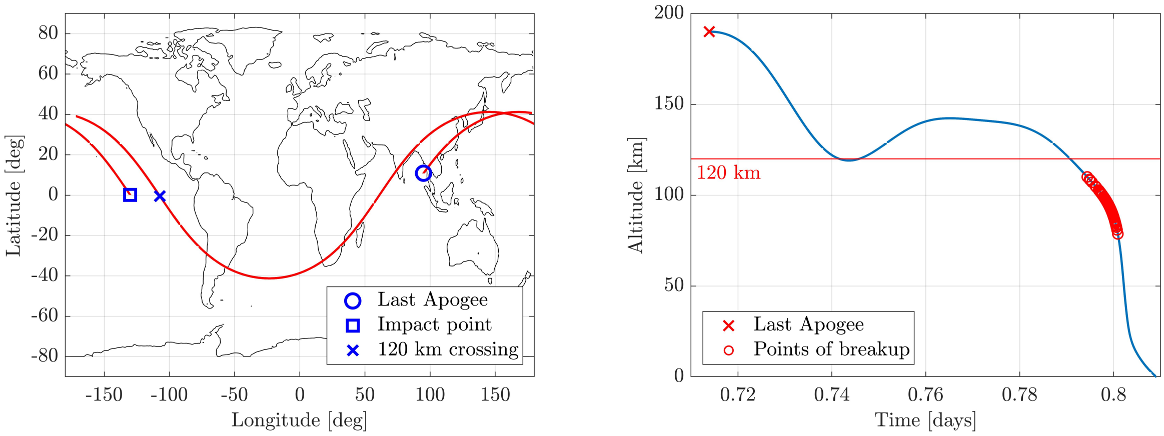

(a) Ground track (b) Altitude profile with breakup distribution

Figure 5.4: Trajectory from last apogee to ground (base case with $C_D = 2.2$)

In order to have a better look on the last phase, Figure 5.4 shows only the last part of the reentry trajectory, starting from the last apogee and ending in the impact point.

The first image, Figure 5.4a, represents the nominal ground track and some peculiar points. In particular, the point at which the vehicle crosses the altitude of 120 km is conventionally related to the reentry epoch. Therefore, it is evident that from the reentry point to the impact point the vehicle completes a full revolution of the Earth, visiting all of the latitudes bounded in the range defined by the inclination of the last orbital passages and so extending the risk to a very wide and global area.

The second image, Figure 5.4b, zooms in the last part of the altitude profile and overlaps the distribution of breakup points. In fact, nominal trajectory corresponds to the path followed by the intact vehicle from the initial position to the impact point. Along this trajectory the reentry algorithm computes the altitude of vehicle separation for each trial of the simulation. The distribution of breakup points provides an estimation of the range of altitudes at which a vehicle of the category analyzed could disassemble. Such a distribution will be discussed in Section 5.3.1.

5.2.1. Variation of aerodynamic properties of the vehicle

Since the algorithm keeps the ballistic coefficient of the vehicle fixed during the simulation, it is important to understand what this means in terms of variations in nominal trajectory and mostly in nominal impact point. Referring again to Figure 5.4a, it is evident that the reentry trajectory passes over an area that contains all the longitudes and a wide range of latitudes, so a change in reentry conditions could dramatically modify the impact point, moving it from water to land or even to densely inhabited regions.

Figure 5.5 shows the variation in impact point location due to the vehicle ballistic coefficient expressed through the variation of drag coefficient. Values are changed from 1.8 to 2.6 with an increment of 0.002, in order to understand the effects of even small deviations. As supposed, impact point locations are spread in longitude and latitude with respect to the base case. There is not a clear trend but it seems that there are series of values that are shifted in longitude of an amount that is proportional to the percentage of variation. In particular, there is a central series produced by values of C_D that differ from the main value of ±10%. Then, as the percentage increases, the other series shift westward for lower values of C_D and eastward for higher ones. It is possible to conclude that also regions far from the nominal ground track could be affected by the reentering object if the assumed ballistic coefficient is not so close to the actual one.

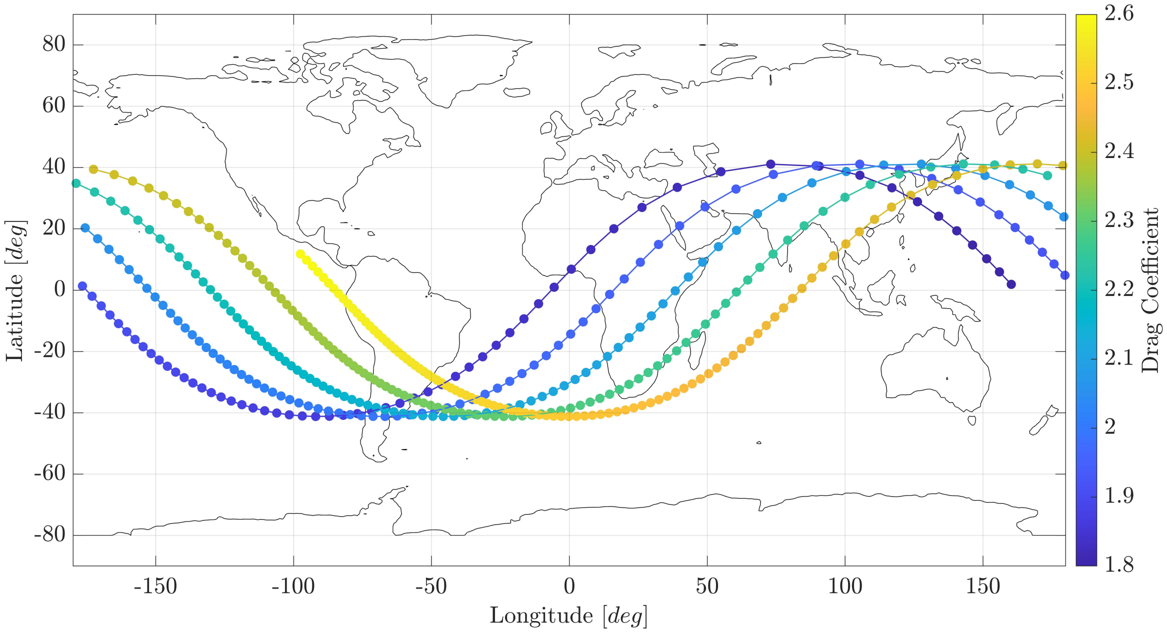

Figure 5.5: Nominal impact points locations for different drag coefficients of the vehicle

Thus, it comes out that a preliminary analysis on main vehicle aerodynamic properties is needful to understand what are the most critical impact points or ground tracks in terms of potential risk to population and surroundings. According to this, the impact points distribution is combined to the values of world population density in Figure 5.6.

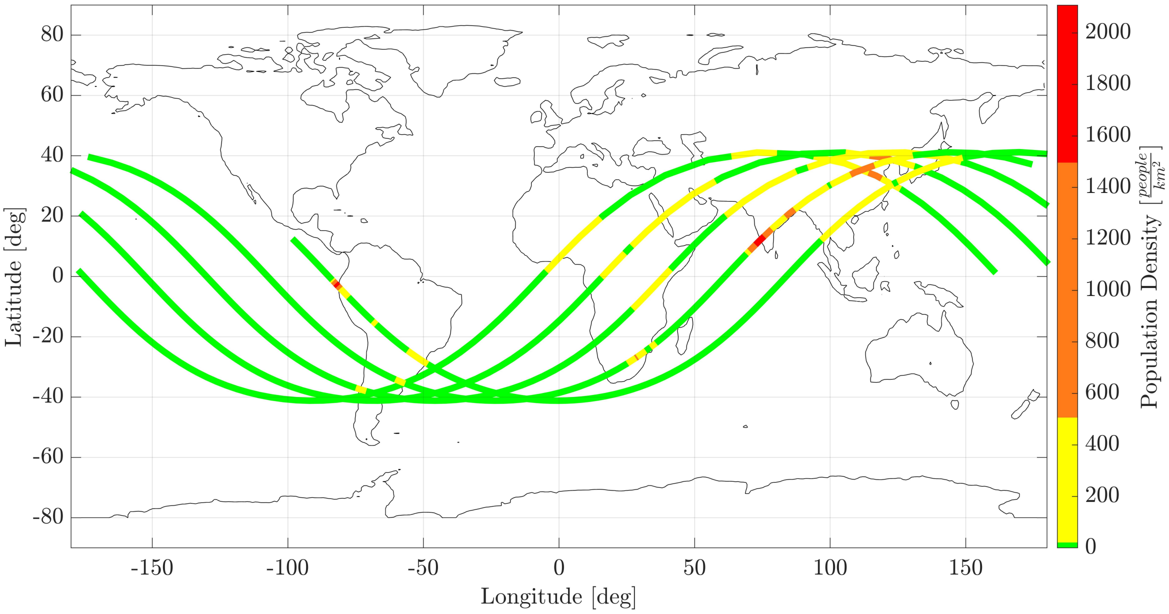

Figure 5.6: Nominal impact points locations vs. population density in the impact area

The usefulness of this graph is twofold: it can be used to exclude impact points that are clearly in ocean and it can be used to identify the critical values of ballistic coefficient for which the reentry simulation needs to be restarted. The most potentially dangerous impact points turn out to be the one located in the south of India due to the very high population density, the one located in the South America near the coastline between Peru and Ecuador due to high population density too, and the region located over China due to a moderate population density and also due to the presence of nuclear facilities. Also yellow zones and green apparently safe regions on land should be analyzed in detail because reentry path could deeply change due to other uncertain parameters, explosions at high altitude, local atmosphere conditions and winds effect.

5.3. Probabilistic distributions

The most relevant outcomes of the probabilistic breakup analysis are the breakup altitude, the final mass and the casualty area. In the following sections, the probability ranges obtained for these quantities are presented. Dealing with items involved in the reentry, the term *elements* refer to intact components that detach from the main vehicle and fall apart, instead the term *fragments* refer to debris generated from an element that undergoes fragmentation. Sometimes in the following the term *separation altitude* is used in place of breakup altitude, but they actually coincide.

5.3.1. Critical Altitudes

Two important altitudes are computed by the algorithm: separation altitude of the structure and fusion altitude of an element.

The first one is the altitude at which the material of the structure reaches the melting temperature. This is also the instant at which the components are released from the vehicle, so it is assumed as the breakup altitude. Figure 5.7 shows the distribution of separation altitude over one hundred simulated reentries. The range goes from 75 km to 115 km with the most probable values around 95 km. This is in agreement with the range of breakup altitudes that is commonly used by deterministic models. Moreover, the distribution lies under the value of 120 km that conventionally defines the beginning of the reentry event.

The second one is the altitude at which an element falling apart reaches its own material fusion temperature. Such an altitude defines the beginning of the ablation phase, that will wear out the material generating debris and terminating in the element demise.

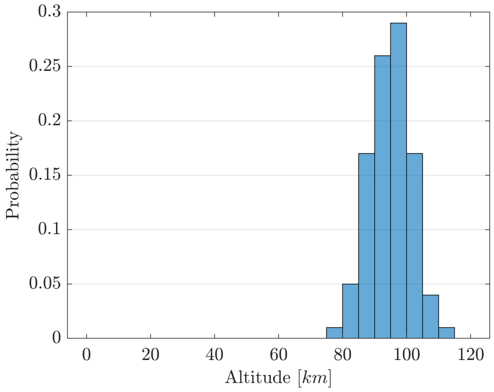

Figure 5.7: Breakup altitude distribution over 100 simulated reentries

In Figure 5.8, the distributions of fusion altitude of each one of the four simulated elements are presented. A value equal to zero means that the element impacts on ground without reaching the fusion temperature and so it will crash with the initial mass and cross section.

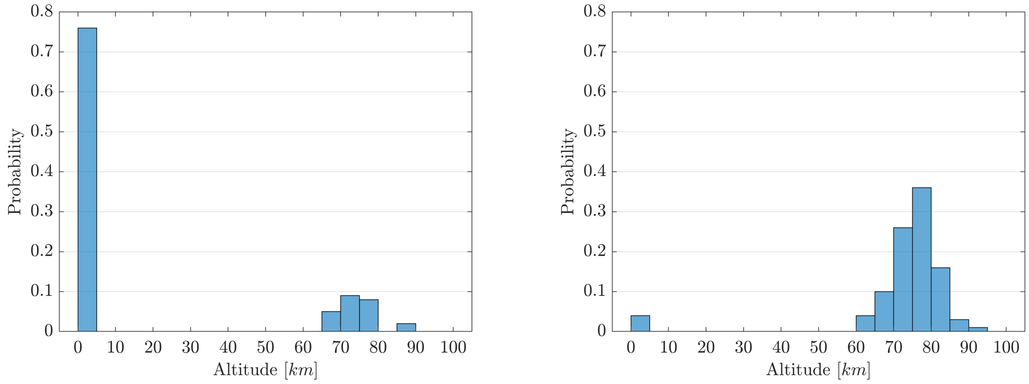

(a) Steel Tank

(b) Titanium Large Sphere

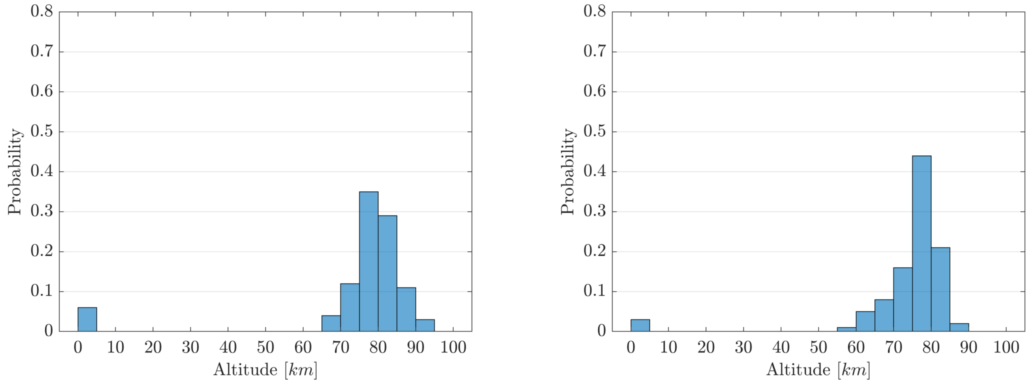

(c) Titanium Small Sphere

(d) Steel Combustion Chamber

Figure 5.8: Fusion altitude distributions over 100 simulated reentries

It is possible to observe that the main range of fusion altitudes is located between 60 and 90 km with an higher probability around the central value. However, the main tank presents a high percentage of cases in which the melting temperature is not reached. This outcome is in contrast with the one of the combustion chamber that is made of the same material and also with the ones of titanium spheres that have an higher value of melt temperature. The explanation may be given by the larger dimensions of the steel tank associated with a less regular attitude motion with respect to the one of spheres. Thus, the tank is affected on average by a lower net heat flux due to a lower heat transfer orientation factor. It seems also that, except for the elements that don't melt, there is a sort of correlation between fusion altitudes, since all the elements reach the fusion temperature in almost the same range of altitudes.

The distribution related to the guidance box is absent because the element follows almost the same distribution of the structure. In fact, it reaches the fusion temperature at high altitudes and undergoes complete ablation in all the simulated trials. For this reason, the component is not carried on further in the simulation, even if usually the guidance box contains instruments and devices needed for navigation made of different materials, such as reaction wheels, that could be released after the demise of the box undergoing their own reentry process. The analysis of internal components goes beyond the scope of the present work.

5.3.2. Final mass

The final mass of an element is the quantity used to detect the effects of ablation during the reentry. It is also the key parameter of the fragmentation module implemented in the algorithm. Figure 5.9 shows the final mass distributions for each element over the reentry simulation. The final mass distribution is in some way connected to the distribution of fusion altitude, because for sure the percentage of impacting elements that have not reached the fusion temperature constitutes a lower bound for the percentage of impacting elements with the initial mass value. The latter one could be even higher, since elements that reach the melt temperature can still not ablate due to particular sets of values of parameters.

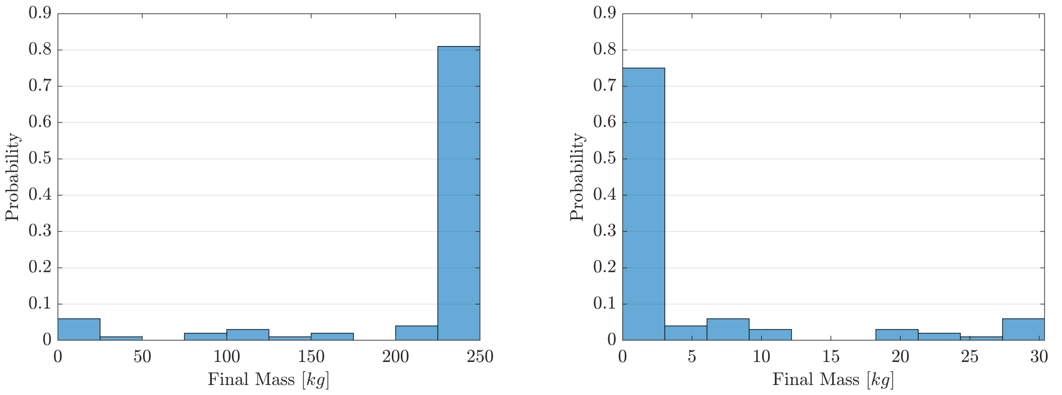

(a) Steel Tank (b) Titanium Large Sphere

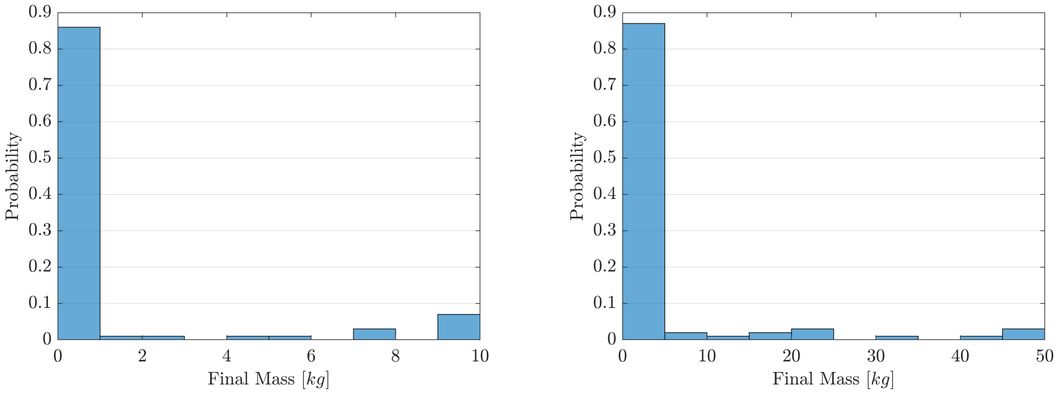

(c) Titanium Small Sphere (d) Steel Combustion Chamber

Figure 5.9: Final mass distributions over 100 simulated reentries

The most massive element is the steel propellant tank. In more that 80% of the reentries it impacts on ground still intact, being so a very critical component in the evaluation of risk. This outcome finds a confirm in the recovered debris of historical Delta II second stage reentries on land, where the main tank was found almost intact ([24], [25]). In the other cases, it can undergo different levels of ablation and even completely ablate in less than 10% of the simulated trials. Regarding the other elements, the trend appears reversed, with element demise in almost all the cases. In particular, for the combustion chamber made of steel there are low probabilities that it reaches intact the ground. The two titanium spheres have almost the same probability to impact with the initial mass, but the larger one is characterized by a lower percentage of complete ablation, that at the same time is spread over the range of partial ablation. Thus, it is likely to expect that the large titanium sphere would produce more fragments than the smaller one and that they would survive, according to the fragmentation model implemented.

5.3.3. Casualty Area

Casualty area gives a first estimate of the risk level associated to the reentry. According to the formula 2.1, for each reentry trial, the area of each impacting fragment is augmented by the projected area on ground of a standing human and added up with the others. The largest cross section area of a fragment is used in order to obtain the maximum possible result.

The total casualty area distribution over one hundred trials is shown in Figure 5.10. The spike coincides with values between 6 and 7 m^2 and the most probable range is the one between 6 and 10 m^2. Such interval represents trajectories over which ablation of elements is only a small fraction of the total mass and so they survive reentry largely intact. In fact, the upper bound ($10m^2$) coincides with the sum of casualty areas of intact elements. The portion of the curve to the left of the peak represents those simulated trajectories during which one or more elements undergo ablation. Instead, the portion of the curve to the right represents those simulated trajectories during which one or more elements fragment and generated debris survive the remaining trajectory. The total casualty area may be larger when an element fragments because there is more area projected to the ground. Therefore, fragmentation may significantly increase calculated casualty area, even to three times the most probable value.

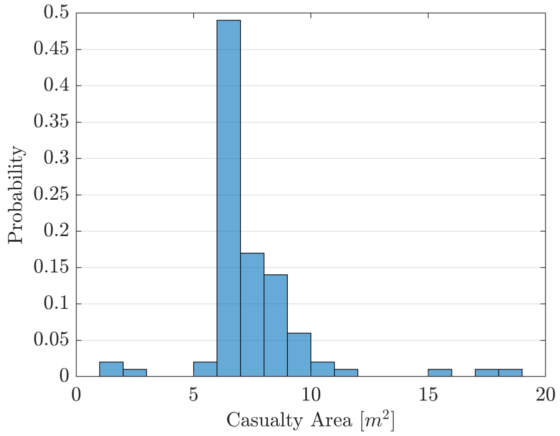

Figure 5.10: Total casualty area over 100 simulated reentries

Figure 5.11 shows the contribution of each simulated element to the total casualty area. Each distribution is computed over the total number of reentries but only the impacting fragments contributes to the casualty area. Therefore, the column corresponding to zero area is omitted and the sum of probabilities of the depicted columns is equivalent to the percentage of total impacting fragments.

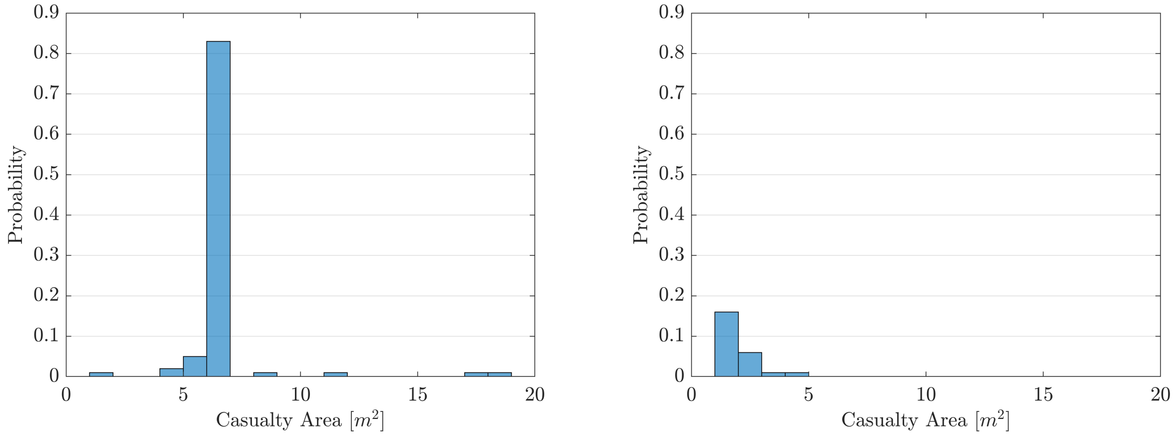

(a) Steel Tank (b) Titanium Large Sphere

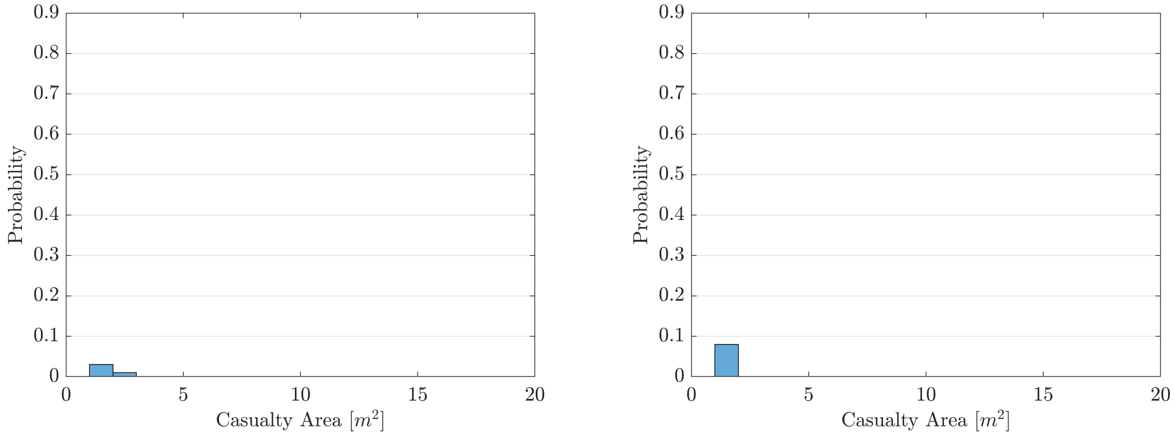

(c) Titanium Small Sphere (d) Steel Combustion Chamber

Figure 5.11: Casualty area of each element over 100 simulated reentries

The most important contributions to total casualty area are given by the steel tank due to its low average ablation percentage and by the large titanium sphere due to its fragmentation that increases the range of its casualty area, raising the values from the nominal one of $1.3m^2$ up to $5m^2$.

It is important to remark that the fragmentation module always considers the higher number of fragments that can generate from a certain ablation percentage. This is done in the attempt to obtain a considerable result from the statistical point of view despite the moderate number of trials used in the simulation. Anyhow, the total casualty area distribution obtained is similar to the one published in the reference work [2, 23].

5.3.4. Aggregation of distributions

Previous sections show the distributions obtained for each probabilistic quantity, moreover it would be interesting to understand if and how they are related one each others. Thus, the above probability distributions are combined through an aggregation process. Ranges are divided into bins and probabilities of trials that have the values defined by a certain bin are summed. Such a procedure can be useful to identify correlations or specific trends among quantities. Figure 5.12 contains the combined distributions of separation altitude and fusion altitude for each one of the simulated elements.

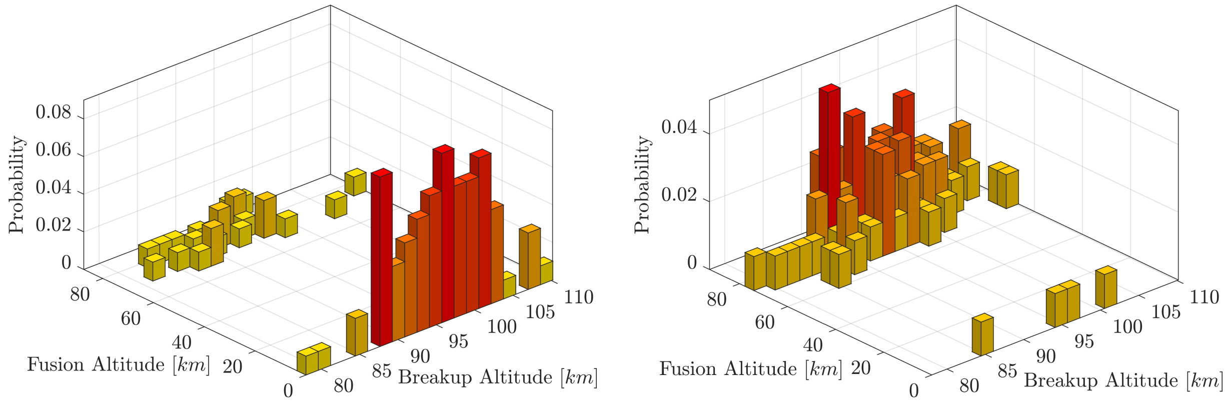

(a) Steel Tank (b) Titanium Large Sphere

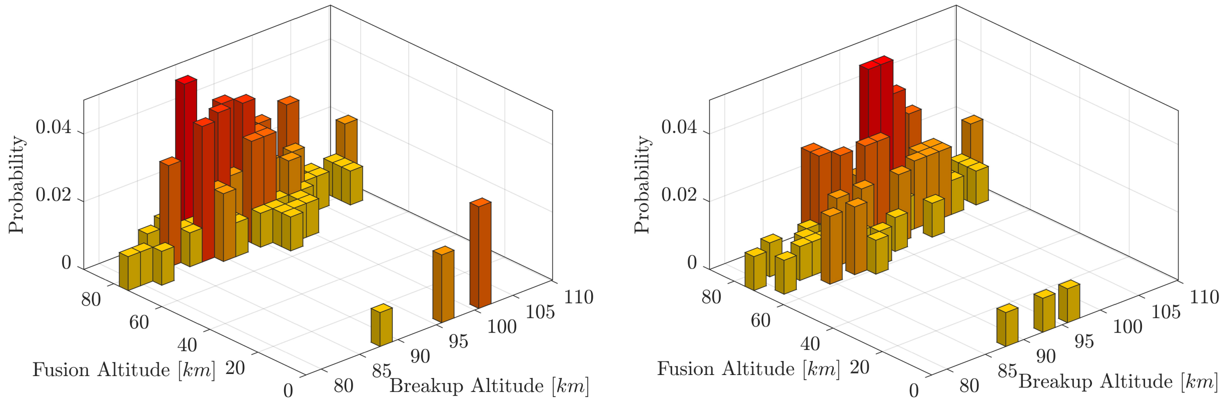

(c) Titanium Small Sphere (d) Steel Combustion Chamber

Figure 5.12: Probability distributions of fusion altitude vs. breakup altitude

There is a common feature in the fact that the fusion altitudes are mostly confined in the range between 60 and 90 km and the remaining are located in the stripe of bins equal to zero. In addition, the most probable values are confined among the central values of the range of breakup altitudes. As already seen, it is more likely that the steel tank does not reach the fusion temperature, while the other components tend to melt at high altitudes. The aggregation is coherent with the single distributions, since for example in Figure 5.12a the sum of all the bar corresponding to zero fusion altitude equals the value in Figure 5.8a.

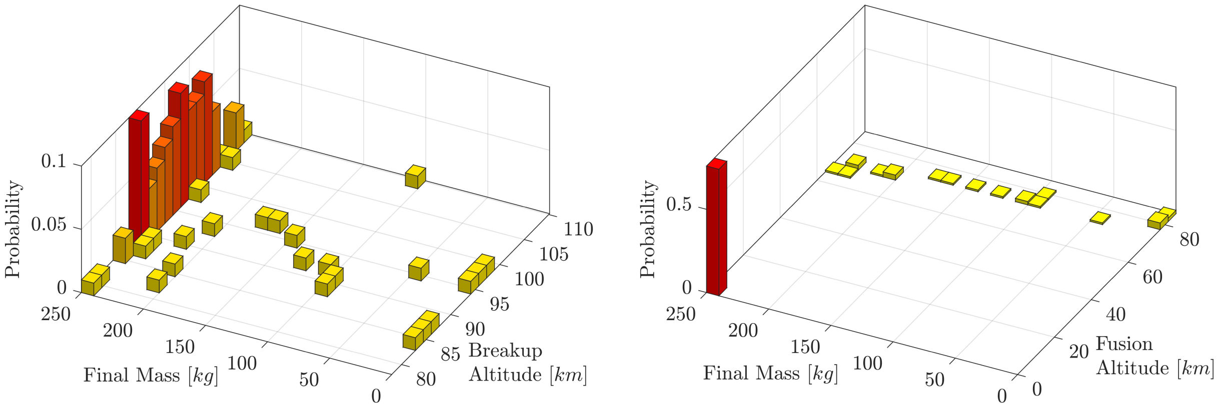

(a) Final mass vs. Breakup altitude

(b) Final mass vs. Fusion altitude

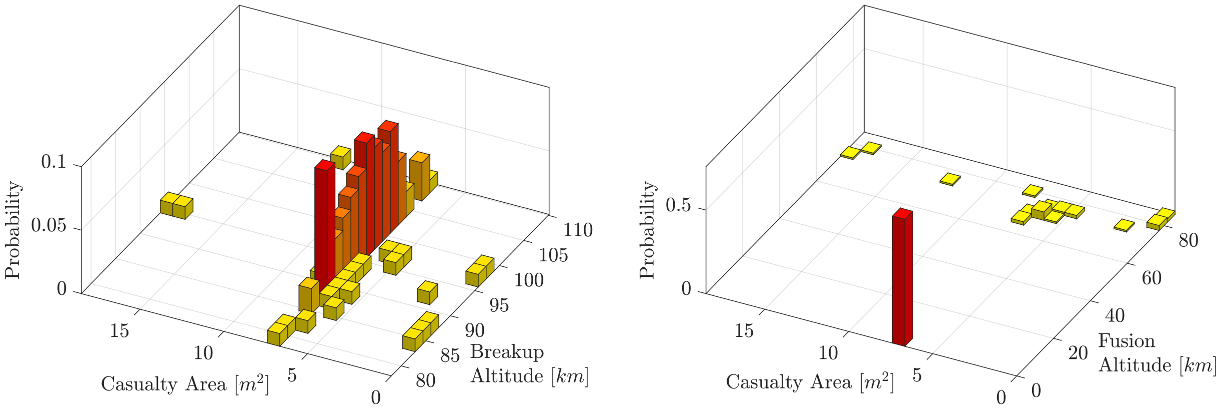

(c) Casualty area vs. Breakup altitude

(d) Casualty area vs. Fusion altitude

Figure 5.13: Critical altitudes vs. final mass and casualty area (Steel Tank)

Figure 5.13 shows the connections of peculiar altitudes with both final mass and casualty area for the steel propellant tank, cause it has the most relevant contribution in the reentry results. The graphs with the fusion altitude confirm the fact that in most of the trials the element impacts with the original mass. The remaining part is related to elements that reach the melt temperature in the altitude range between 60 and 90 km and are affected by the ablation phenomenon. There are few trials in which the ablation percentage is zero and so the element reaches ground intact, but most of the trials present a significant amount of ablated mass and so elements are prone to fragment. The effects of fragmentation can be seen in Figure 5.13d where the most probable value of casualty area divides the field in two regions in which the area increases or decreases. Such regions are made by the fragments of the elements that reach the fusion temperature during reentry.

Figures 5.13a and 5.13c confirm the considerations done above on separation altitudes, as the most of the trials result in final masses equal to the initial value whatever is the separation altitude and the remaining part corresponding to elements that experience ablation.

The consequences of fragmentation on casualty area are detailed in Figure 5.14. The algorithm uses the value of final mass of the element to compute the number of possible fragments and then propagate them to obtain their final casualty area. Figure 5.14a shows that the number of fragments becomes higher than one under a certain value of element final mass. Actually, the bin corresponding to 9 fragments is generated by a low value of final mass, while the bin of zero fragments corresponds exactly to zero final mass. This is related to the assumption that an element that undergoes great ablation of its mass can no longer remain intact and breaks into multiple fragments. Figure 5.14b instead confirms the fact that values of casualty area lower than the most probable one are given by elements that ablate without generating fragments. Instead, the region with higher values of casualty area corresponds to number of fragments higher than two. Therefore, fragmentation could increase a lot the value of casualty area.

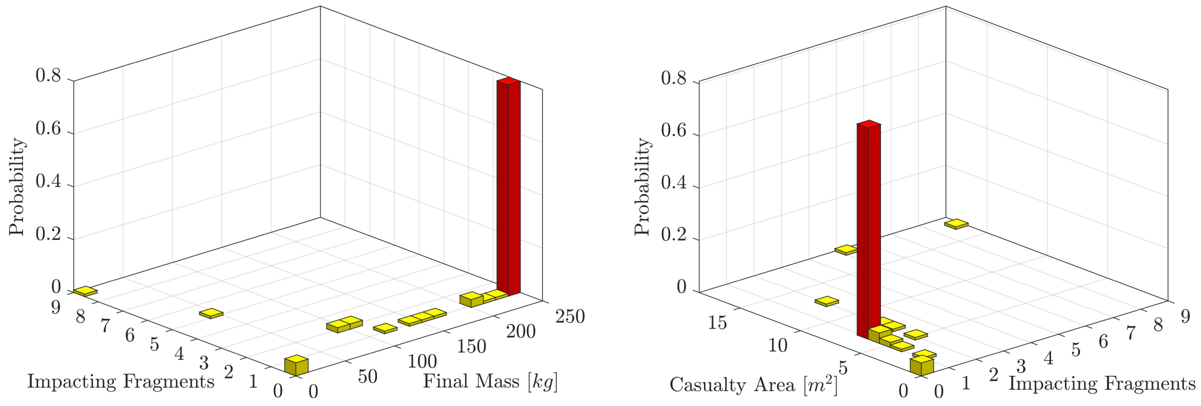

(a) Number of fragments vs. Final mass (b) Casualty area vs. Number of fragments

Figure 5.14: Final mass vs. number of fragments vs. casualty area (Steel Tank)

Finally, Figure 5.15 combines the distributions of breakup altitude and total casualty area. The most probable region is the one between 5 and 10 m^2 in casualty area with corresponding altitudes from 85 to 105 km. However, the same range of altitudes contains also the highest and the lowest values of casualty area obtained. According to this, there is no apparent correlation between separation altitude of a vehicle and total casualty area of fragments impacting ground. Effectively, there are many other events, phenomena and parameters that stand in the way from breakup to ground and affect the final value of casualty area. Anyway, a most probable range of values is identified and its magnitudes are high enough to justify a further risk analysis.

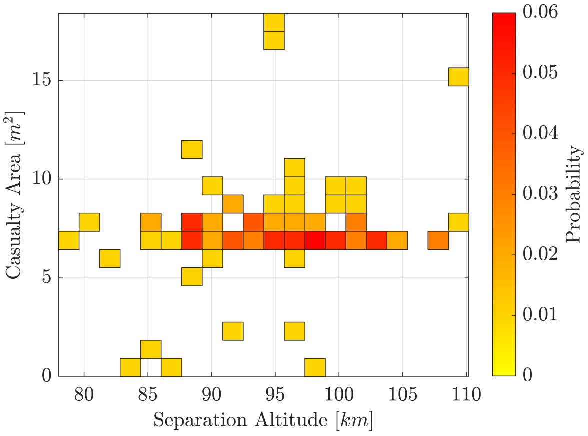

Figure 5.15: Total casualty area vs. breakup altitude

5.4. Footprint dispersion

After casualty area evaluation, the second step in estimating the risk level associated to the reentry is the footprint determination. Due to the high uncertainty involved in the reentry process, the nominal impact point gives only a coarse information about the geographical area that could be affected by impacting debris. In fact, the footprint is generally an elongated trail that could be hundred of kilometers long and tens of kilometers wide. The footprint dispersion extends in downrange and crossrange directions. The former is related to the different trajectories of debris dominated by variations in breakup altitudes, ballistic coefficient and atmospheric conditions. The latter is caused by lateral actions, such as winds effects or aerodynamic loads dependant on the attitude of the falling object. The present work considers objects as point masses from the aerodynamic point of view, so only variations of the footprint in downrange direction are expected.

5.4.1. Footprint of the vehicle

Figure 5.16 shows the probabilistic footprint of the vehicle over one hundred simulated reentries. The impacting fragments of each of the four components are put together in order to compare their relative footprint distributions. In addition, the information about the casualty area associated to each fragment is depicted with the dimension of each point. A bigger circle means higher area projected on ground.

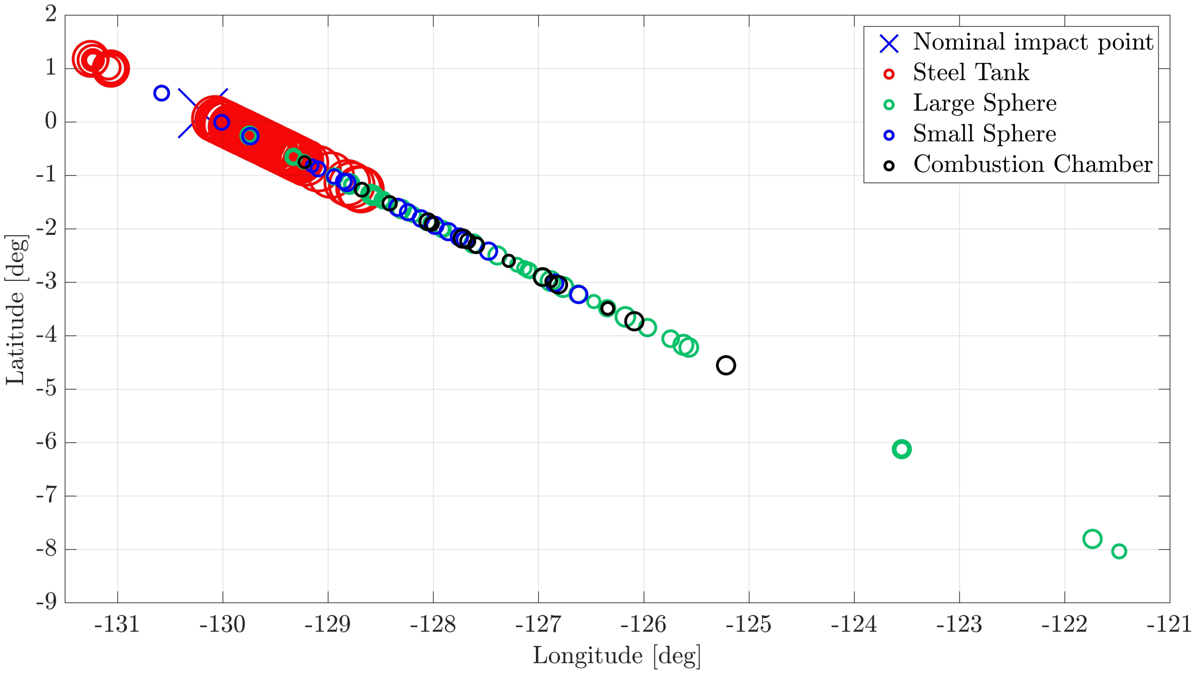

Figure 5.16: Probabilistic footprint over 100 simulated reentries (base case $C_D = 2.2$)

The impact points of debris coming from the steel tank are located near the nominal impact point with an higher concentration immediately after it. Such a result is found also for the other components with an increasing dispersion in downrange direction passing from the small sphere to the combustion chamber and then the large sphere. Some debris fall also before the nominal impact point along the ground track. The different length of distributions of each element could be caused by different breakup altitudes, different ballistic coefficients of fragments and also to different atmospheric conditions encountered during the specific trajectory of each fragment. All these effects can significantly change the impact point and so they will be investigated in the next section.

5.4.2. Footprint of each element

With the purpose of getting insight about the location of impact points, in this section the footprint dispersion of each element is analysed. Figure 5.17 shows the impact points over all trials for each element with dimensions related to casualty area and colors related to separation altitude.

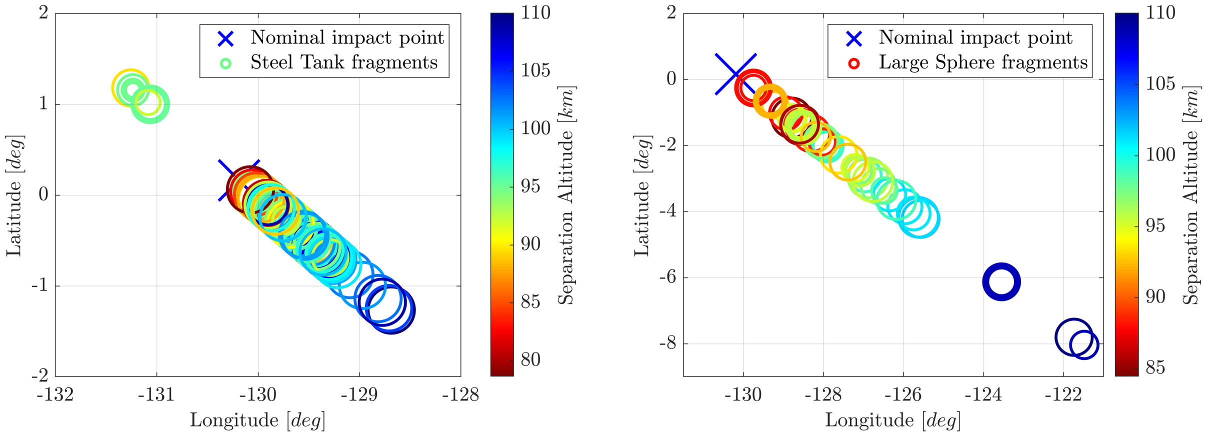

(a) Steel Tank

(b) Titanium Large Sphere

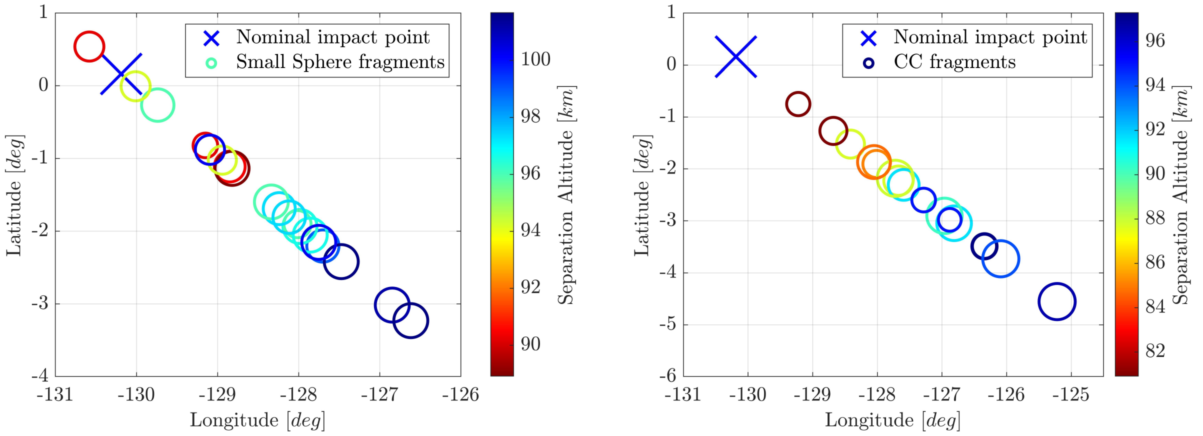

(c) Titanium Small Sphere

(d) Steel Combustion Chamber

Figure 5.17: Footprint of each element (dimensions with A_{CAS}, colors with h_{SEP})

The breakup altitude has no evident effect on the casualty area of impact points since there are circles of same size evenly distributed along the footprint and also circles with different size intersects one each other. Instead, it is possible to identify a sort of division of the footprint in sectors according to the range of separation altitudes. Lower altitudes cause that impact points are closer to the nominal impact point, while increasing altitudes cause an higher offset. This effect is more evident in Figures 5.17b,c,d, while in the graph of the steel tank there is a dissimilarity in the points before the nominal point.

It is important to mention that the dependency on the fusion altitude is not included because, even if it is the altitude at which fragments are generated, it does not directly affect the impact point. In fact, the final point is strictly related to the trajectory of each fragment in term of initial position and ballistic coefficient. The initial position depends on the trajectory of the parent element and so indirectly on the breakup altitude. The effect of the ballistic coefficient is investigated in Figure 5.18, associating to impact points the value of drag coefficient of the related fragment.

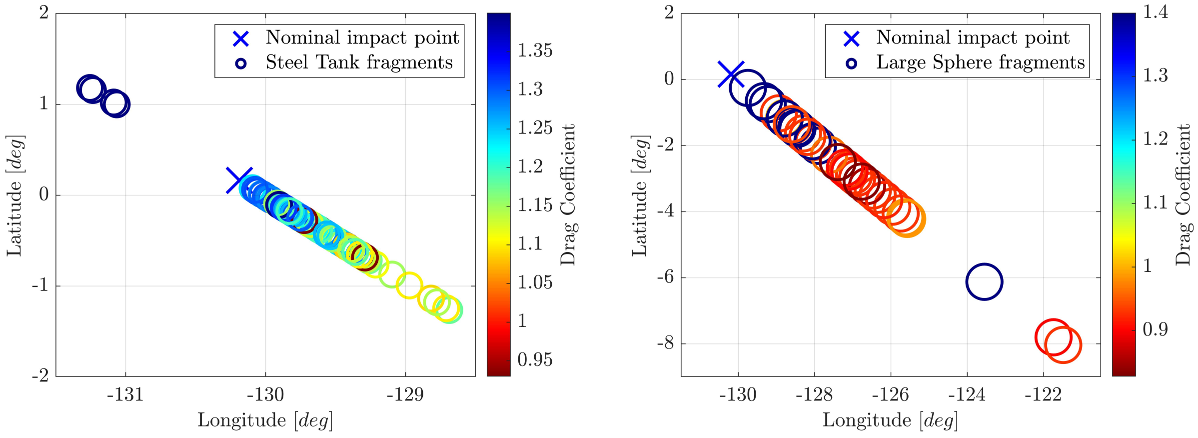

(a) Steel Tank

(b) Titanium Large Sphere

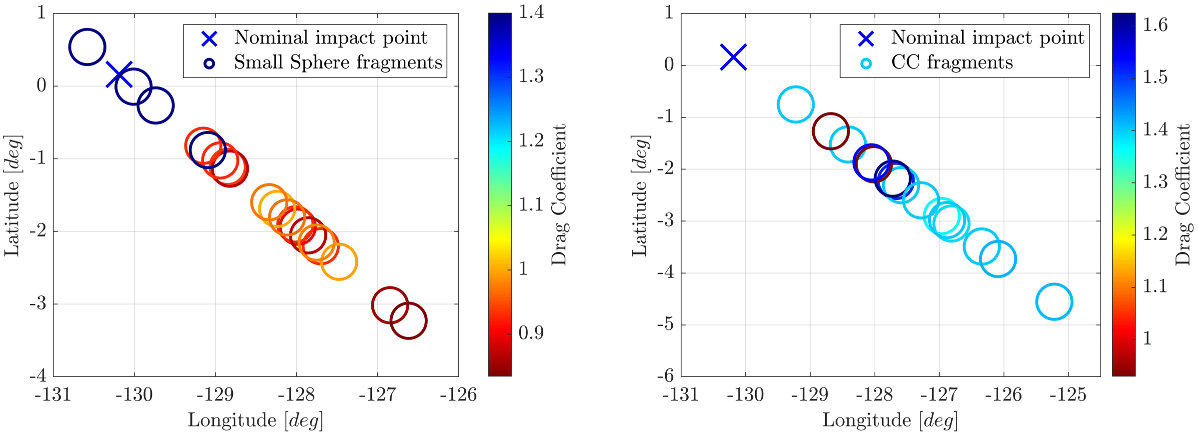

(c) Titanium Small Sphere

(d) Steel Combustion Chamber

Figure 5.18: Footprint of each element (colors with C_D of each fragment)

It comes out that fragments with higher drag coefficient impact before the others, but the distinction is not so clear. For example, in Figure 5.18b there is a "blue" circle very far from the other of the same color and in Figure 5.18d there are points with lower drag coefficients before points with higher values. According to this, additional analyses on a further dependency were made adding one by one the data of separation altitude, fusion altitude, initial area of the fragment and casualty area, but no correlation was found. Probably, the third effect in footprint dispersion is linked to the initial position of the fragment that determines the atmospheric conditions that the fragment itself will face along its trajectory.

5.5. Casualty Risk

Estimation of casualty risk is the ultimate result of a reentry analysis and it is an index of how much the reentry is hazardous for population and properties in the affected regions. Since the footprint of the base case is totally on the ocean, well away from populated land, the algorithm is run anew for the potentially risky cases highlighted in Section 5.2.1. Those reentry events are associated to values of drag coefficient that are well distributed over the range of variability, thus it will be possible to compare the shape of the footprint and the casualty risk between nominal trajectories that belong from the middle and from the edges of the range. Safety standards give limits on casualty expectancy and so this is the quantity taken as reference in this section. Reentry events that could not accomplish the limit of one casualty over ten-thousands are not acceptable and further measures to reduce the risk should be adopted. Casualty expectancy is given by the product of casualty area, population density and probability of the reentry event. Casualty area depends on size of impacting fragments, population density is directly linked to the location of the impact, while the probability needs a separate discussion.

5.5.1. Population Density

Population density is obtained from the Gridded Population of the World, Version 4 (GPWv4): Population Density, Revision 11 [26]. It consists of estimates of human population density (number of persons per square kilometer) based on counts consistent with national censuses and population registers, for the years 2000, 2005, 2010, 2015, and 2020. A proportional allocation gridding algorithm, utilizing approximately 13.5 million national and sub-national administrative units, was used to assign population counts to 30 arc-second grid cells. To enable faster global processing, and in support of research communities, the 30 arc-second count data were aggregated to 2.5 arc-minute, 15 arc-minute, 30 arc-minute and 1 degree resolutions to produce density rasters at these resolutions. In the present work, the population density map of the year 2020 at 1 degree resolution is used. It is important to report that the map is not always consistent with the geographical borders on lands, as happen exactly in the south corner of India where in the western part comes out a strange shape of the coastline. The same behaviour is found also in density maps with finer grids, but for the level of approximation of this work, it is anyway considered acceptable.

5.5.2. Impact probability

Generally speaking, the impact probability is the probability of a reentry event and the total casualty expectancy is the summation over all the reentry event weighted by the probability of each. However, each reentry event produces different types of fragments that impact in many different locations. Since both the fragmentation and the footprint dispersion are stochastic processes, the present work associates the probability of occurrence to the single fragment and not to the overall reentry event. Doing so, the total casualty expectancy of each reentry trial is computed as the sum of the casualty expectancy of each impacting fragment. The impact probability of each fragment is translated into the probability of existence of a fragment with a certain area, that has been generated at a certain altitude from a parent element that has separated at a certain breakup altitude. In practice, the breakup altitude range is divided in bins from zero to the maximum value and the probability of each bin is computed over the values of all the reentry trials. The same procedure is applied to the fragmentation altitudes, but repeated for every bin of breakup altitude, in order to relate the fusion altitude to the corresponding separation altitude. Then, the range of casualty area is divided into bins too and the probability of each bin combined with the corresponding fragmentation altitude is computed. Finally, the probabilities of the area bins combined with the fusion altitude bins are again combined with the probabilities of fusion altitude bins combined with separation altitude bins to obtain the desired probability of each generated fragment according to its previous steps. Such a method of computing impact probability of each fragment is dependant on the number of available data and so on the number of simulated trials. Therefore, increasing the number of simulated reentries would produce a more detailed database for a more refined probability calculation.

5.5.3. Casualty Expectancy: case 1

Here are reported the results of risk estimation for the case with $C_D = 2.248$, that corresponds to the nominal impact point in the south of India. Figure 5.19 shows the ground track from the last apogee to impact and the footprint dispersion of all impacting fragments. Only the value of drag coefficient is changed with respect to the base case, while the set of sampled parameters is exactly the same. The point at which happens the crossing of 120 km altitude is almost the same as the base case, while the impact point location deeply changes even if the variation in drag coefficient is only of 2%.

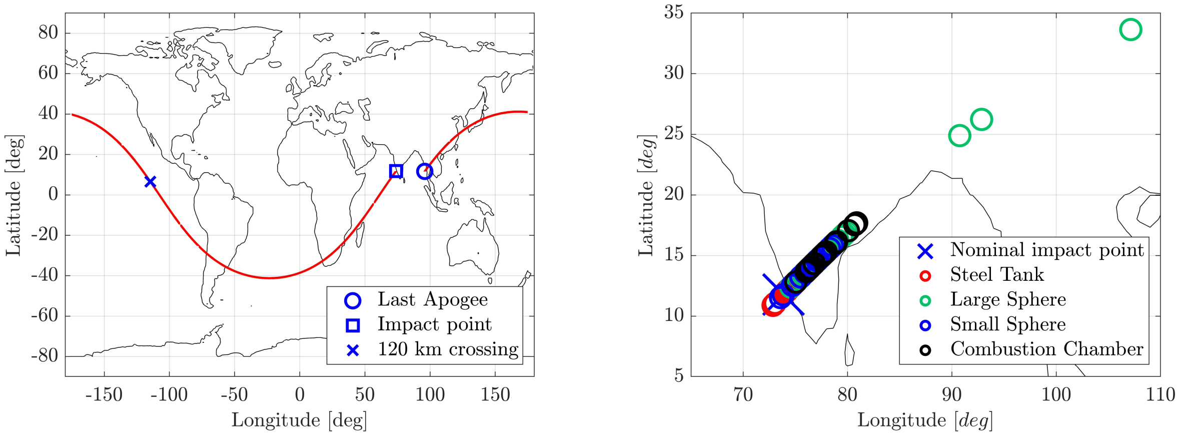

(a) Ground track (b) Footprint distribution

Figure 5.19: Trajectory from last apogee to ground (case with $C_D = 2.248$)

The footprint dispersion is comparable with the one of the base case, as the debris coming from the steel tank are located near the nominal impact point and the debris of the other components have an increasing dispersion in downrange direction passing from the small sphere to the combustion chamber and then the large sphere. This last component produces fragments that impact very far from the nominal point in some cases. Those fragments come from reentries in which the breakup happens at altitudes over 120 km and this translates into a longer path before impacting on ground. Fragments belonging from other elements are not present at the same locations because they demise.

Figure 5.20 shows the resulting casualty expectancy represented in terms of probabilities for each range and computed values for each point of the gridded map of the region affected by the footprint dispersion. It comes out that the highest risk is expected near the nominal impact point. This could be given by the fact that the reentry case was selected because the nominal impact point is over a very populated zone, but also by the fact that the bulk of the impacting fragments is nested around the nominal point too.

It is important to remark that the two graph of Figure 5.20 are conceptually different. The histogram refers to the total casualty expectancy of each simulated reentry obtained summing up the E_C of each element. The map, instead, refers to total casualty expectancy in each area defined by the grid (1 deg in longitude x 1 deg in latitude). Moreover, in the histogram the sum of probabilities is not 1 because there are trials in which the casualty expectancy is zero and they are discarded in making the graph.

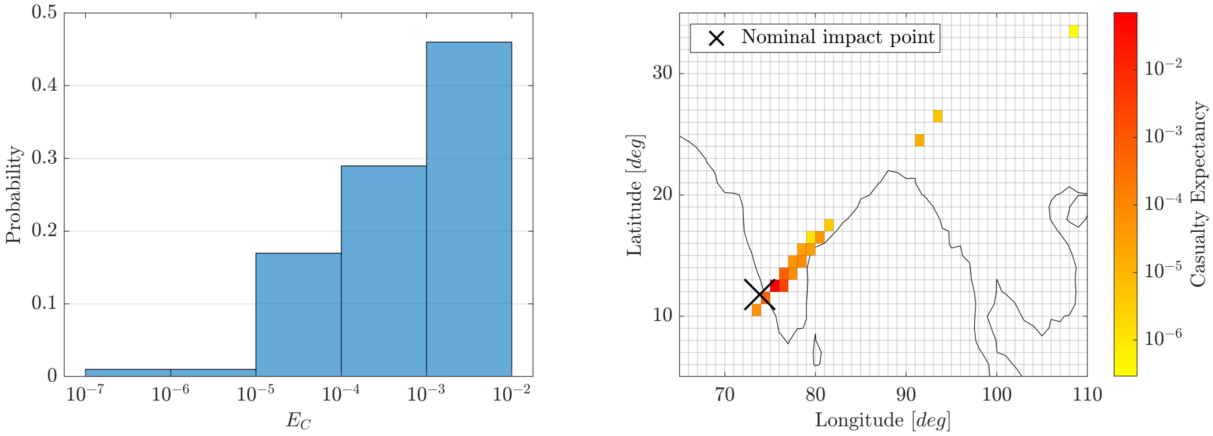

(a) Total histogram (b) Gridded map

Figure 5.20: Casualty expectancy over 100 simulated reentries (case with $C_D = 2.248$)

5.5.4. Casualty Expectancy: case 2

Here are reported the results of risk estimation for the case with $C_D = 1.814$, that corresponds to the nominal impact point in the east of China. Figure 5.21 shows the ground track from the last apogee to impact and the footprint dispersion of all the impacting fragments. Only the value of drag coefficient is changed with respect to the base case, while the set of sampled parameters is exactly the same.

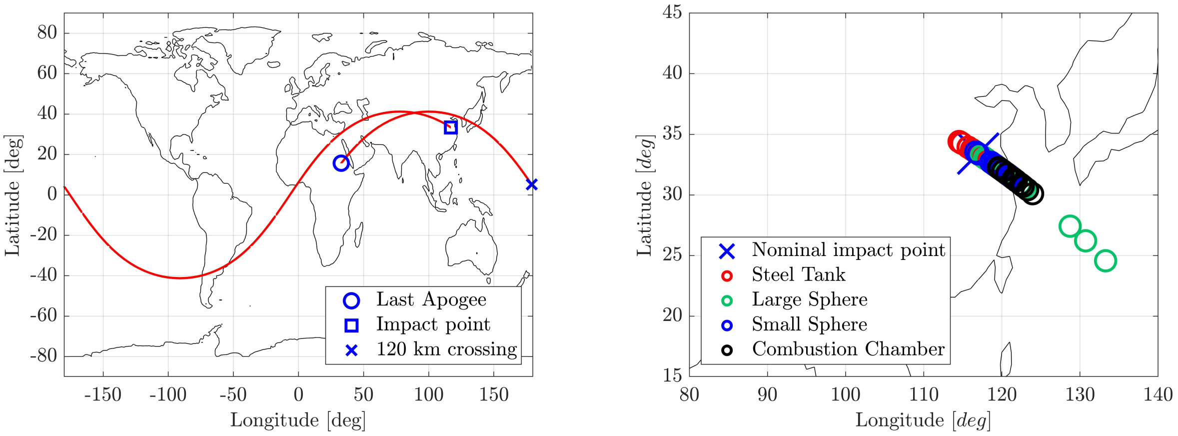

(a) Ground track (b) Footprint distribution

Figure 5.21: Trajectory from last apogee to ground (case with $C_D = 1.814$)

The point at which the crossing of 120 km altitude happens is far in longitude from the one of the base case, but it is almost at the same latitude. Moreover, it is quite near to the zone of impact. The footprint dispersion is again comparable with the one of the base case, as the debris coming from the steel tank are located near the nominal impact point and the debris of the other components have an increasing dispersion in downrange direction passing from the small sphere to the combustion chamber and then the large sphere. Some fragments impact very far after the nominal point. Those fragments come from reentries in which the breakup happens at altitudes over 120 km and this translates into a longer path before impacting on ground. Fragments from other elements are not present at the same locations because they demise or fall along a different trajectories due to differences in drag coefficient.

Figure 5.22 shows the resulting casualty expectancy represented in terms of probabilities for each range and computed values for each point of the gridded map of the region affected by the footprint dispersion. It comes out again that the highest risk is expected near the nominal impact point. This could be given by the fact that the reentry case was selected because the nominal impact point is over a very populated zone, but also by the fact that the bulk of the impacting fragments is nested around the nominal point too. The fragments far from the nominal point actually do not contribute at all to the casualty expectancy because they fall on water in this case.

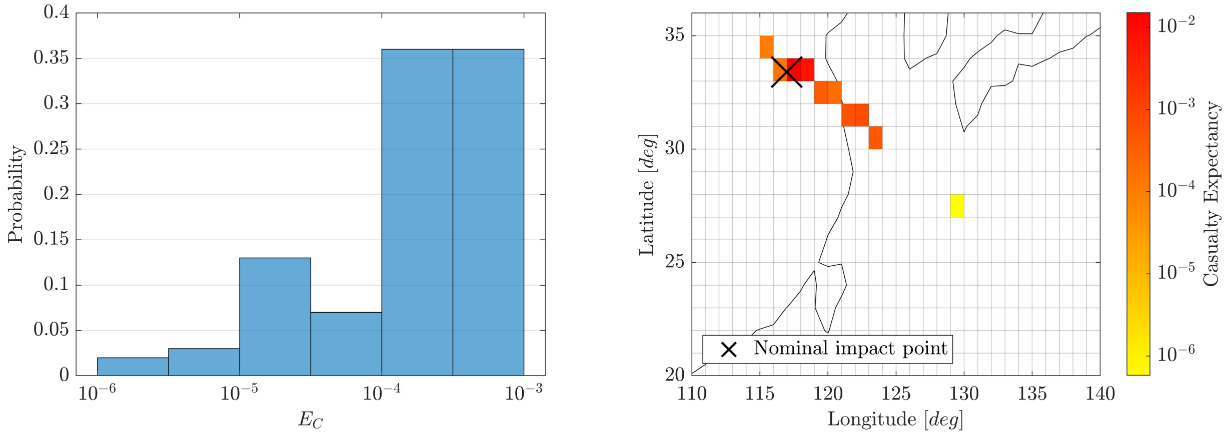

(a) Total histogram (b) Gridded map

Figure 5.22: Casualty expectancy over 100 simulated reentries (case with $C_D = 1.814$)

5.5.5. Casualty Expectancy: case 3

Here are reported the results of risk estimation for the case with $C_D = 2.584$, that corresponds to the nominal impact point over Peru and Ecuador. This case completes the range of variability of the drag coefficient of the vehicle, since the first case is near the central point, while the second one is near the lower bound and this latter is near the upper bound of the analyzed distribution. Figure 5.23 shows the groundtrack from the last apogee to impact and the footprint dispersion of all the impacting fragments. Only the value of drag coefficient is changed with respect to the base case, while the set of sampled parameters is exactly the same. The point at which happens the crossing of 120 km altitude is quite near in longitude from the one of the base case and it is almost at the same latitude. Moreover, it is quite near to the zone of impact.

This latter consideration finds correspondence also in the other cases and it would be an interesting topic to further investigate, because if there is a similarity between the coordinates of the point at which the spacecraft crosses the altitude of 120 km and the coordinates of the impact point, then they can be related and probabilistic distribution can be built with only the former as input and the latter as output, avoiding to run some parts of the algorithm.

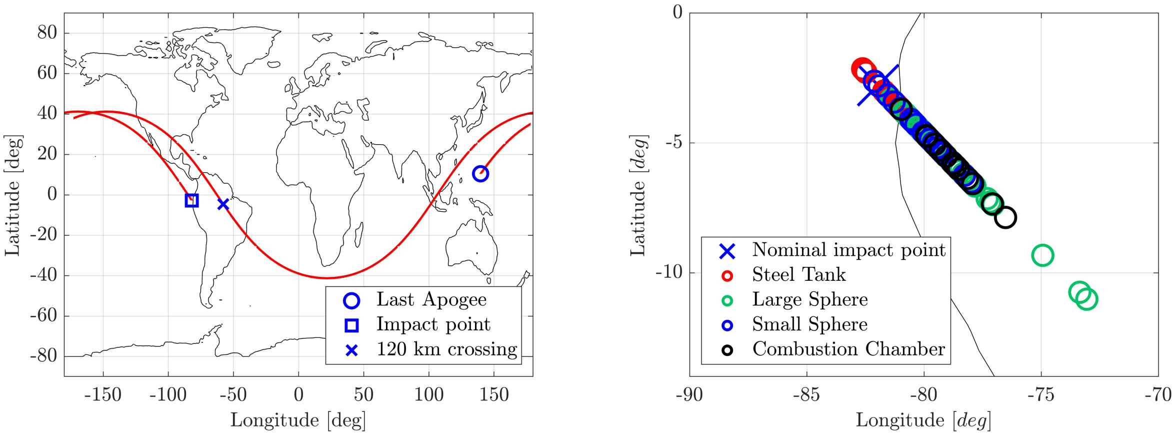

(a) Ground track (b) Footprint distribution

Figure 5.23: Trajectory from last apogee to ground (case with $C_D = 2.584$)

The footprint dispersion is again comparable with the one of the base case, as the debris coming from the steel tank are located near the nominal impact point and the debris of the other components have an increasing dispersion in downrange direction passing from the small sphere to the combustion chamber and then the large sphere. Some fragments impact far after the nominal point but the dispersion is not so elongated as in previous cases.

Figure 5.24 shows the resulting casualty expectancy represented in terms of probabilities for each range and computed values for each point of the gridded map of the region affected by the footprint dispersion. It comes out again that the highest risk is expected near the nominal impact point. This could be given by the fact that the reentry case was selected because the nominal impact point is over a very populated zone, but also by the fact that the bulk of the impacting fragments is nested around the nominal point too.

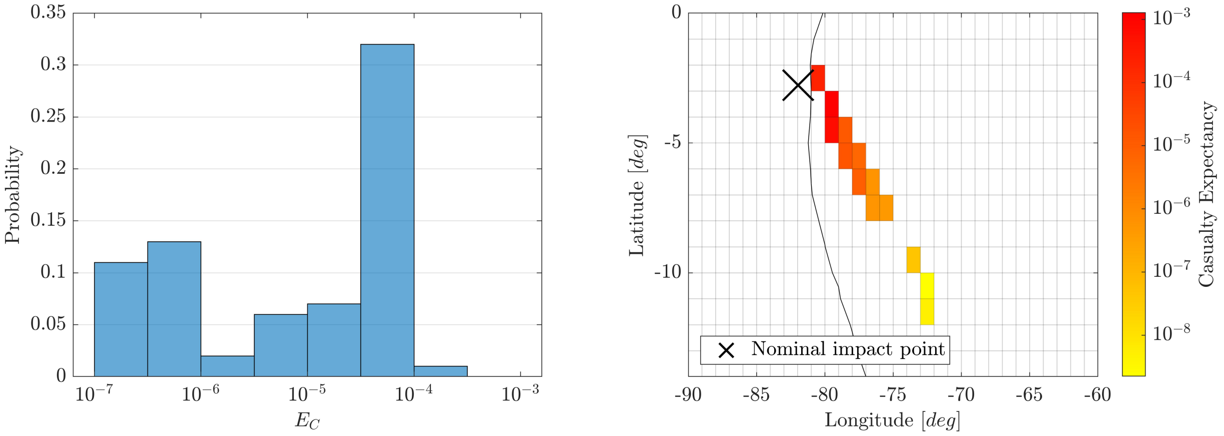

(a) Total histogram (b) Gridded map

Figure 5.24: Casualty expectancy over 100 simulated reentries (case with $C_D = 2.584$)

5.6. Sensitivity Analysis

In order to understand the sensitivity of crucial variables and outcomes of the simulation to the parameters, a detailed analysis has been performed. The sensitivity analysis includes only parameters that have substantial effects on the main elements, which are the structure, the steel propellant tank and the titanium large sphere. The tank is considered because it gives the main contribution to casualty area, while the large sphere is considered for its elongated footprint dispersion. The parameters are selected after a procedure of aggregation as in Section 5.3.4. Figures 5.25, 5.26, 5.27 report the most significant combined distributions for structure, tank and large sphere, respectively.

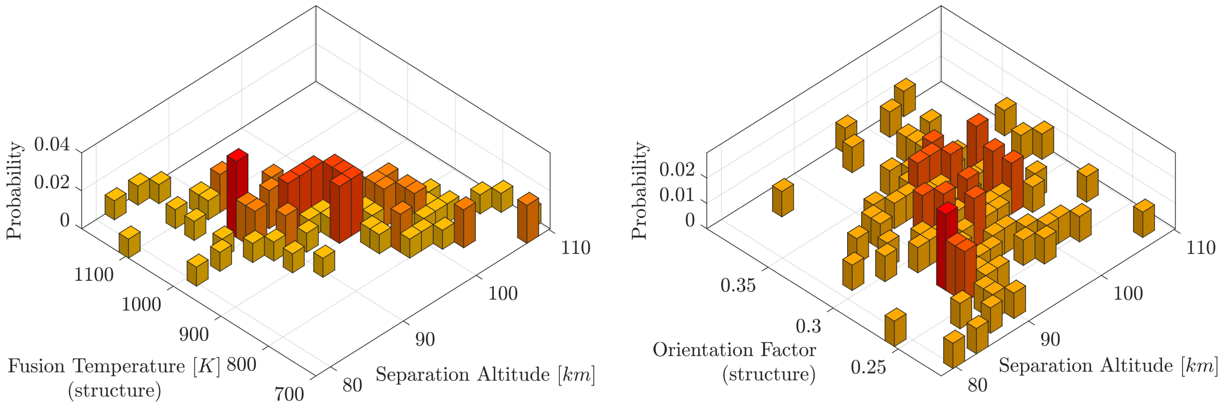

(a) Fusion temperature

(b) Orientation Factor

Figure 5.25: Correlation of breakup altitude and parameters of the structure

For the structure, it comes out that there is an almost linear relation between fusion temperature and separation altitude. Thus, variation in melt temperature of the structure directly affects the breakup altitude of the vehicle. Also the dependence on heat transfer orientation factor is remarkable.

Regarding the steel tank, high values of fusion temperature bring to impacting elements with initial mass, while low values allow fusion and ablation. Moreover, even if not reported, material emissivity and orientation factor condition the final mass distribution as high values of ε and low values of OF reduce the heat absorption and so the element remains intact.

Regarding the titanium large sphere, high values of emissivity and melt temperature inhibit the fusion process and at the same cause impacts of intact elements.

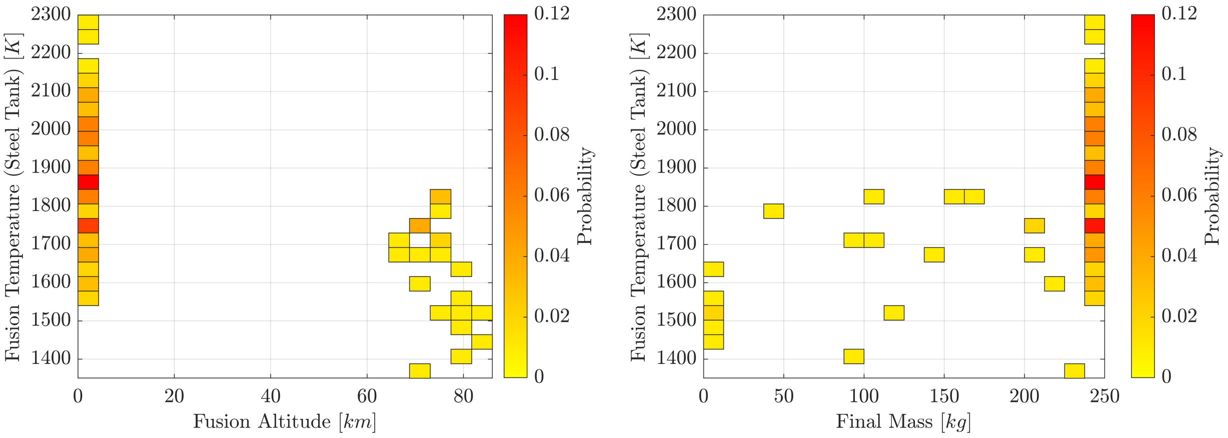

(a) Fusion altitude (b) Final mass

Figure 5.26: Correlation of variables and parameters for the Steel Tank

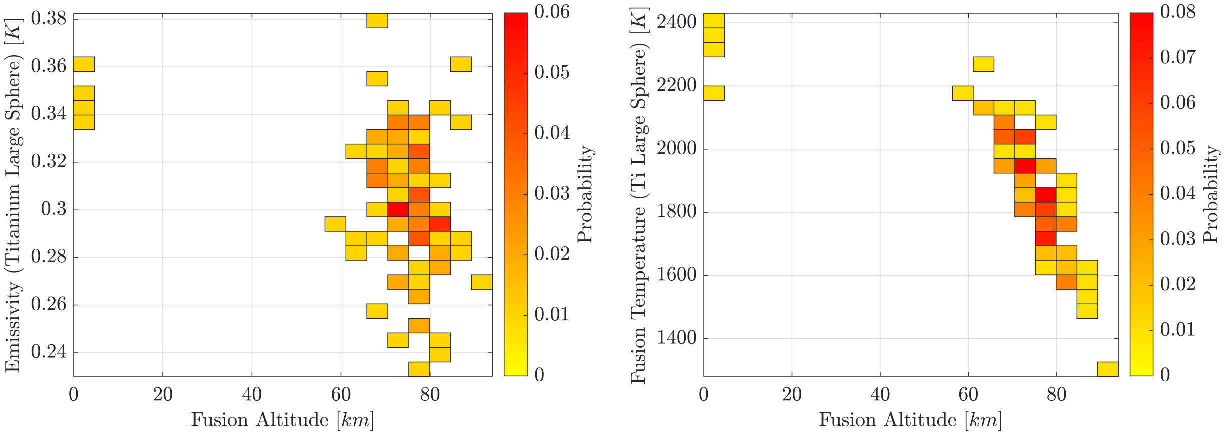

(a) Emissivity vs Fusion altitude (b) Fusion temperature vs. Fusion altitude

Figure 5.27: Correlation of variables and parameters for the Titanium Large Sphere

According to previous graphs the sensitivity analysis is planned on fusion temperature and orientation factor of the structure, while for the two elements on melt temperature, emissivity and orientation factor. Finally, also the sensitivity at the variation of drag coefficient of each element is investigated, consistently with the analysis done for the main vehicle. In practice, the distributions of parameters are modified to account for lower and higher uncertainty. By doing so, the standard deviation of normal and uniform distributions is either halved of doubled; however in triangular distributions, a variation of 20% around both the lower and upper bounds is applied.

In the following, the results obtained for each chosen parameter on the three considered elements are shown. Every modified distribution is compared with the one from the base case.

5.6.1. Varying melt temperature of the structure

In order to analyze the sensitivity to melt temperature of the structure, the sampling procedure is applied again to build two new normal distributions with half and double standard deviation with respect to the base case. The new sets of temperature are compared with the base one in Figure 5.28. The objective is to investigate what happens for reduced and augmented uncertainty. The distribution in Figure 5.28b is wider that the base one and it is useful for include outliers that could represent particular alloys or an unknown material but similar to the assumed one.

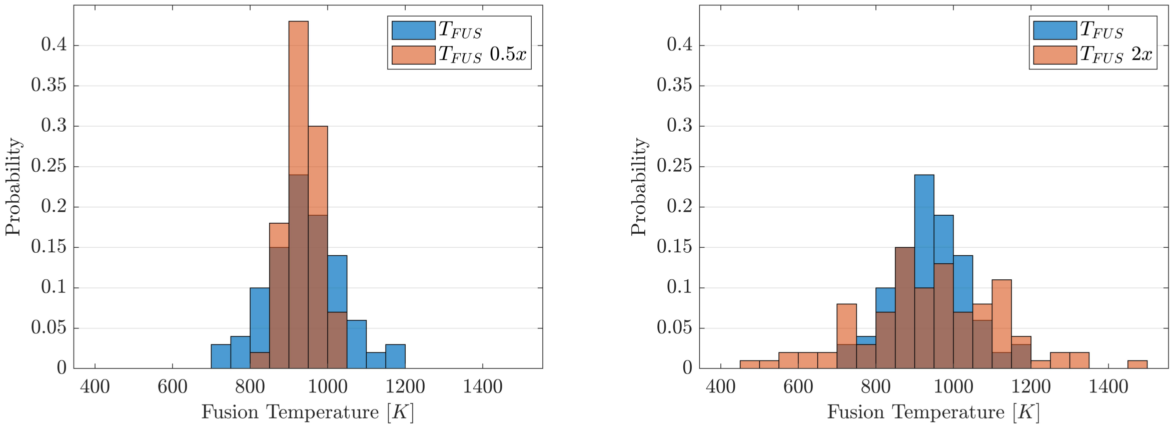

(a) Half standard deviation

(b) Twice standard deviation

Figure 5.28: Comparison of sampled distributions of fusion temperature (structure)

According to Figure 5.25a, it is expected that, decreasing the range of fusion temperatures of the structure, the range of breakup altitudes will decrease too and vice versa. As shown in Figure 5.29, this actually happens. In particular, for reduced uncertainty the probability of central altitudes increases, while for the augmented uncertainty case the probability spreads over a wider range especially on the right side of the distribution and breakup could happen even at very high altitudes. An higher altitude of separation of the structure could deeply modify the reentry path and the thermal effects on components. Therefore, also the distributions of casualty area and footprint dispersion are explored.

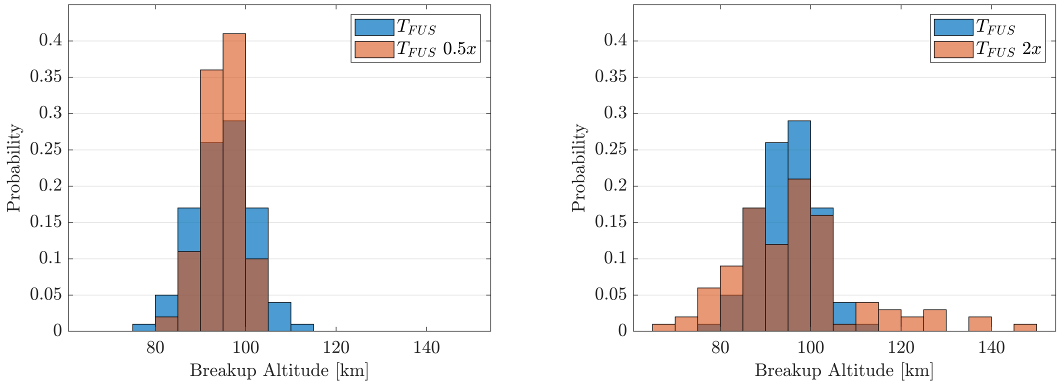

(a) Half standard deviation (b) Twice standard deviation

Figure 5.29: Sensitivity of breakup altitude to fusion temperature of the structure

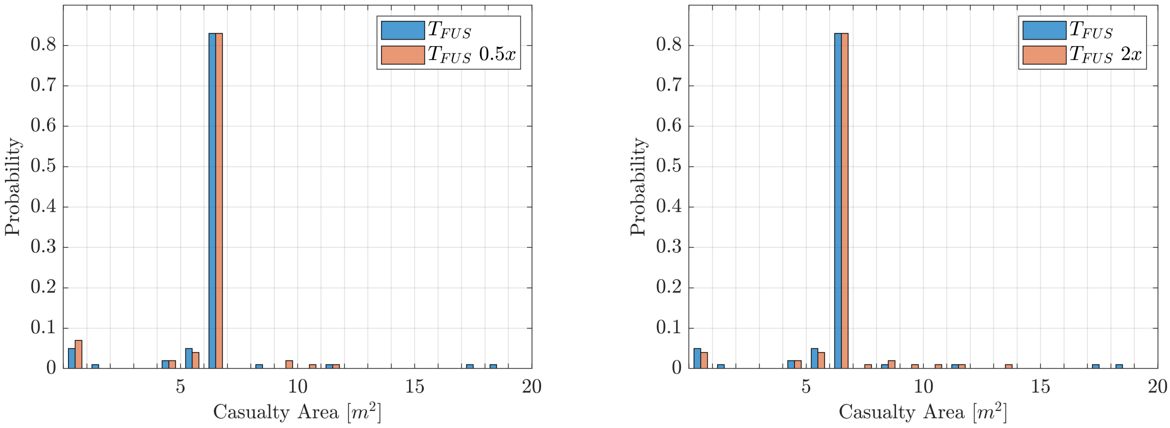

(a) Half standard deviation (Tank) (b) Twice standard deviation (Tank)

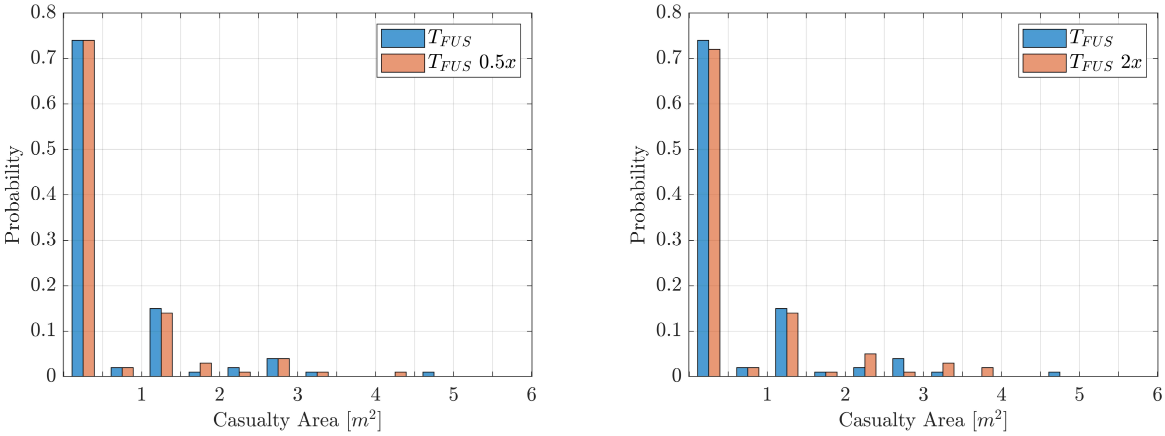

(c) Half standard deviation (Large Sphere) (d) Twice standard deviation (Large Sphere)

Figure 5.30: Sensitivity of casualty area to fusion temperature (structure)

Regarding Figure 5.30, the most probable value of casualty area remains the same and with almost the same probability, while the values of area produced by fragments move towards lower values. This latter change could be caused by different reasons: in the case of reduced uncertainty, the shorter range of breakup altitudes could induce lower levels of ablation and so less generated fragments; instead in the case of doubled standard deviation, the extended part of the range with higher altitudes could bring more elements to demise and again it could reduce the number of fragments or their final mass.

Footprint distributions make a substantial difference between the two analyzed cases. The reduced uncertainty case brings to a lower dispersion of the impact points, that are closer to the nominal impact point and also to each other, as shown in Figures 5.31a and c. Also the number of fragments is reduced with respect to the base case, lowering from 111 to 105 for the tank and from 53 to 51 for the large sphere.

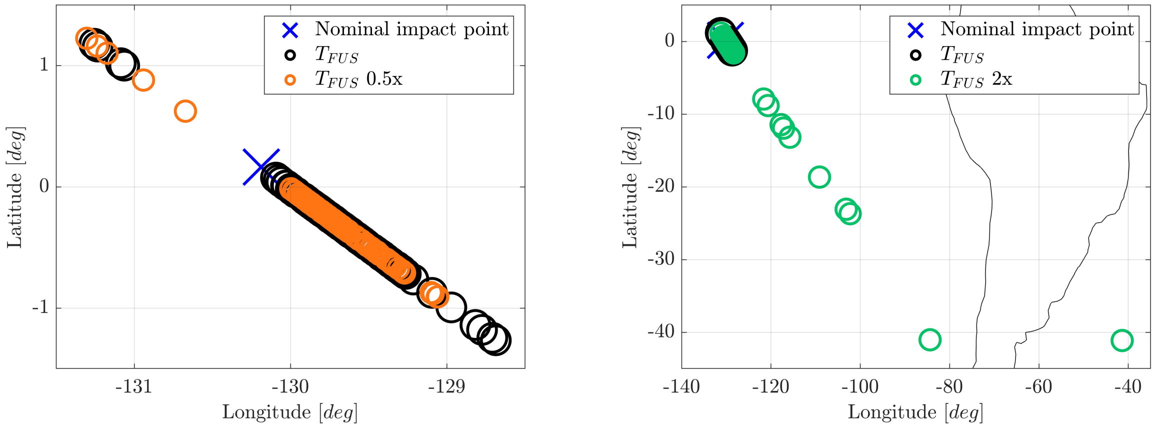

(a) Half standard deviation (Tank)

(b) Twice standard deviation (Tank)

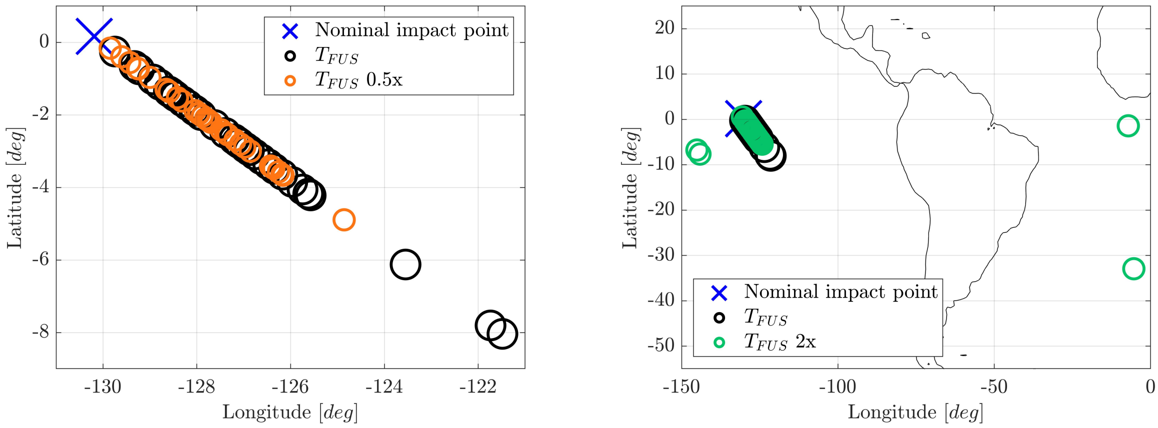

(c) Half standard deviation (Large Sphere)

(d) Twice standard deviation (Large Sphere)

Figure 5.31: Sensitivity of footprint to fusion temperature of the structure

Instead, the augmented uncertainty case causes almost the same dispersion near the nominal impact point, but the footprint shows some outliers that belongs from trials in which the breakup happens at altitudes higher than 120 km. In such cases, the vehicle is not already on the parabolic reentry path and so the elements continue the orbital trajectory according to their ballistic coefficient till they reenter into atmosphere. Then, some demise and others impact on ground. Locations of impact points are different because they are directly related to the value of drag coefficient, that is variable among different elements due to shape and among same elements due to sampling and to atmospheric conditions encountered during the descent. Moreover, the number of fragments increases with respect to the base case, passing from 111 to 115 for the tank and from 53 to 62 for the large sphere. In conclusion, in case of values of fusion temperature of the structure very far from the correct value, the range of breakup altitudes could deeply change, bringing to possible impact points distant thousands of kilometers from the predicted impact zone. This fact leads to think at reentries that are predicted to impact in the middle of the ocean but due to errors in materials modeling can affect also land areas.

5.6.2. Varying orientation factor of the structure

Referring again to Figure 5.25, the correlation of separation altitude of the structure and heat transfer orientation factor is not so evident as the previous one, but the orientation of a reentering object is a very critical parameter whose variability shall not be disregarded.

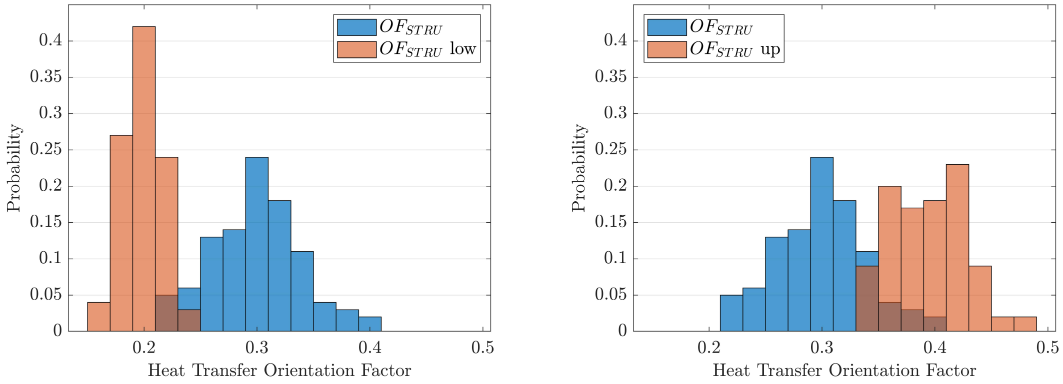

(a) Lower bound (b) Upper bound

Figure 5.32: Comparison of sampled distributions of Orientation Factor (structure)

The sampling procedure is applied again to build two new triangular distributions around the boundaries of the distribution of the base case. Thus, the sensitivity analysis is performed accounting for an uncertainty of 20% around each of the edges of the base distribution, as shown in Figure 5.32. The objective is to investigate how the lowest and highest orientation would affect the outcomes of the simulation. The new distribution in Figure 5.32a corresponds to a random spinning and tumbling cylinder, while the new one in Figure 5.32b corresponds to a stable broadside and spinning sphere.

As shown in Figure 5.33, the distribution of breakup altitudes shifts towards lower values for the lower bound case and vice versa for the upper bound case. In particular, looking at the first histogram, it comes out that a vehicle with very unstable attitude absorbs a lower net amount of heat and under particular conditions could even impact without undergoing breakup. This extreme event corresponds to the column at zero altitude that has a probability of one over the one-hundred simulated reentries. In such a case, the combination of sampled parameters consists in a very low orientation factor (0.186) and a very high couple of specific heat (1034 $\frac{J}{kg \cdot K}$) and melt temperature (1101 K) for aluminum and the structure does not reach the fusion. On the contrary, the upper bound case bring to higher values of breakup altitudes, even higher than 120 km. A modified range of altitudes of separation of the structure could deeply change the reentry path and the thermal effects on components. Therefore, also the distributions of casualty area and footprint dispersion are explored.

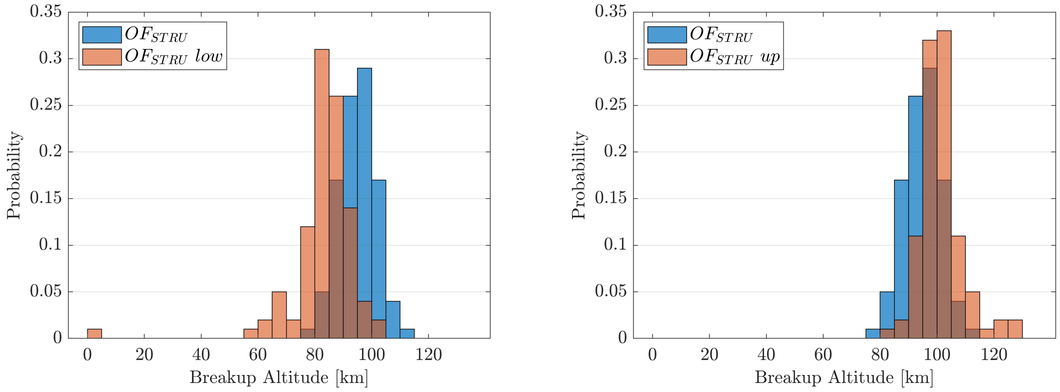

(a) Lower bound (b) Upper bound

Figure 5.33: Sensitivity of breakup altitude to Orientation Factor of the structure

Regarding casualty area, Figure 5.34 shows that in all the cases the most probable value of casualty area remains the same, with a little change in probability for the lower bound cases. Still in the graphs of lower bound case, the number of trials with zero casualty area reduces in favour of a wider range of areas higher than the one of the peak. This is caused by a higher number of impacting fragments with enough dimensions to raise the values of casualty area. In fact, the number of impacting debris pass from 111 to 124 for the tank and from 53 to 68 for the large sphere. The upper bound cases bring to even more higher values of casualty area, since higher breakup altitudes expose the elements earlier to the heat by atmospheric friction and the amount of ablation increases. According to this, partially ablated elements tend to undergo more ablation and so fragment or even demise. As already seen, an element that fragment could increase the casualty area values. This behaviour is confirmed by Figures 5.34b and 5.34d: the former is related to steel tank case, in which impacting fragments pass from 111 to 109 and consequently the probability of zero area bin increase a little due to more demised fragments but also the maximum value of area increases a lot due to higher generation of fragments; the latter is related to the large titanium sphere case, in which impacting fragments increase from 53 to 71, and consequently the range of high values of casualty area enlarges while the probability of zero area bin remains fixed because probably only fragmentation takes place.

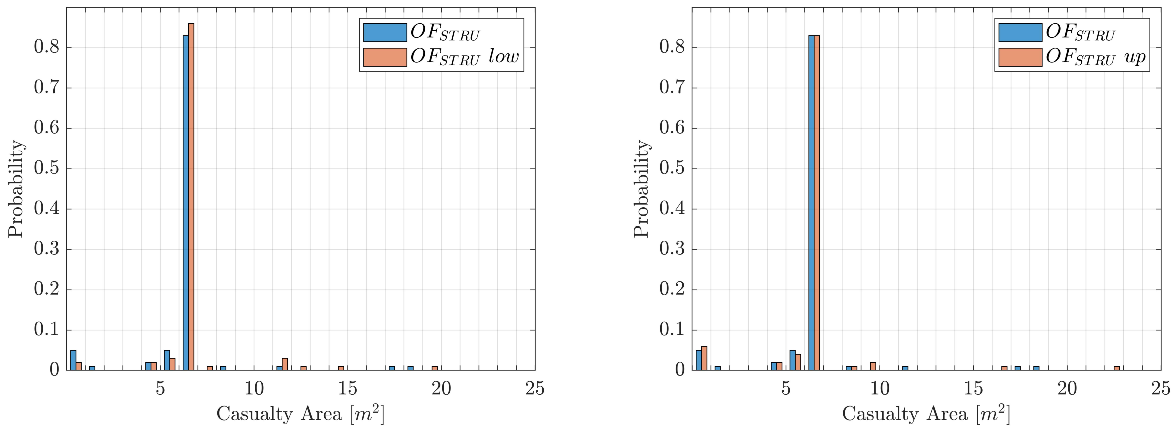

(a) Lower bound (Tank)

(b) Upper bound (Tank)

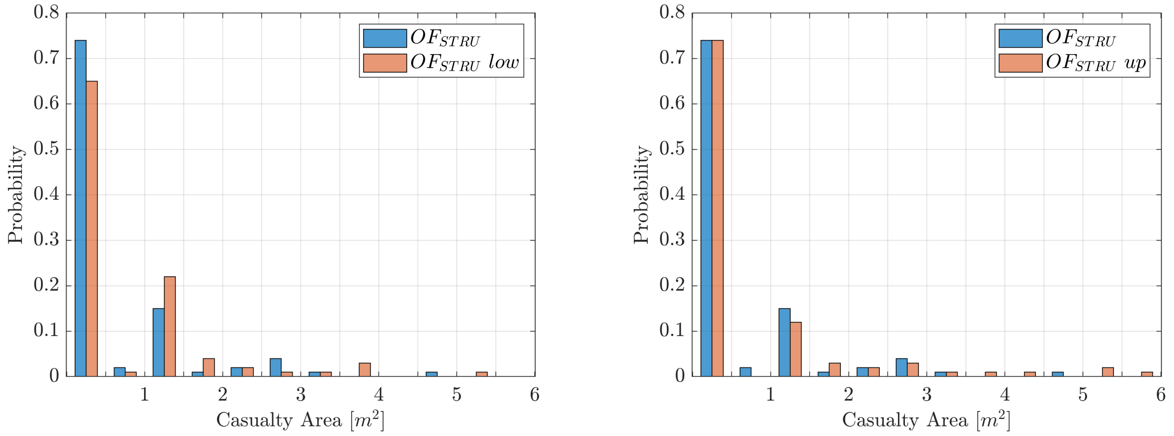

(c) Lower bound (Large Sphere)

(d) Upper bound (Large Sphere)

Figure 5.34: Sensitivity of casualty area to Orientation Factor of the structure

Regarding footprint distributions in Figure 5.35, the lower bound of orientation factor translates into a shorter dispersion of impact points, while the upper bound distribution causes a wider dispersion due to a correspondent range of higher breakup altitudes. In particular in Figure 5.35d, there is a fragment of the large sphere that falls very distant from the others. This outlier corresponds to a trial in which the separation of the structure happens above 120 km, thanks to an orientation factor of 0.444 in combination with a melt temperature of 722 K and a specific heat of 922 $\frac{J}{kg \cdot K}$. Also other reentries have similar separation altitudes but in those cases the elements demise. Such an impact point is present only in the large sphere graph because for the same reentry the steel tank has an higher drag coefficient and so it follows a different path, falling closer to the nominal impact point.

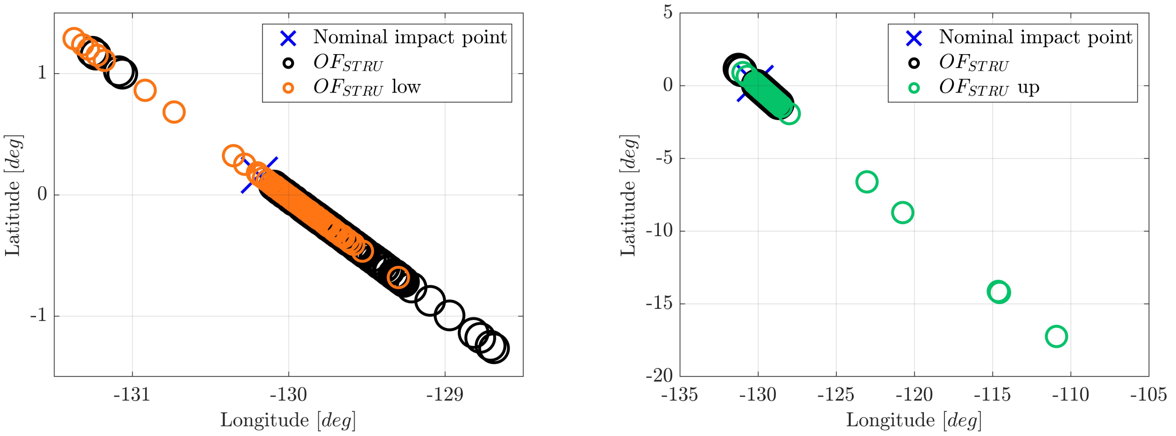

(a) Lower bound (Tank)

(b) Upper bound (Tank)

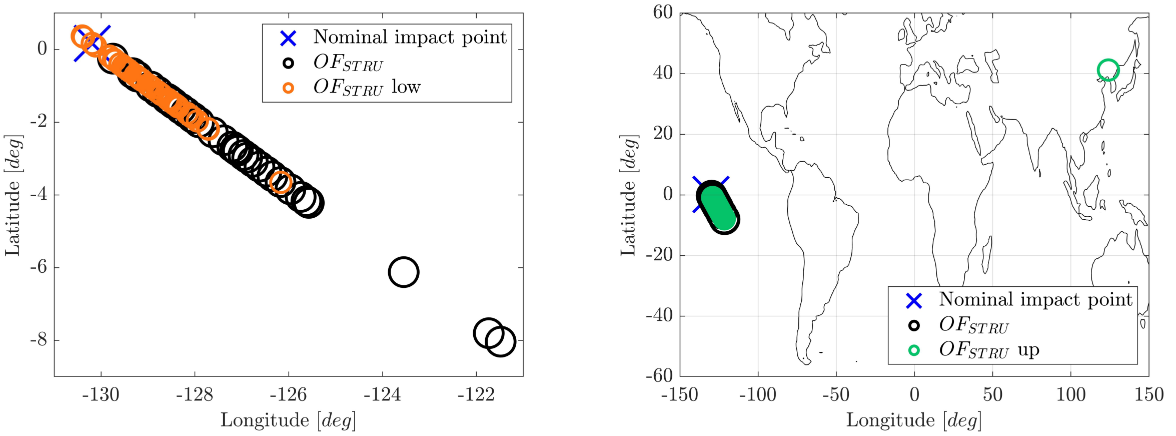

(c) Lower bound (Large Sphere)

(d) Upper bound (Large Sphere)

Figure 5.35: Sensitivity of footprint to Orientation Factor of the structure

In conclusion, variations in orientation factor change the casualty area distribution. Moreover, higher values of orientation factor increase the range of breakup altitudes, bringing to a more dispersed footprint and to fragments that impact very far from the expected zone.

5.6.3. Varying melt temperature of elements

Melt temperature of an element drives the start of ablation process. An element with higher fusion temperature is likely to undergo less mass ablation and so it will impact with a higher final mass. Therefore, this section investigates the effects of fusion temperature on fusion altitude and final mass for both the steel tank and the titanium large sphere. In addition, the modified distributions of casualty area and footprint are included only if there are noticeable changes.

Steel Tank

The sampling procedure is applied again to build the two new normal distributions with half and double standard deviation with respect to the base case. The new sets of temperature are compared with the base one in Figure 5.36.

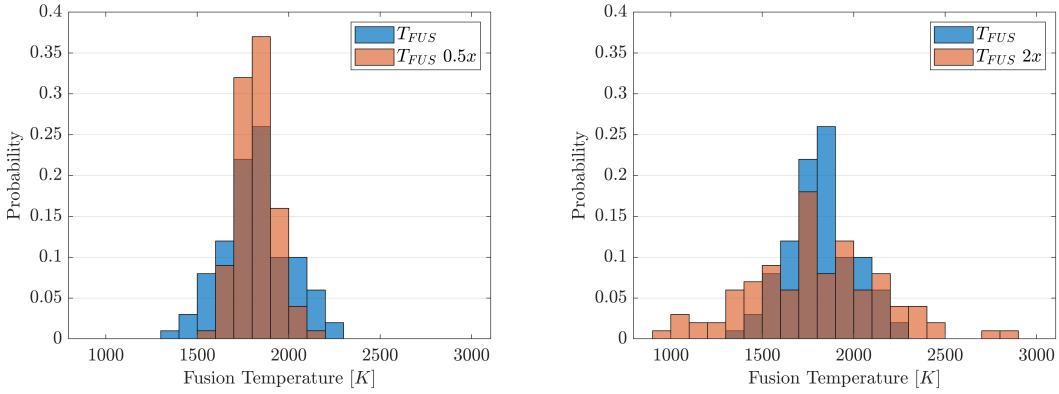

(a) Half standard deviation (b) Twice standard deviation

Figure 5.36: Comparison of sampled distributions of fusion temperature (Steel Tank)

The effects on fusion altitude distributions are shown in Figure 5.37. It comes out that the reduced uncertainty distribution causes an increase in the probability that the element impacts without reaching the melt temperature. At the same time, the range of fusion altitudes does not change. This can be related to the fact that central values of the distribution of the parameter and so values closer to the mean value of the material melt temperature are more likely to prevent the fusion of the element. This behaviour is confirmed by the augmented uncertainty distribution effects on fusion altitude distribution of Figure 5.37b. Peripheral values of melt temperature increase the number of elements that reach fusion during the reentry and also spread the probability range towards higher fusion altitudes. Consequently in Figure 5.38, the final mass distribution of the halved standard deviation case is moved towards the initial mass value, while the other case spreads the probability over intermediate and zero values of mass.

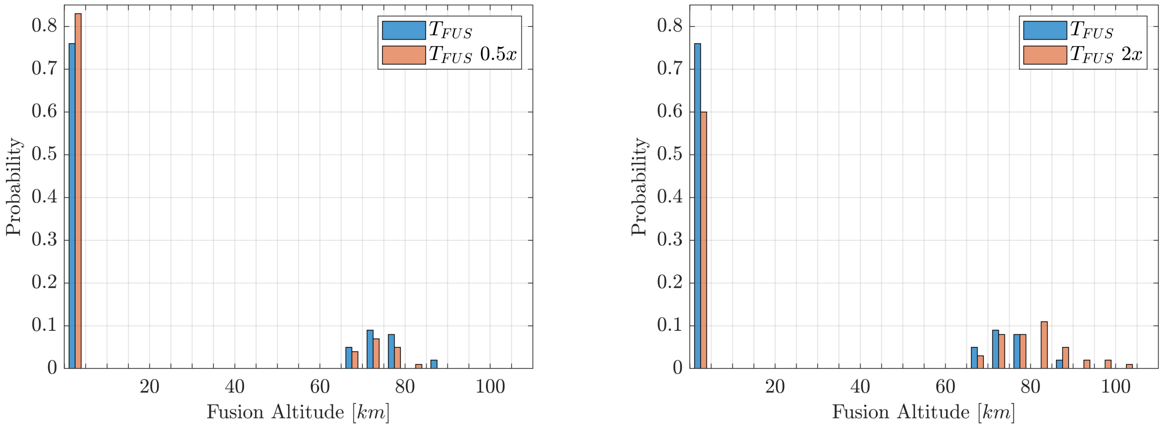

(a) Half standard deviation (b) Twice standard deviation

Figure 5.37: Sensitivity of fusion altitude to fusion temperature (Steel Tank)

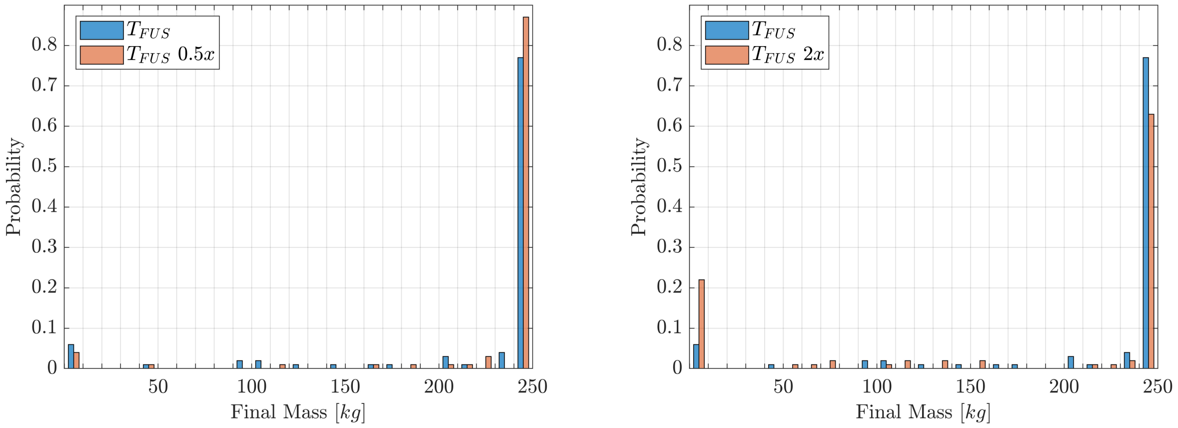

(a) Half standard deviation (b) Twice standard deviation

Figure 5.38: Sensitivity of final mass to fusion temperature (Steel Tank)

The effects observed above affect the casualty area in Figure 5.39. The reduced uncertainty case increases the probability of the nominal value of casualty area corresponding to an intact impacting element. On the opposite the augmented uncertainty case increases the probabilities to have zero casualty area, due to more elements that demise. In both cases fragmentation is reduced. As a consequence, the footprint is almost the same of the base case and the number of impacting fragments lowers from 111 to 103 and from 111 to 84, respectively.

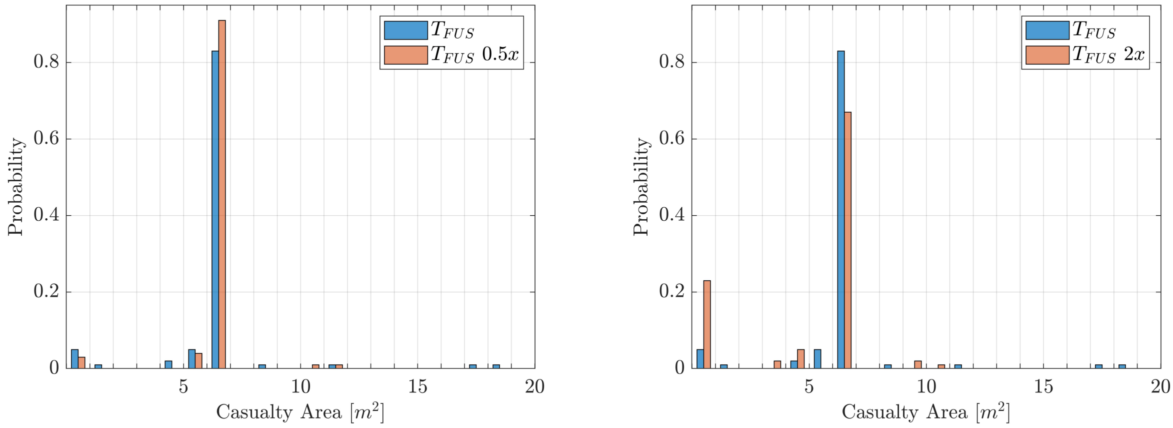

(a) Half standard deviation (b) Twice standard deviation

Figure 5.39: Sensitivity of casualty area to fusion temperature (Steel Tank)

Titanium Large Sphere

The sensitivity analysis to material melt temperature is here repeated for the titanium large sphere, because a different material and a different shape could produce different outcomes. Two new normal distributions with half and double standard deviation with respect to the base case are generated and compared with the base one in Figure 5.40.

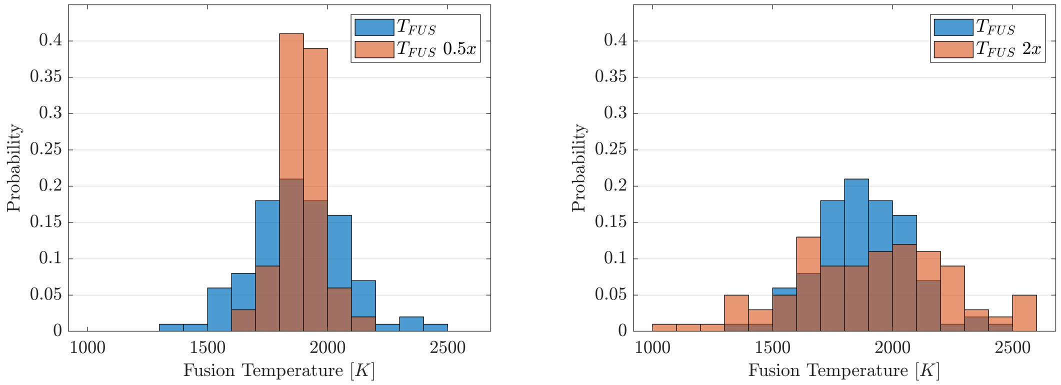

(a) Half standard deviation (b) Twice standard deviation

Figure 5.40: Comparison of sampled distributions of fusion temperature (Large Sphere)

Observing Figure 5.41, it comes out that the reduced uncertainty distribution deletes the zero fusion altitude bin and increases the probability of the range from 60 to 85 km. On the contrary, the augmented uncertainty distribution causes an increase in the probability that the element impacts without reaching the melt temperature in spite of the range of fusion altitudes, that is also extended by a little over higher altitudes. Consequently in Figure 5.42, the final mass distribution of the halved standard deviation case is moved towards the zero, while the other case spreads the probability towards intermediate and initial values of mass.

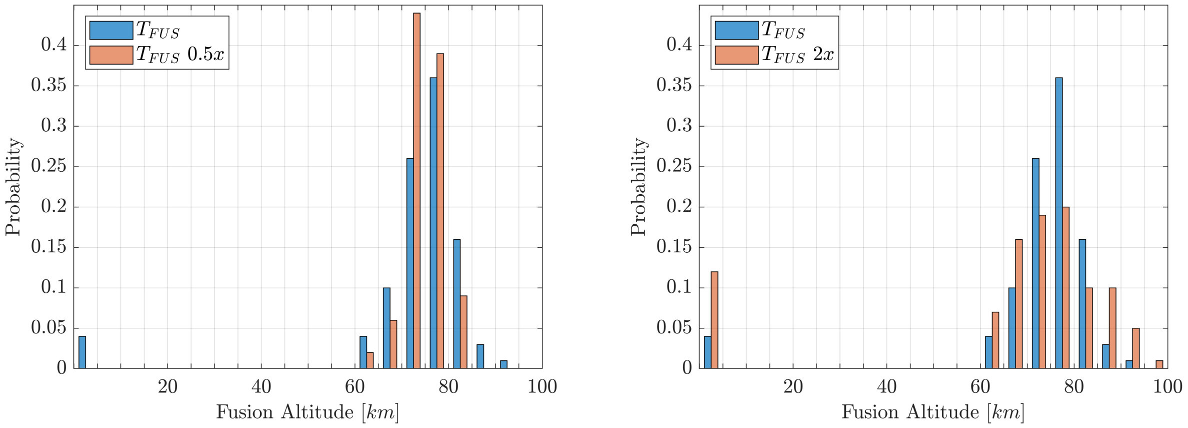

(a) Half standard deviation (b) Twice standard deviation

Figure 5.41: Sensitivity of fusion altitude to fusion temperature (Large Sphere)

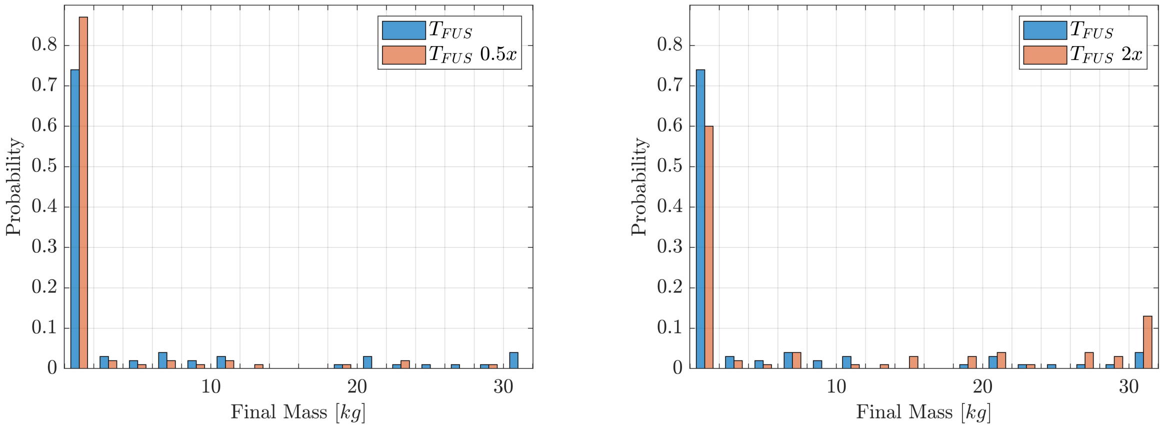

(a) Half standard deviation (b) Twice standard deviation

Figure 5.42: Sensitivity of final mass to fusion temperature (Large Sphere)

The effects observed above affect the casualty area in Figure 5.43. The reduced uncertainty case increases the probability to have zero casualty area, due to more elements that demise. On the opposite the augmented uncertainty case increases the probabilities of the nominal value of casualty area corresponding to an intact impacting element. In both cases fragmentation is increased, producing higher values of maximum casualty area.

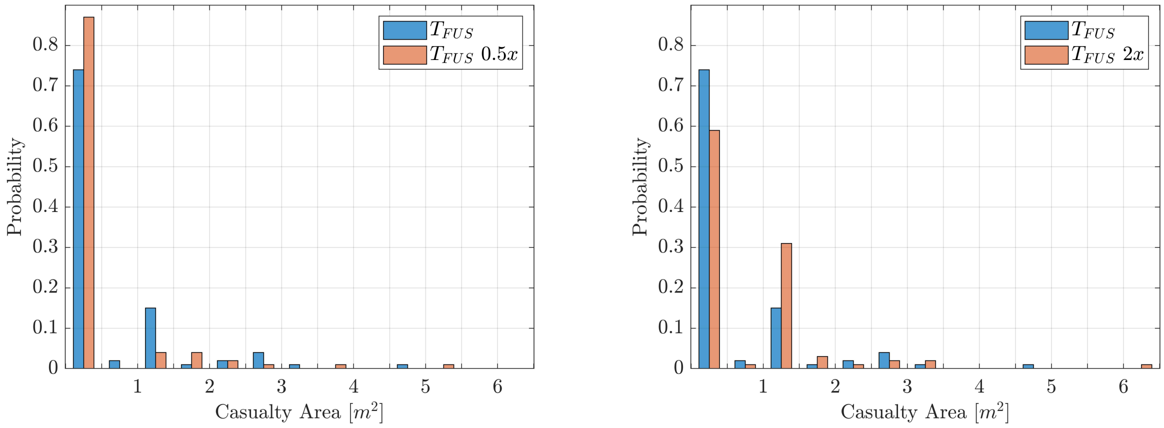

(a) Half standard deviation (b) Twice standard deviation

Figure 5.43: Sensitivity of casualty area to fusion temperature (Large Sphere)

Finally, the footprint is almost the same of the base case and the number of impacting fragments passes from 53 to 36 for the reduced uncertainty and from 53 to 70 for the augmented uncertainty.

The sensitivity to fusion temperature of the titanium large sphere gives opposite results with respect to the steel tank. Since each element has its own set of parameters, probably the motivation of opposite behaviour lies in the combination of parameters and maybe also the modeling shape through the values of orientation factor. In fact, the sphere has a less wide range of heat transfer orientation factors with respect to the tank, that on the contrary is more unstable and so could be more sensitive to variation in melt temperature.

5.6.4. Varying material emissivity of elements

The emissivity is a tricky parameter to set, since it depends on surface finishing, coatings, composition of alloys and typically space components employ materials that undergo many manufacturing processes. Thus, the variability of emissivity has been investigated.

Steel Tank

Two new normal distributions with half and double standard deviation with respect to the base case are generated and compared with the base one in Figure 5.44. Then the effects on fusion altitude, final mass and casualty area distributions are shown respectively in Figures 5.45, 5.46, 5.47.

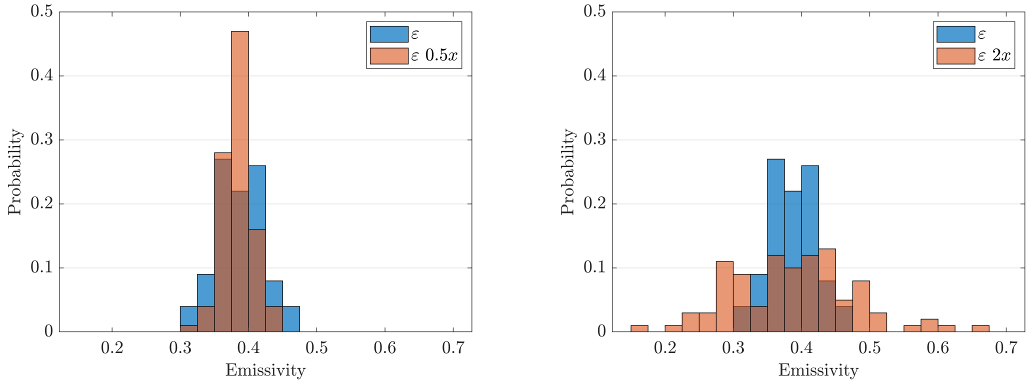

(a) Half standard deviation (b) Twice standard deviation

Figure 5.44: Comparison of sampled distributions of material emissivity (Steel Tank)

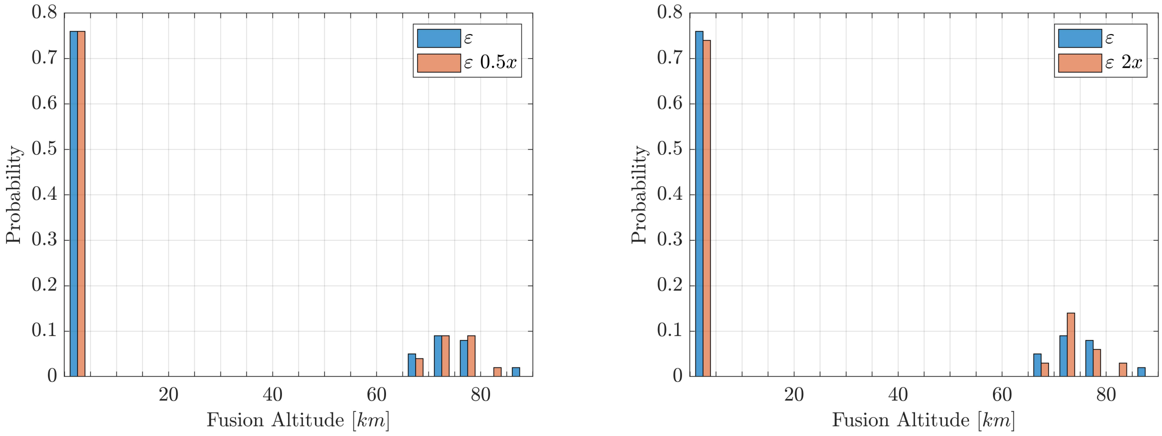

(a) Half standard deviation (b) Twice standard deviation

Figure 5.45: Sensitivity of fusion altitude to material emissivity (Steel Tank)

Figure 5.45b shows that if a wider range of emissivity is considered the distribution of fusion altitudes changes. Higher values of emissivity bring to a reduction of the higher bound of the fusion altitudes range, while lower values of emissivity reduce the probability of element impacting without reaching the fusion temperature. In fact, emissivity is directly related to the amount of heat radiated by the element: lower emissivity means higher net absorbed heat.

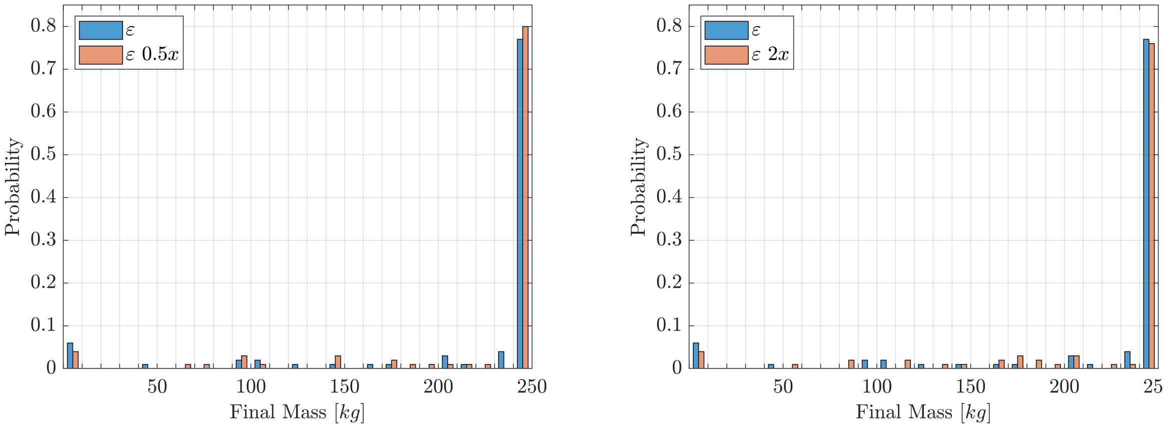

(a) Half standard deviation (b) Twice standard deviation

Figure 5.46: Sensitivity of final mass to material emissivity (Steel Tank)

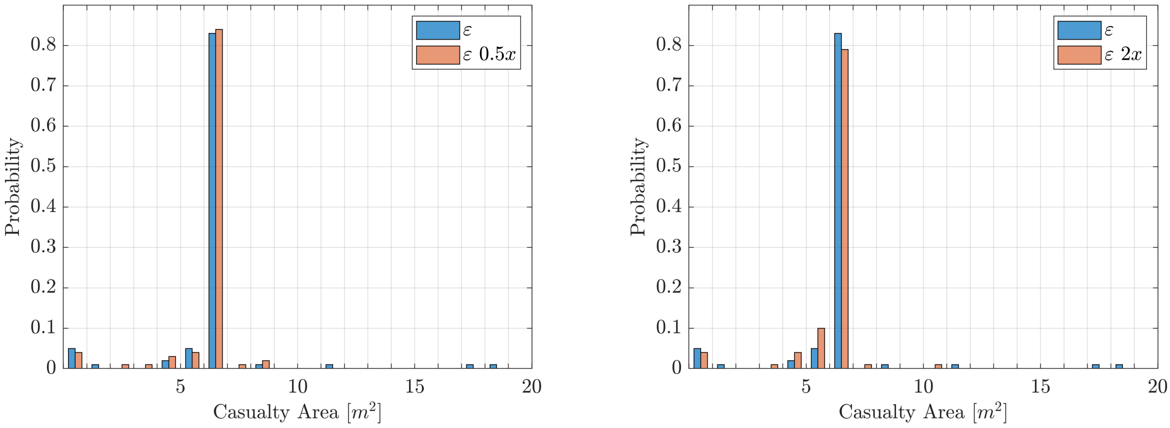

(a) Half standard deviation (b) Twice standard deviation

Figure 5.47: Sensitivity of casualty area to material emissivity (Steel Tank)

Figure 5.46 shows that for central values of the emissivity distribution the final mass is spread towards the highest value, while for peripheral values the final mass is distributed over intermediate values. This latter effect is probably due to the fact that low values of emissivity tend to promote fusion and then ablation of the element while high values tend to do the opposite, so in Figure 5.46b the probabilities of both the lowest and highest mass values decrease in favour of the intermediate values.

Finally in Figure 5.47, the casualty area distributions are not so different from the one of the base case, except for a shift of bins towards the left, probably caused by reduced fragmentation. The footprint dispersion is almost the same and the number of impacting fragments pass from 111 to 102 in both the two cases.

Altogether, the effect of variation of the range of emissivity is not so evident, but it is important to remark that the sensitivity is done on a percentage of the main value and so the change in emissivity value is not so great. This does not allow to understand what can be the effect of different magnitudes of emissivity, as for example in case of particular surface finishing or different coatings. However, these are very peculiar conditions and they would require an analysis on a too wide range of emissivity with so many samples that would result unfeasible. In any case, the main effects come from the augmented uncertainty case.

Titanium Large Sphere

The results of the analysis on the large sphere are omitted because they replicate the effects already seen for the steel tank.

5.6.5. Varying heat transfer orientation factor of elements

While the emissivity acts directly of the radiative heat term in the thermal model, conversely the heat transfer orientation factor modifies the convective heat term. Higher values of OF cause higher values of absorbed net heat.

Steel Tank

The sampling procedure is applied again to build two new triangular distributions around the boundaries of the distribution of the base case. Thus, the sensitivity analysis is performed accounting for an uncertainty of 20% around each of the edges of the base distribution, as shown in Figure 5.48. The objective is to investigate how the lowest and highest orientation would affect the outcomes of the simulation. The new distribution in Figure 5.48a corresponds to a random spinning and tumbling cylinder, while the new one in Figure 5.48b corresponds to a broadside stagnation orientation.

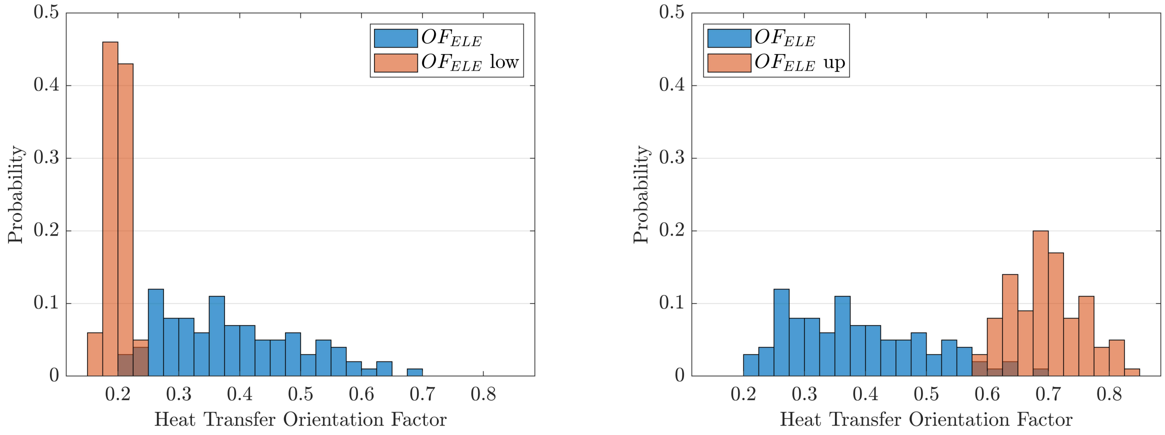

(a) Lower bound (b) Upper bound

Figure 5.48: Comparison of sampled distributions of Orientation Factor (Steel Tank)

The effects on the fusion altitude distribution are evident in Figure 5.49. The lower bound distribution causes that almost all the probability moves towards the bin at zero altitude. This means that elements falling with an unstable attitude absorb very low amount of net heat and so impact without reaching the fusion temperature. On the contrary, an element that has a stable attitude and exposes its larger side to the cross flow is more likely to melt during the reentry, even at higher altitudes than the base case, as can be seen in the graph of the upper bound distribution in Figure 5.49b. These considerations affect the final mass distribution in Figure 5.50. The lower bound case induces all the elements to impact with the initial mass, while the upper bound case increases the overall ablation percentage and leads to a most probable value of zero for the final mass.

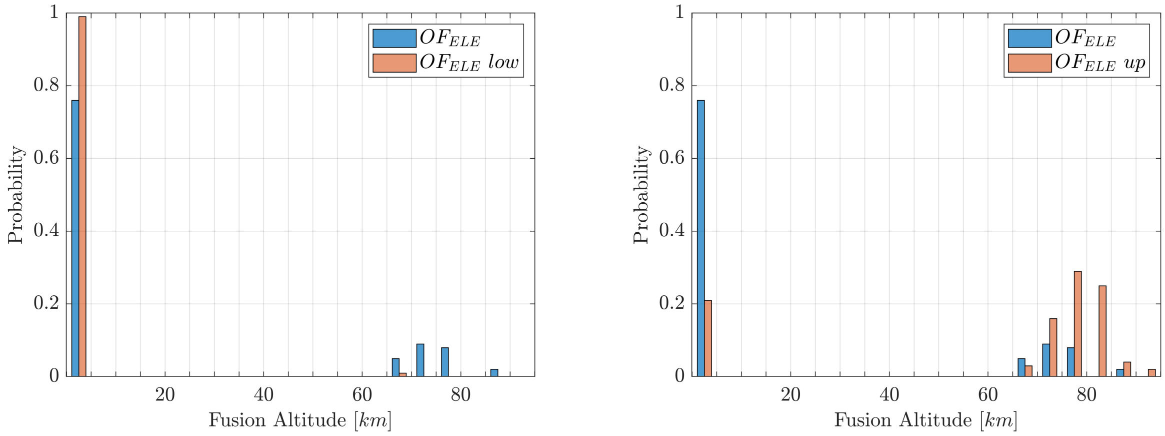

(a) Lower bound (b) Upper bound

Figure 5.49: Sensitivity of fusion altitude to Orientation Factor (Steel Tank)

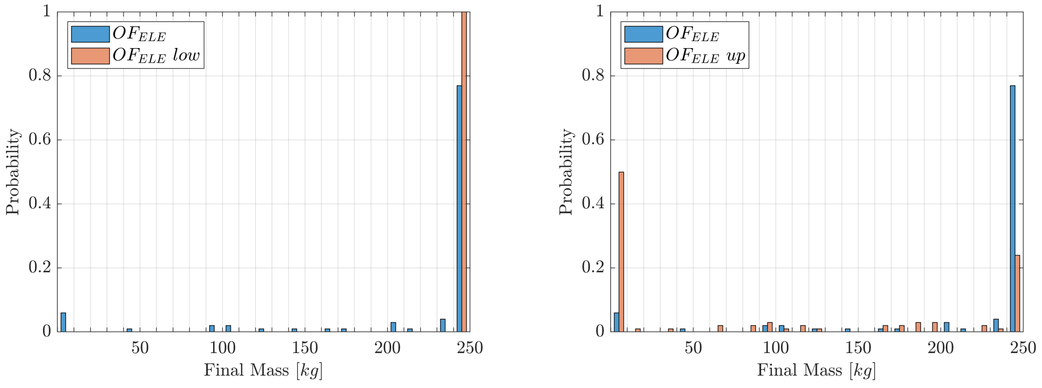

(a) Lower bound (b) Upper bound

Figure 5.50: Sensitivity of final mass to Orientation Factor (Steel Tank)

The distributions of final mass reflect on the casualty area in Figure 5.51. The lower bound case gives only the nominal value of casualty area with a probability of 1. This means that in all the simulated reentries the steel tank impacts intact, due only to the low value of orientation factor and whatever are the values of other parameters. This is confirmed by the number of impacting fragments, that are exactly 100 as the impacting elements. Instead, Figure 5.51b shows that the probability of the nominal value of area lowers and spreads towards both the zero casualty area and higher values corresponding to generation of fragments. The latter part gives very high values of casualty area near $25m^2$, but this is the results of the sum of many fragments that would probably impact in different locations, so that the casualty area on ground related to each fragment should be smaller. In this case, the number of impacting fragments passes from 111 to 85 and it can be even lower without fragmentation because the percentage of demise is quite high.

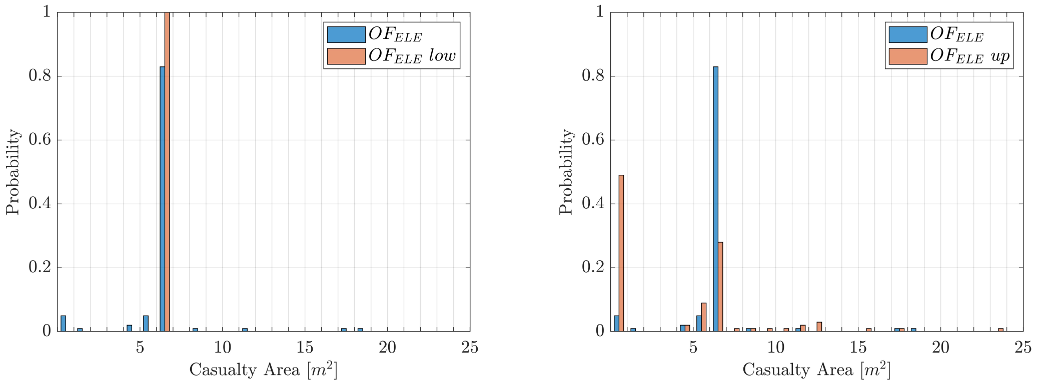

(a) Lower bound (b) Upper bound

Figure 5.51: Sensitivity of casualty area to Orientation Factor (Steel Tank)

Titanium Large Sphere

The sensitivity analysis to the orientation factor is repeated in the same way also for the titanium large sphere. The new distribution in Figure 5.52a corresponds to a more unstable attitude represented by an uncertainty of 20% around the lower bound of the base case distribution, while the new distribution around the upper bound in Figure 5.52b corresponds to a more stable attitude. The fusion altitude distributions change accordingly in Figure 5.53. The lower bound case induces less net heat absorption and so the probability range moves towards lower values of altitude. In particular, the number of impacting intact elements is doubled. The upper bound case has the opposite effect, since the probability range moves towards higher altitudes.

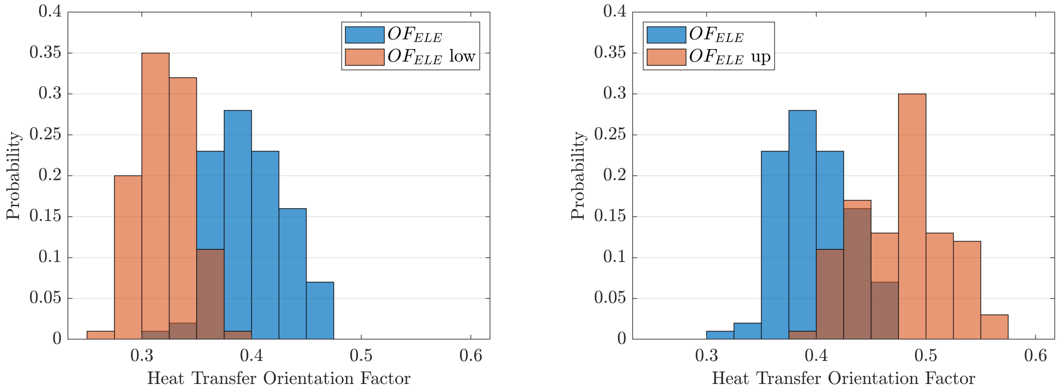

(a) Lower bound

(b) Upper bound

Figure 5.52: Comparison of sampled distributions of Orientation Factor (Large Sphere)

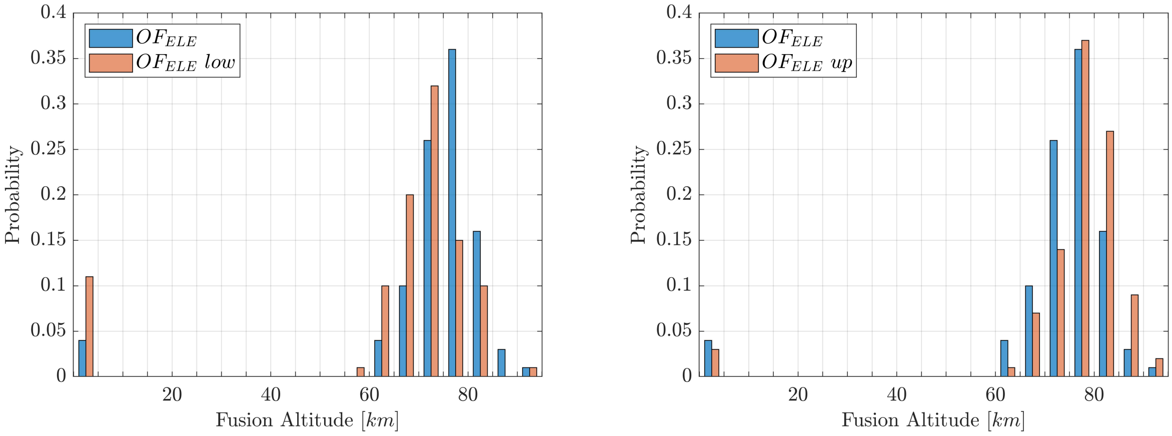

(a) Lower bound

(b) Upper bound

Figure 5.53: Sensitivity of fusion altitude to Orientation Factor (Large Sphere)

The final mass distributions in Figure 5.54 change consequently. In the first graph the range of final masses moves towards higher values corresponding to lower overall ablation, while in the second graph the amount of ablated mass increases and also does the probability of demise. Such distributions reflect on the casualty area in Figure 5.55. In the lower bound case, the probability of the nominal value increases and the number of impacting fragments pass from 53 to 67. In the upper bound case, the probability of having zero casualty area increases as the number of impacting fragments decreases from 53 to 37. However, there are also new high values of area due to more fragmentation events caused by the elevated percentages of mass ablation.

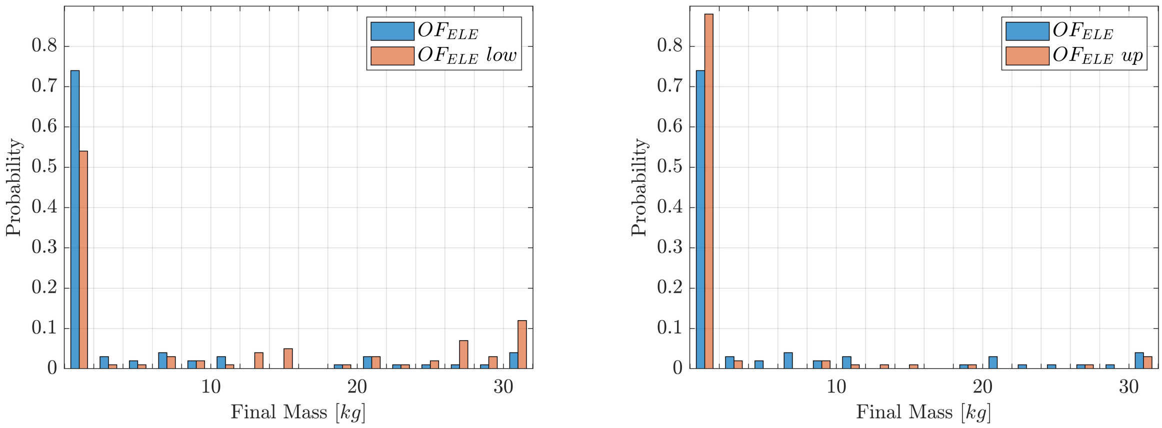

(a) Lower bound (b) Upper bound

Figure 5.54: Sensitivity of final mass to Orientation Factor (Large Sphere)

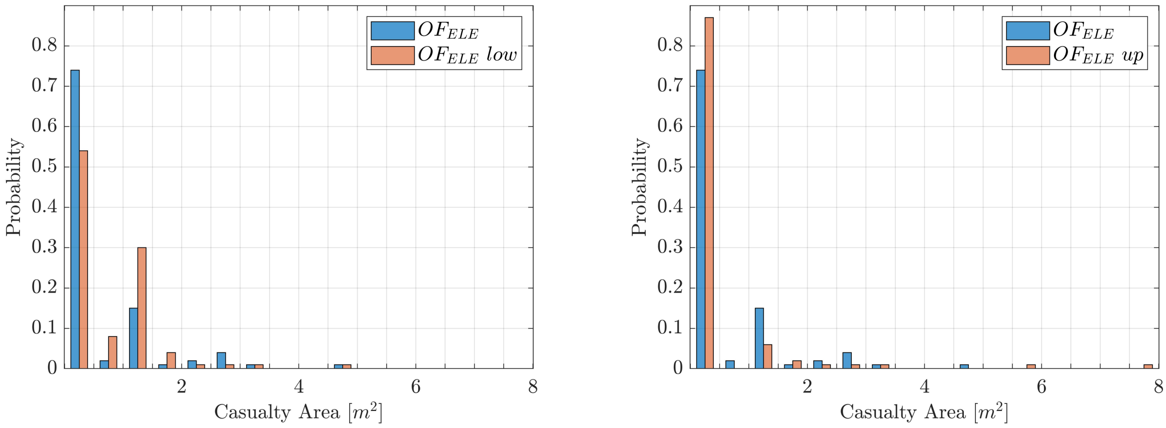

(a) Lower bound (b) Upper bound

Figure 5.55: Sensitivity of casualty area to Orientation Factor (Large Sphere)

5.6.6. Varying drag coefficient of elements

Relying on the variation of nominal impact points due to change in drag coefficient of the vehicle in Section 5.2.1, the sensitivity to the drag coefficient of the elements is here performed to investigate the variation in footprint dispersion.

Steel Tank

Two new uniform distributions with half and double standard deviation with respect to the base case are generated and compared with the base one in Figure 5.56.

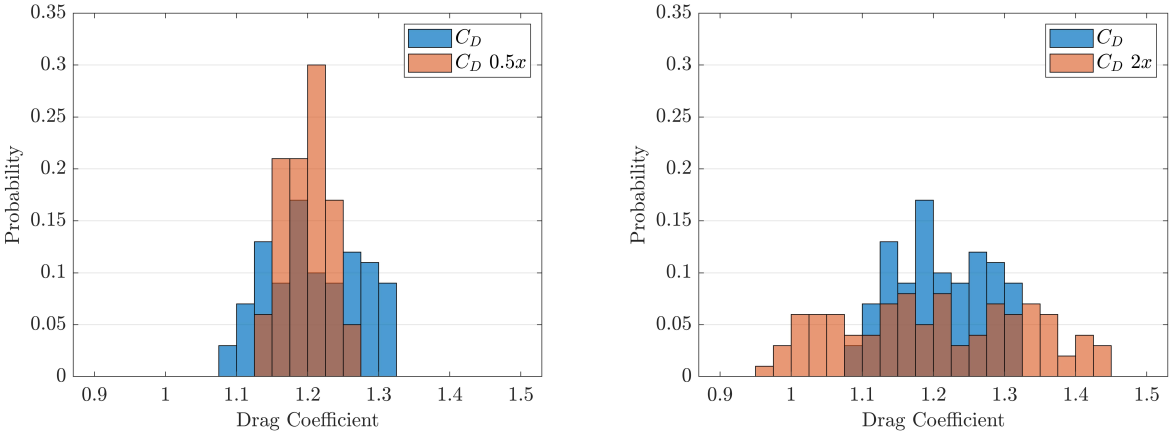

(a) Half standard deviation

(b) Twice standard deviation

Figure 5.56: Comparison of sampled distributions of drag coefficient (Steel Tank)

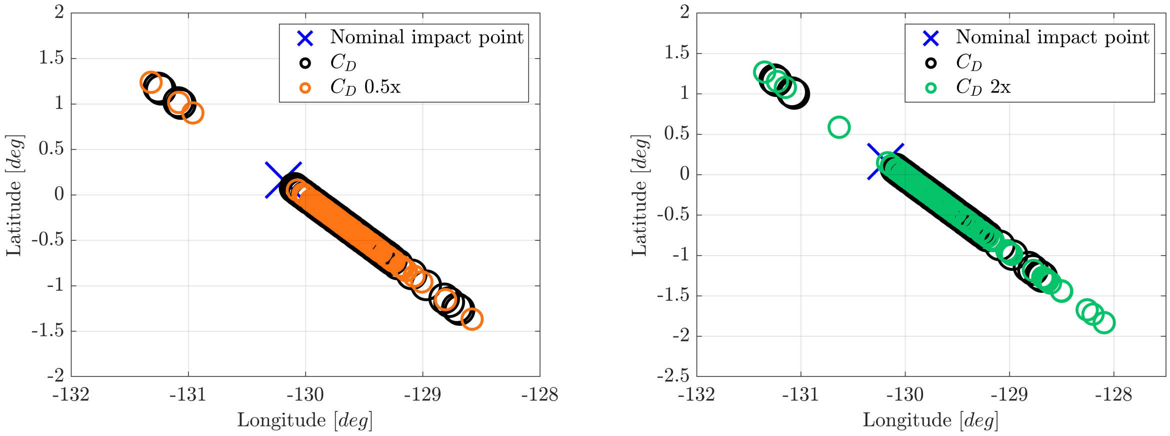

(a) Half standard deviation

(b) Twice standard deviation

Figure 5.57: Sensitivity of footprint to drag coefficient (Steel Tank)

The changes in fusion altitude and final mass distribution are negligible. Also the distribution of casualty area is almost the same, except for a reduction of highest values from about $20m^2$ to about $10m^2$.

Even the expected changes in footprint dispersion are not so evident, as shown in Figure 5.57. The black circles are larger only for make the graphs more readable. In both cases the number of impacting fragments reduces respectively from 111 to 101 and from 111 to 104.

Titanium Large Sphere

The procedure is repeated also for the titanium large sphere in order to understand if a change in the analyzed element brings to more clear effects. Two new uniform distributions with half and double standard deviation with respect to the base case are generated and compared with the base one in Figure 5.58.

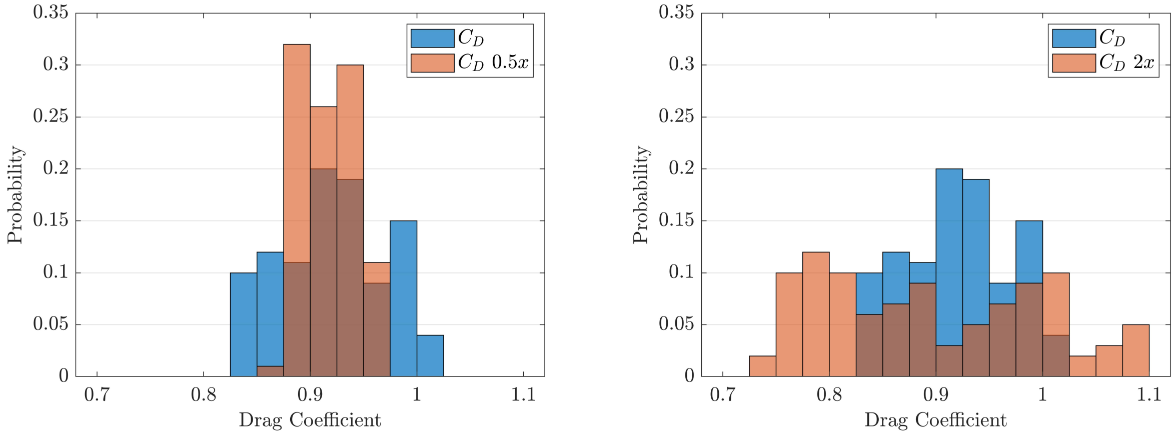

(a) Half standard deviation

(b) Twice standard deviation

Figure 5.58: Comparison of sampled distributions of drag coefficient (Large Sphere)

The results follow the same trend obtained for the steel tank. The changes in fusion altitude and final mass distribution are negligible. The distribution of casualty area is almost the same of the base case.

Also the footprint dispersions are not so different from the base case, as shown in Figure 5.59. The black circles are larger only for make the graphs more readable. In the reduced uncertainty case, the number of impacting fragments increases from 53 to 65. In fact, there are more points right after the nominal one. Instead in the augmented uncertainty case, the number of impacting fragments decreases from 53 to 40. In fact, the impact points right after the nominal one are sparser and they are scattered towards the terminal part of the footprint.

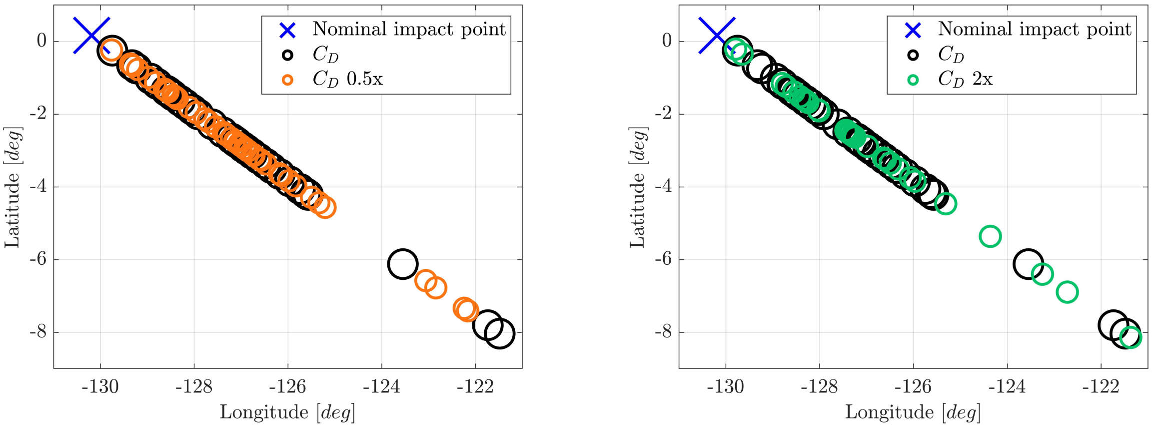

(a) Half standard deviation (b) Twice standard deviation

Figure 5.59: Sensitivity of footprint to drag coefficient (Large Sphere)

In conclusion, the variation of footprint dispersion due to the variation of drag coefficient of elements is poor. This is quite unexpected because a change in drag coefficient should modify significantly the trajectory and so the impact point location. Probably, the range of separation altitudes of the base case (from 110 to 75 km) drives the shape of the subsequent trajectory in a way that a change in drag coefficient does not affect to much the path. In particular, a trajectory that is steep enough will be less affected than a smooth trajectory like the orbital path. In fact, the cases of breakup at altitudes over 120 km that arise in other sensitivity analyses bring to impact points very far from the bulk of the main points because the elements have a lower C_D with respect to the vehicle and so they depart from the nominal reentry path going on along a decaying orbit. On the contrary, the motivation could be either that the uncertainty considered or the number of simulated reentry are not enough to appreciate great differences in the outcomes.

5.7. Additional results

5.7.1. Variation of eccentricity of the initial orbit

According to the target orbit of the mission, upper stages could be released on orbits that have different values of eccentricity. This parameter reflects mainly on the size of the orbit and on the altitude of the apogee. Without conducting a complete sensitivity analysis, this section simply halves and doubles the eccentricity of the orbit of the base case and runs the reentry algorithm for both cases. The modification of the eccentricity is done computing the orbital parameters at the first perigee passage after the initial point and modifying the eccentricity keeping fixed the perigee radius. Finally, the semi-major axis is updated so as not to change the other orbital parameters.

Figure 5.60 shows the new obtained paths followed by the main vehicle from the last apogee to ground. The base case (Figure 5.4a) has an eccentricity of 0.0171. The latitude band overflown is the same but there are changes in the length of the ground track, especially in the augmented eccentricity case. Moreover, the locations of peculiar points are completely different. Probably, these effects are caused by differences in the overall reentry time from the initial epoch and flight path angle during reentry path.

Figure 5.61 shows the altitude profile of each case. The double eccentricity case takes less time to reach the ground and this explains the shorter ground track. The other two cases take almost the same time and this explains the same length of the ground track, hence the difference in location of the nominal impact point is due to different reentry points.

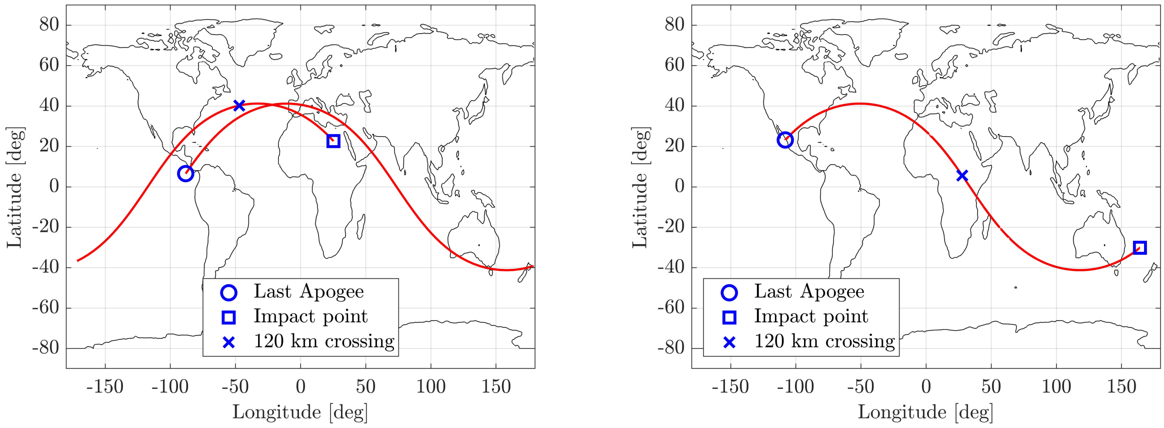

(a) Half eccentricity (b) Double eccentricity

Figure 5.60: Ground track from last apogee to ground (modified eccentricity)

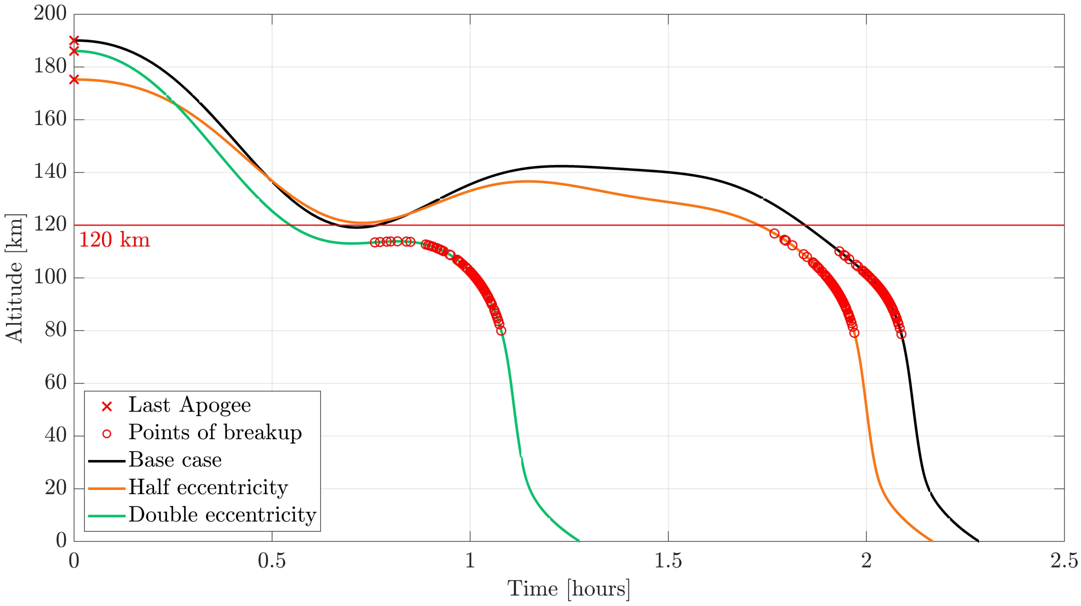

Figure 5.61: Altitude profile from the last apogee to ground (modified eccentricity)

Of course the overall time from initial point to ground is different among the three cases, because higher eccentricity means higher altitude of the apogee and so lower net effect of atmospheric drag over the whole orbit. In fact, the orbit with half eccentricity makes only 4 revolutions before reentry against the 12 of the base case. Consequently the time needed is about 6 hours. Instead, the orbit with double eccentricity raises its apogee up to an altitude of 600 km and it makes 37 revolutions before reentry. Consequently the time needed is more than 2 days. On the opposite, the time to reach the ground is the lowest in this case, probably due to a steeper trajectory at the reentry epoch.

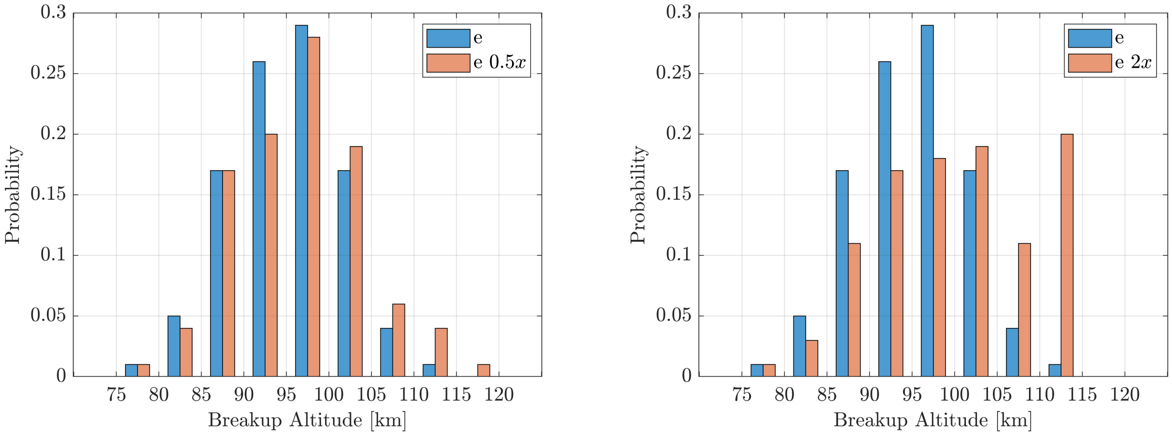

(a) Half eccentricity

(b) Double eccentricity

Figure 5.62: Breakup altitude (modified eccentricity)

Figure 5.62 compares the breakup altitude distribution among the three different eccentricities. The augmented case causes a redistribution of the probability fields towards higher altitudes.

The outcomes of the reentry analysis are reported in Figures 5.63 and 5.64 for the steel tank and titanium large sphere elements.
The distributions of casualty area of each element remain almost the same with no significant variation in the probability of each range. Only the maximum value of casualty area for the titanium sphere is raised from almost $5m^2$ to almost $8m^2$ in the double eccentricity case, probably because the increased range of high breakup altitudes produces a greater exposure of the element to the heat flux and so an increased fragmentation. On the contrary, the half eccentricity case produces a slight shift of the casualty area range towards lower values.

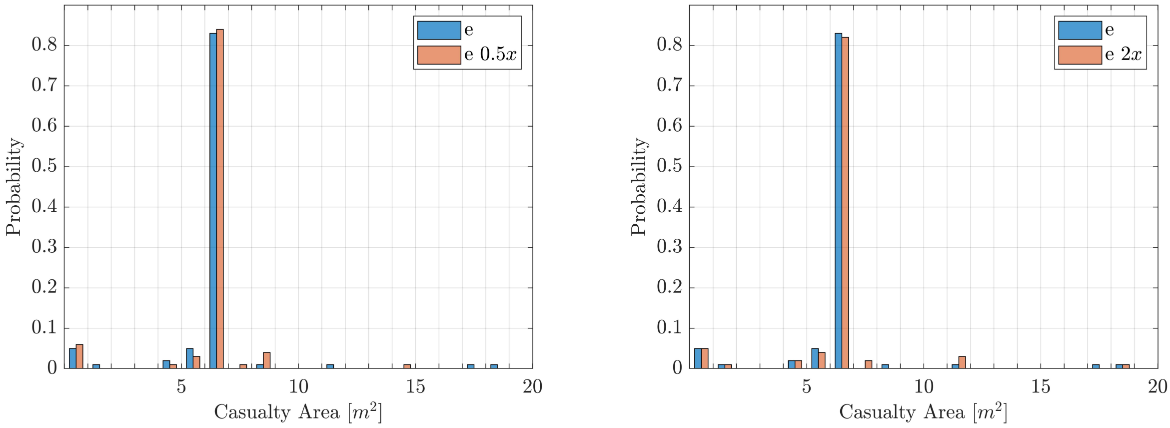

(a) Steel Tank (0.5e)

(b) Steel Tank (2e)

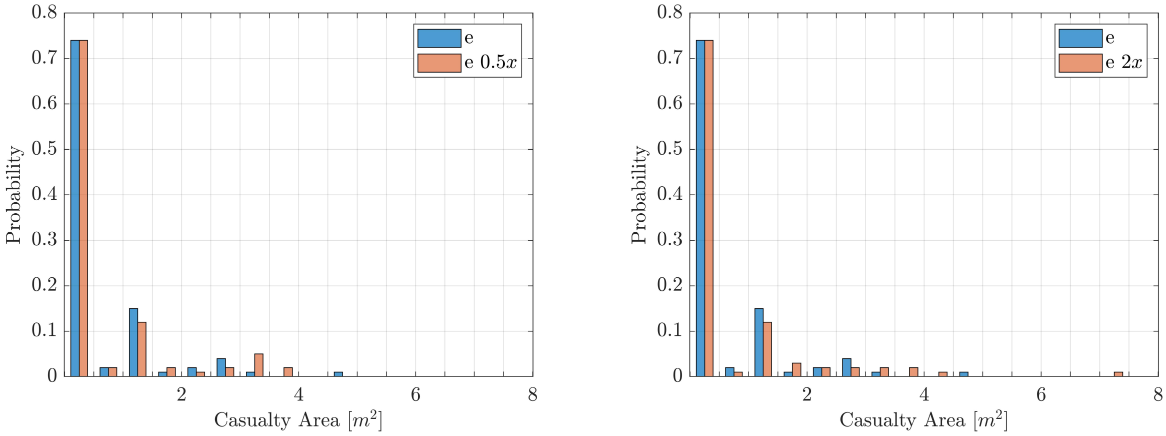

(c) Titanium Large Sphere (0.5e)

(d) Titanium Large Sphere (2e)

Figure 5.63: Casualty area of tank and large sphere (modified eccentricity)

Regarding the footprint dispersions of the fragments of each element, it is not possible to compare them due to different locations of the nominal impact point and also due to different inclinations of the path. However, footprints have almost the same dispersion among the two cases and there is also a similarity with the ones of the base case (Figure 5.17a and 5.17b). In fact, the bulk of the fragments is again near the nominal point and the large sphere presents an augmented dispersion after the nominal point. More precisely, the case with double eccentricity brings to an increased dispersion after the nominal point for both the elements. This effect can be again related to the increased probability of high separation altitudes, that will cause a longer path of the element and its fragments. Fragments are represented by circles whose size is proportional to the casualty area.

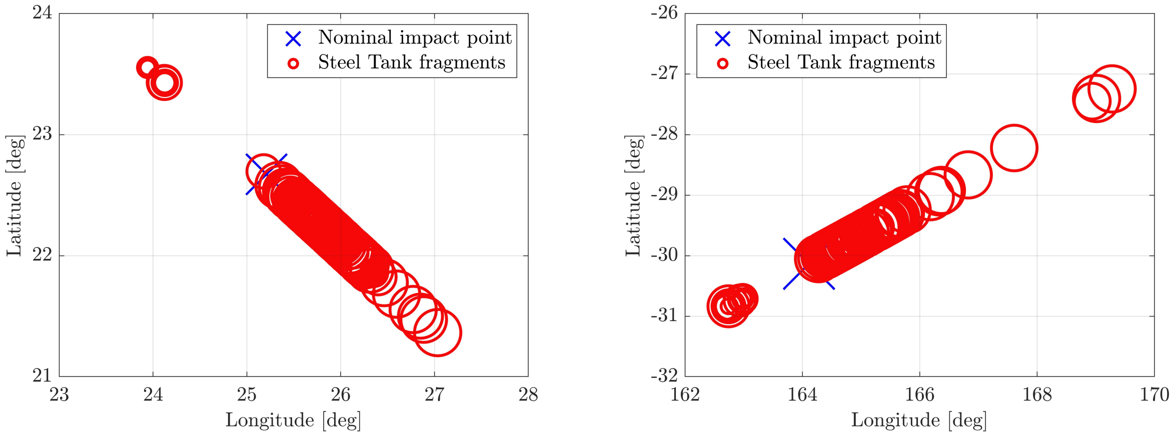

(a) Steel Tank (0.5e) (b) Steel Tank (2e)

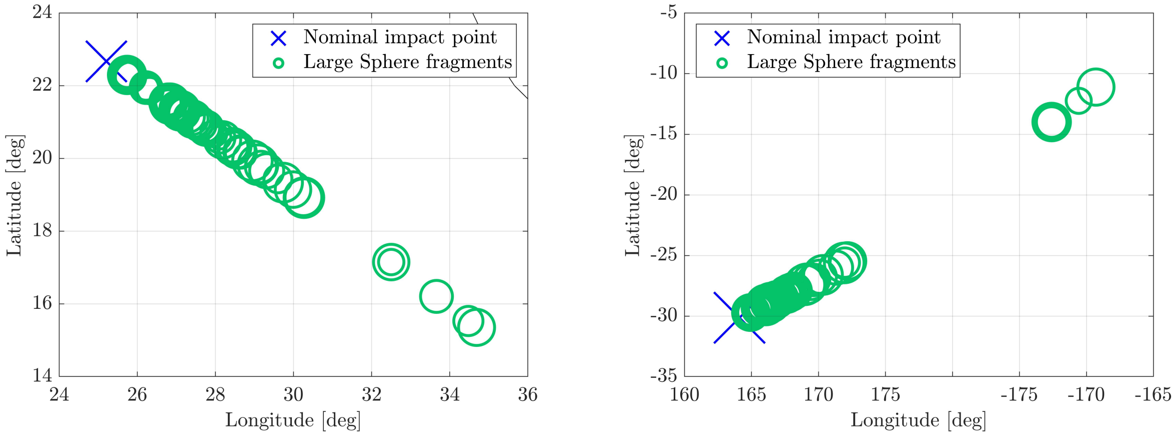

(c) Titanium Large Sphere (0.5e) (d) Titanium Large Sphere (2e)

Figure 5.64: Footprint of tank and large sphere (modified eccentricity)

5.7.2. Variation of inclination of the initial orbit

According to the location of the launch base and the mission requirements, upper stages could be released on orbits ranging from equatorial to polar. Therefore, it should be interesting to understand how the inclination of the initial orbit affects the reentry event. Without conducting a complete sensitivity analysis, this section simply halves and doubles the inclination of the orbit of the base case and runs the reentry algorithm for both cases. The modification of the inclination is done at the first passage from a nodal point after the initial point so as not to change the other orbital parameters.

Figure 5.65 shows the new obtained paths followed by the main vehicle from the last apogee to ground. The base case (Figure 5.4a) has an inclination of 41.03 deg and the latitude band overflown is accordingly halved in the first case and doubled in the second one. The location of the point at which the altitude of $120km$ is crossed remains nearly the same. Instead, impact point location is shifted both in longitude and latitude. In particular, the reduced inclination case brings to higher positive latitudes while the augmented one brings to negative latitudes. These effects are well explained by Figure 5.66, in which the altitude profile of each case is plotted against the other. The time that the vehicle takes to go from the last apogee to ground is almost the same among the three cases, but the case with half inclination takes less time than the base case, so the impact is located before on the path and this is why there is a shift towards west and higher altitudes. Regarding the case with double inclination, the longer time to impact produces a shift towards negative latitudes, while the shape of the orbit causes again a westward drift of the impact point.

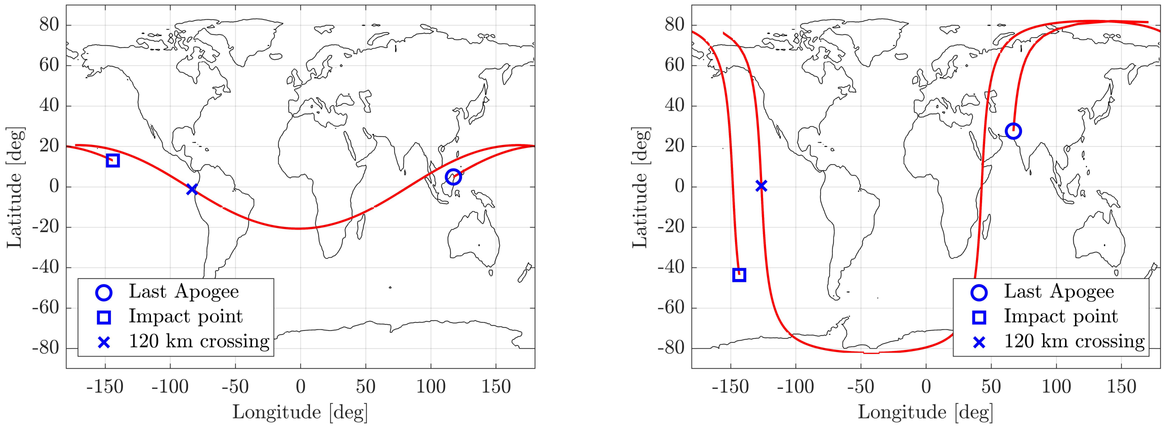

(a) Half inclination (b) Double inclination

Figure 5.65: Ground track from last apogee to ground (modified inclination)

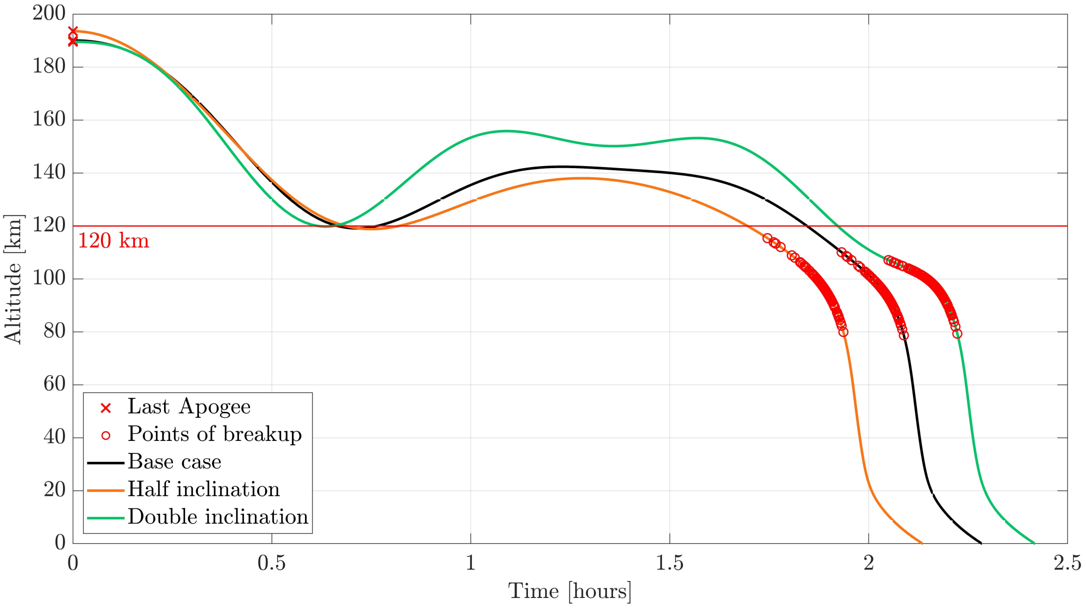

Figure 5.66: Altitude profile from the last apogee to ground (modified inclination)

The overall time from initial point to ground is almost the same in the three cases, while the reduced inclination case brings to one orbital revolution less than the base case and vice versa for the augmented inclination case. In the graph, the distribution of breakup points is moved towards higher altitudes for the reduced inclination case and vice versa for the augmented inclination case. This behaviour is analyzed in the histograms of Figure 5.67, which compare the breakup altitude distributions among the three different inclinations. Actually, also the double eccentricity case redistributes the probability towards higher breakup altitudes.

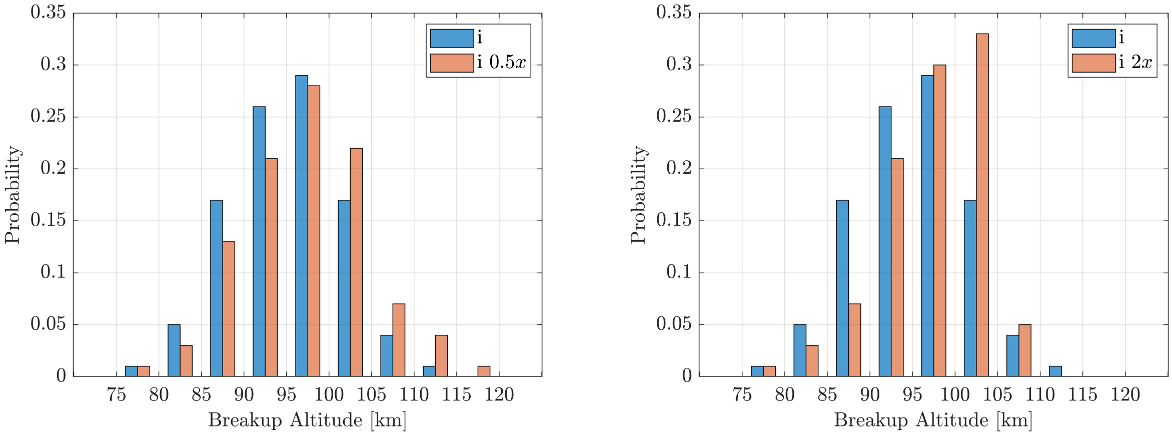

(a) Half inclination

(b) Double inclination

Figure 5.67: Breakup altitude (modified inclination)

The outcomes of the reentry analysis are reported in Figures 5.68 and 5.69 for the steel tank and titanium large sphere elements.

The distributions of casualty area of each element remain almost the same with no significant variation in the probability of each range. Only the maximum value of area for the tank is reduced from almost $20m^2$ to almost $15m^2$ in both cases, probably due to a reduced fragmentation.

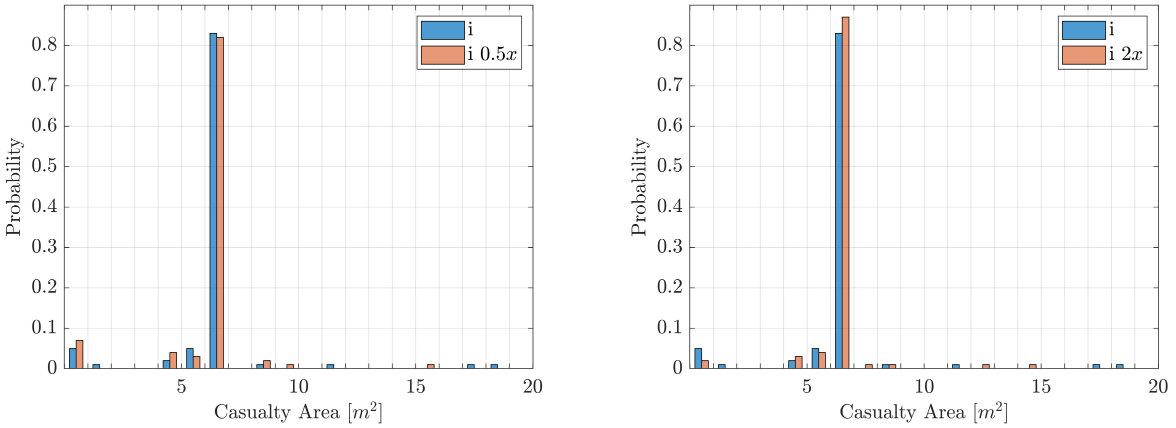

(a) Steel Tank (0.5i) (b) Steel Tank (2i)

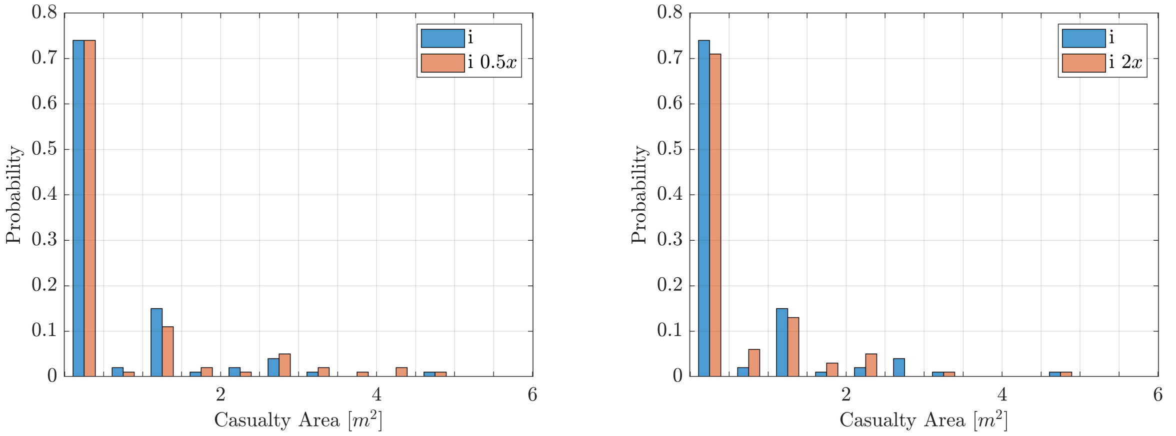

(c) Titanium Large Sphere (0.5i) (d) Titanium Large Sphere (2i)

Figure 5.68: Casualty area of tank and large sphere (modified inclination)

Regarding the footprint dispersions of the fragments of each element, it is not possible to compare them due to different locations of the nominal impact point and also due to different inclination of the path. However, footprints have almost the same dispersion among the two cases and there is also a similarity with the ones of the base case (Figure 5.17a and 5.17b). In fact, the bulk of the fragments is again near the nominal point and the large sphere presents an augmented dispersion after the nominal point. Fragments are represented by circles whose size is proportional to the casualty area.

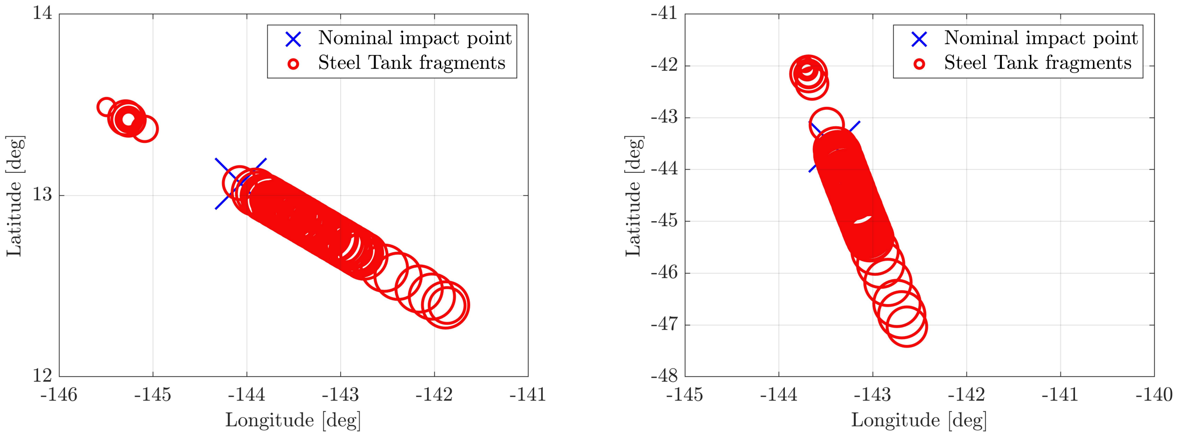

(a) Steel Tank (0.5i)

(b) Steel Tank (2i)

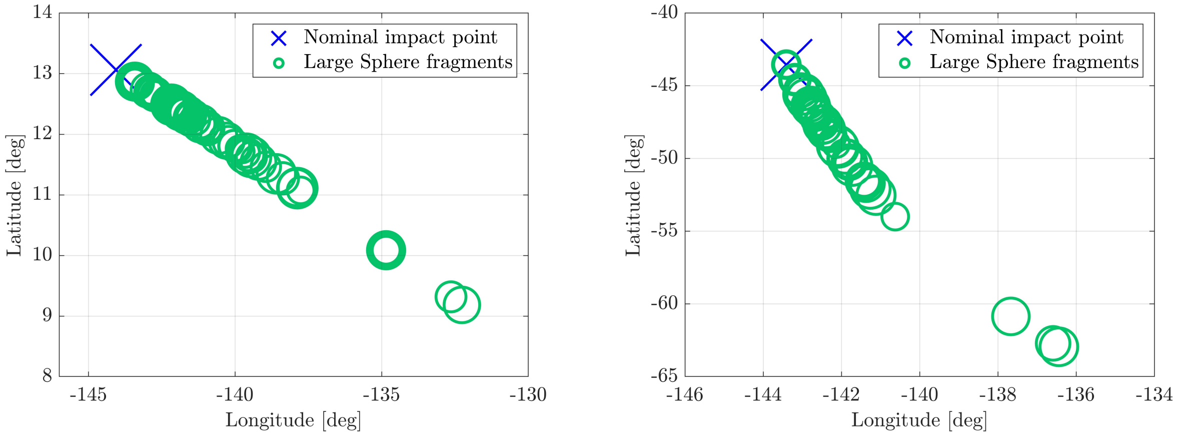

(c) Titanium Large Sphere (0.5i)

(d) Titanium Large Sphere (2i)

Figure 5.69: Footprint of tank and large sphere (modified inclination)

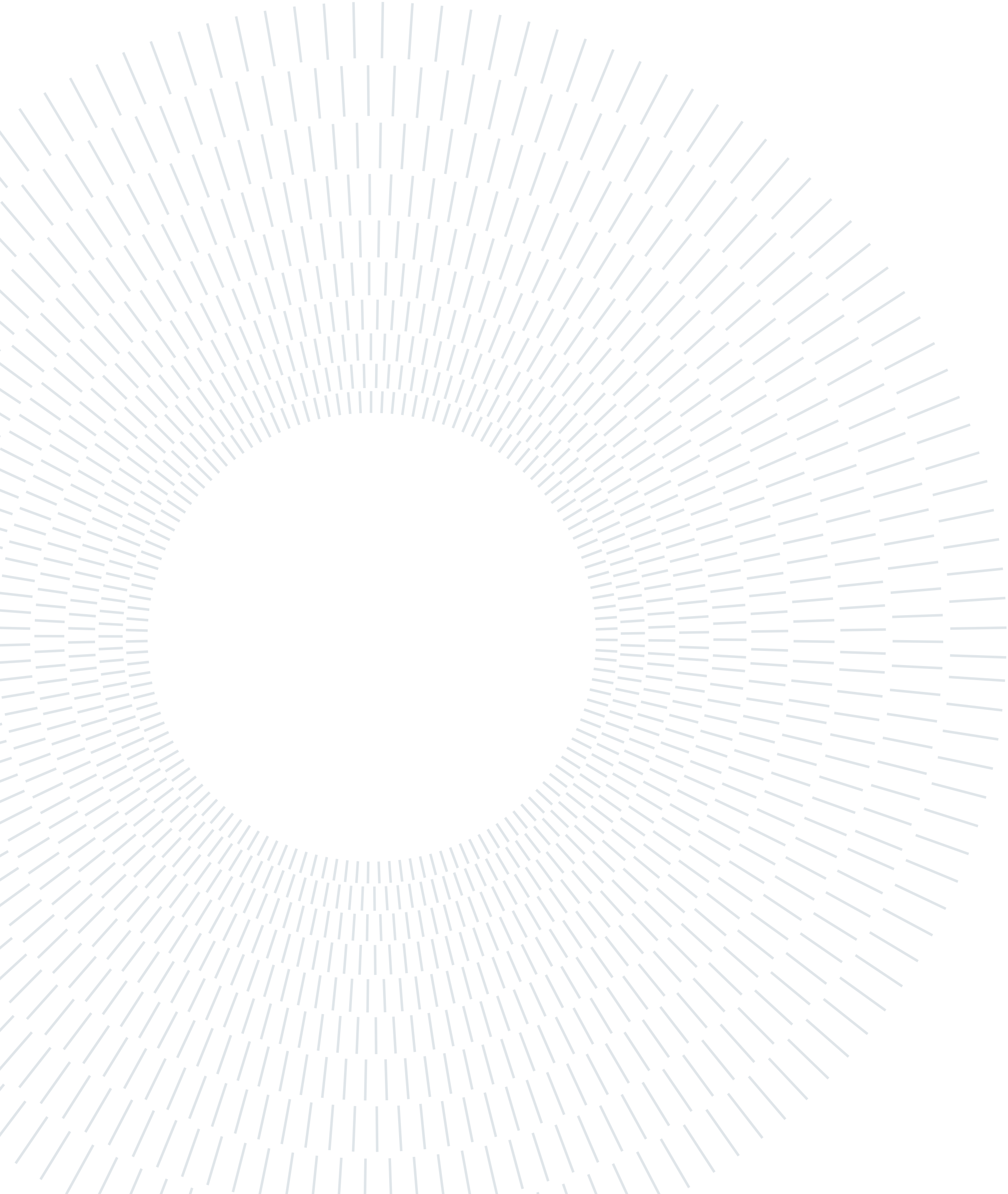

6 | Conclusions and future developments

The algorithm developed in this thesis is able to estimate the probability distributions of casualty area and casualty expectancy associated to a reentry event and the footprint dispersion of impacting fragments, replacing common assumptions with uncertainty distribution on main parameters. The inclusion of uncertainties treatment enables the investigation of different reentry scenarios and extends the range of applicability of the reentry algorithm to various categories or assemblies of space objects and to various types of orbit.

The simulation framework has been applied to the analysis of the reentry of an upper stage vehicle that resume the characteristic of the Delta II second stage. Obtained results are in agreement with distributions available in literature and could be used to understand the most probable and hazardous impact regions, so that further detailed analysis can be done to refine the risk estimations.

One of the most interesting contribution of the thesis is the combination of breakup model and location of impact points. The breakup model considers a fictitious structural element that drives the separation of all the other components, representing what actually happens after the main breakup. The impact points are the outcomes of a propagator dedicated to reentry trajectory determination. In such a way, it is possible to quantify the casualty expectancy associated to a certain geographical area on the Earth.

Moreover, the implemented algorithm could be used for different purposes and it has been applied to the development of a detailed sensitivity analysis on main parameters, such as melt temperatures, heat transfer orientation factors, material emissivity and drag coefficient. The results of the sensitivity analysis highlight the importance of the orientation factor in determining the net heat flux over a falling object and so the consequent thermal behaviour. As well, the modeling of the structure element is crucial in this algorithm, since it directly affects the range of breakup altitudes and so all the following events. In fact, correlations have been found between fusion altitude of the structure and the main outcomes of the reentry.

Each performed simulation is composed by one-hundred trials. This value was selected as a compromise between the width of the range of results in terms of statistical validity and the time needed to perform calculations. Then, a simulation on 5 elements takes about 3 hours to run on a platform with a moderate configuration (Intel i7 dual core and 16 GB of RAM).

Of course, there are many aspects to improve. The orientation factor parameter is dependent mainly on the attitude, that also varies during the reentry. Since the adopted model considers the object as a point mass for the aerodynamic point of view, the attitude is not computed, and so the orientation factor is represented by a generic distribution that should be improved by experimental data or simply by performing more simulations on objects with different shape and size with the scope of customizing the range of values. Therefore, the first future development should be a simulation campaign on different categories of space vehicle with a number of trials at least ten times greater than the one used till now. Also the vehicle model could be improved considering the possibility that elements once broken could release internal components, such as for example the guidance box element. Finally, the obtained footprint develops only in the down-range direction. Thus, the possibility of the cross-range dispersion could be included accounting the effects of aerodynamic force on each side of an element, therefore computing the attitude of an element, and also including the effects of winds. Such contribution would produce a lateral deviation in the trajectories.

The ultimate goal of an effective probabilistic approach would be a campaign of simulations that accounts for all the possible reentry cases of a certain category of space vehicle, in order to fill in a sort of database with all the outcomes after each reentry. Then, the available data could be exploited to build an overall probability distribution that directly relates a set of initial conditions to the final results.

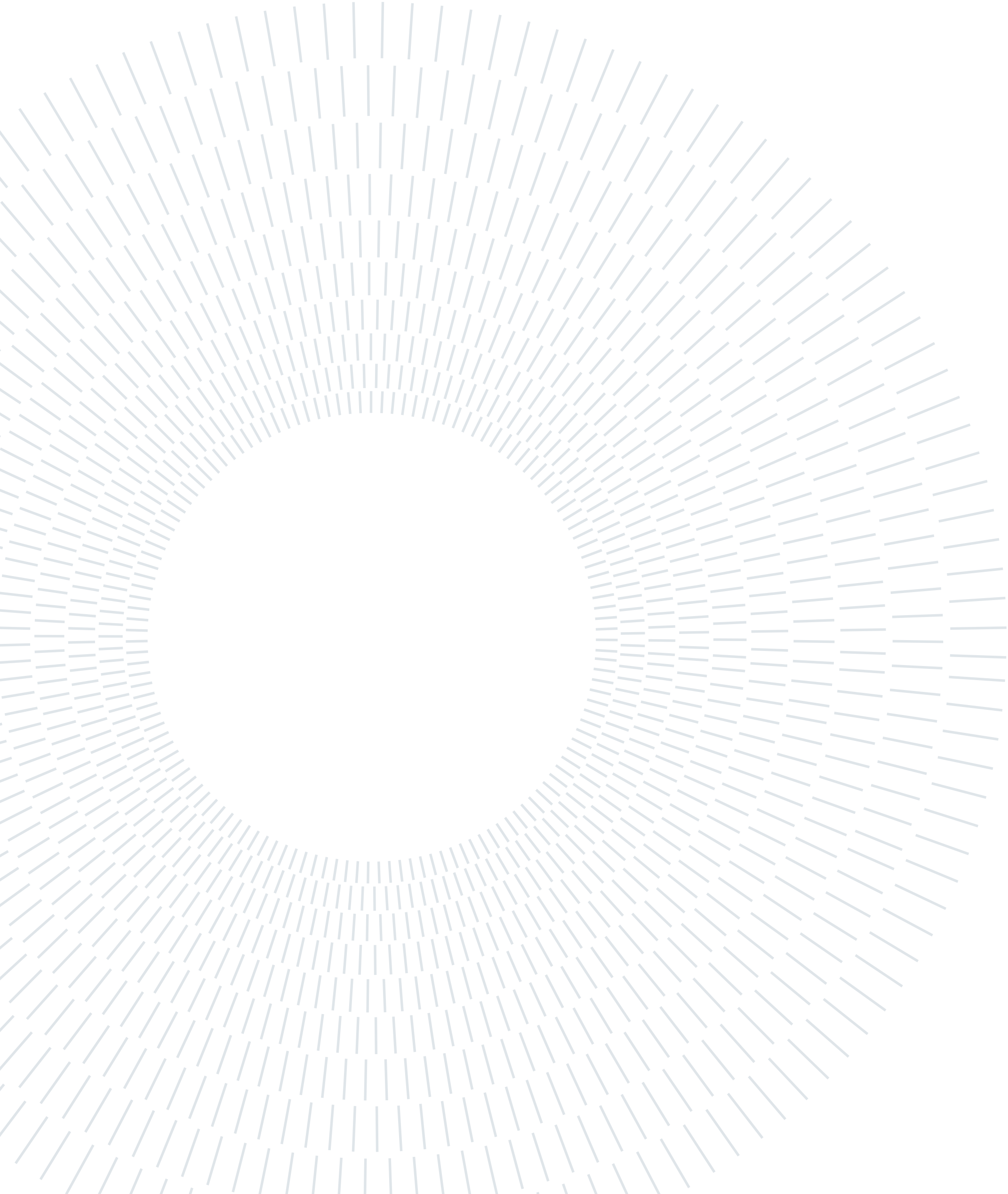

Bibliography

[1] C. Pardini and L. Anselmo. Reentry predictions for uncontrolled satellites: results and challenges. Italian National Research Council, May 2013.

[2] M. V. Frank, M. A. Weaver, and R. L. Baker. A probabilistic paradigm for spacecraft random reentry disassembly. *Reliability Engineering and System Safety*, 90:148–161, 2005.

[3] I. Pontijas Fuentes, D. Bonetti, F. Letterio, G. Vicario de Miguel, G. B. Arnao, P. Palomo, C. Parigini, S. Lemmens, T. Lips, and R. Kanzler. Upgrade of ESA's Debris Risk Assessment and Mitigation Analysis (DRAMA) tool: Spacecraft Entry Survival Analysis Module. *Acta Astronautica*, 158:148–160, 2019.

[4] Bent Fritsche, Heiner Klinkrad, Alexander V. Kashkovsky, and Eduard I. Grinberg. Spacecraft disintegration during uncontrolled atmospheric re-entry. *Acta Astronautica*, 47:513–522, 1997.

[5] T. Lips. Equivalent Re-Entry Breakup Altitude and Fragment List. 2013.

[6] M. Reyhanoglu and J. A. Alvarado. Estimation of debris dispersion due to a space vehicle breakup during reentry. *Acta Astronautica*, 86:211–218, 2013.

[7] A. Falsone and F. Noce. A randomized approach to the prediction of critical situations for air traffic due to uncontrolled space debris reentry. 2013.

[8] Siwoo Kim, Byeong Un Jo, Eun Jung Choi, Sungki Cho, and Jaemyung Ahn. Two-phase framework for footprint prediction of space object reentry. *Advances in Space Research*, 2019.

[9] M. Trisolini and C. Colombo. Modeling re-entry break-up uncertainties with continuity equation and gaussian mixture models interpolation. In *2020 AAS/AIAA Astrodynamics Specialist Conference*, volume AAS 20-636, 2021.

[10] R. B. Mrozinski, G. F. Mendeck, and R. M. Cutri-Kohart. Overview of entry risk predictions. *Advances in Space Research*, 34:1044–1048, 2002.

[11] Nasa. Nasa safety standard: Guidelines and assessment procedures for limiting orbital debris. 2019.

[12] Paul D. Wilde and Christopher H Draper. Aircraft protection standards and implementation guidelines for range safety. 2010.

[13] A. Morselli, R. Armellin, P. Di Lizia, and F. Bernelli Zazzera. Computation of Collision Probabilities Based on Special Perturbations and High Order Methods. 2013.

[14] J. T. Emmert, D. P. Drob, J. M. Picone, D. E. Siskind, M. Jones, M. G. Mlynczak, P. F. Bernath, Xinzhao Chu, E. Doornbos, B. Funke, L. P. Goncharenko, M. E. Hervig, M. J. Schwartz, P. E. Sheese, F. Vargas, B. P. Williams, and Tao Yuan. NRLMSIS 2.0: A Whole-Atmosphere Empirical Model of Temperature and Neutral Species Densities. *Earth and Space Science*, 8, 2020.

[15] N. K. Pavlis, S. A. Holmes, and S. C. Kenyon. The development and evaluation of the Earth Gravitational Model 2008 (EGM2008). *Journal of Geophysical Research*, 117, 2012.

[16] L. F. Crabtree, J. G. Woodley, and R. L. Dommett. *Estimation of Heat Transfer to Flat Plates, Cones and Blunt Bodies.* Aeronautical Research Council, 1970.

[17] L. L. Perini. Compilation and correlation of stagnation convective heating rates on spherical bodies. *Journal of Spacecraft and Rockets*, 12:189–191, 1975.

[18] S. H. Park, D. Neeb, G. Plyushchev, P. Leyland, and A. Gülhan. A study on heat flux predictions for re-entry flight analysis. *Acta Astronautica*, 187:271–280, 2021.

[19] NASA. Stagnation Temperature - Real Gas Effects. URL `https://www.grc.nasa.gov/www/BGH/stagtmp.html`. Accessed: 2021-09-30.

[20] G. L. Steckel and P. M. Adams. Evaluation of Reentry Effects of Delta II Second Stage Propellant Tanks. Technical report, Space and Missile Systems Center Air Force Space Command, March 2018.

[21] B.T.C. Zandbergen. Modern Liquid Propellant Rocket Engines. Technical report, TU-DELFT, May 2000.

[22] L. O. Cropp. *Analytical Methods Used in Predicting the Re-Entry Ablation of Spherical and Cylindrical Bodies.* 1965.

[23] M. A. Weaver, R. L. Baker, and M. V. Frank. Probabilistic estimation of reentry debris area. 2001.

[24] W. H. Ailor, W. K. Hallman, G. L. Steckel, and M. L. Weaver. Analysis of reentered debris and implications for survivability modeling. 2005.

[25] Willem J. Botha. Orbital debris: a case study of an impact event in south africa. 2001.

[26] Center for International Earth Science Information Network CIESIN Columbia University. Gridded Population of the World, Version 4 (GPWv4): Population Density, Revision 11, 2018. URL `https://doi.org/10.7927/H49C6VHW`. Accessed: February 2022.

[27] B. Fritsche, T. Lips, and G. Koppenwallner. Analytical and numerical re-entry analysis of simple-shaped objects. *Acta Astronautica*, 60:737–751, 2007.

[28] George E. Apostolakis. The concept of probability in safety assessments of technological systems. *Science*, 250 4986:1359–64, 1990.

[29] V. S. Aslanov and D. A. Sizov. A spent upper stage removal mission aimed to reduce debris impact footprint size. *Acta Astronautica*, 168:23–30, 2020.

[30] C. Pardini and L. Anselmo. Uncontrolled re-entries of spacecraft and rocket bodies: A statistical overview over the last decade. *Journal of Space Safety Engineering*, 2019.

[31] H. Klinkrad. Assessment of the on-ground risk during re-entries. 2001.

[32] R. P. Patera. Hazard Analysis for Uncontrolled Space Vehicle Reentry. *Journal of Spacecraft and Rockets*, 45:1031–1041, 2008.

[33] M. S. Surratt, M. T. Kerizian, and T. Sgobba. A novel method for prediction and warning for uncontrolled re-entry object impact. *Journal of Space Safety Engineering*, 2:51–56, 6 2015.

[34] WU Ziniu, Hu Ruifeng, Qu Xi, Wang Xiangb, and Wu Zhea. Space Debris Reentry Analysis Methods and Tools. *Chinese Journal of Aeronautics*, 24:387–395, 2011.

[35] T. Lips and B. Fritsche. A comparison of commonly used re-entry analysis tools. *Acta Astronautica*, 57:312–323, 2005.

[36] P. M. Mehta, A. C. Walker, M. Brown, E. A. Minisci, and M. Vasile. Sensitivity analysis towards probabilistic re-entry modeling of spacecraft and space debris. 2015.

[37] FAA. Flight Safety Analysis Handbook. Technical report, Federal Aviation Administration, September 2011.

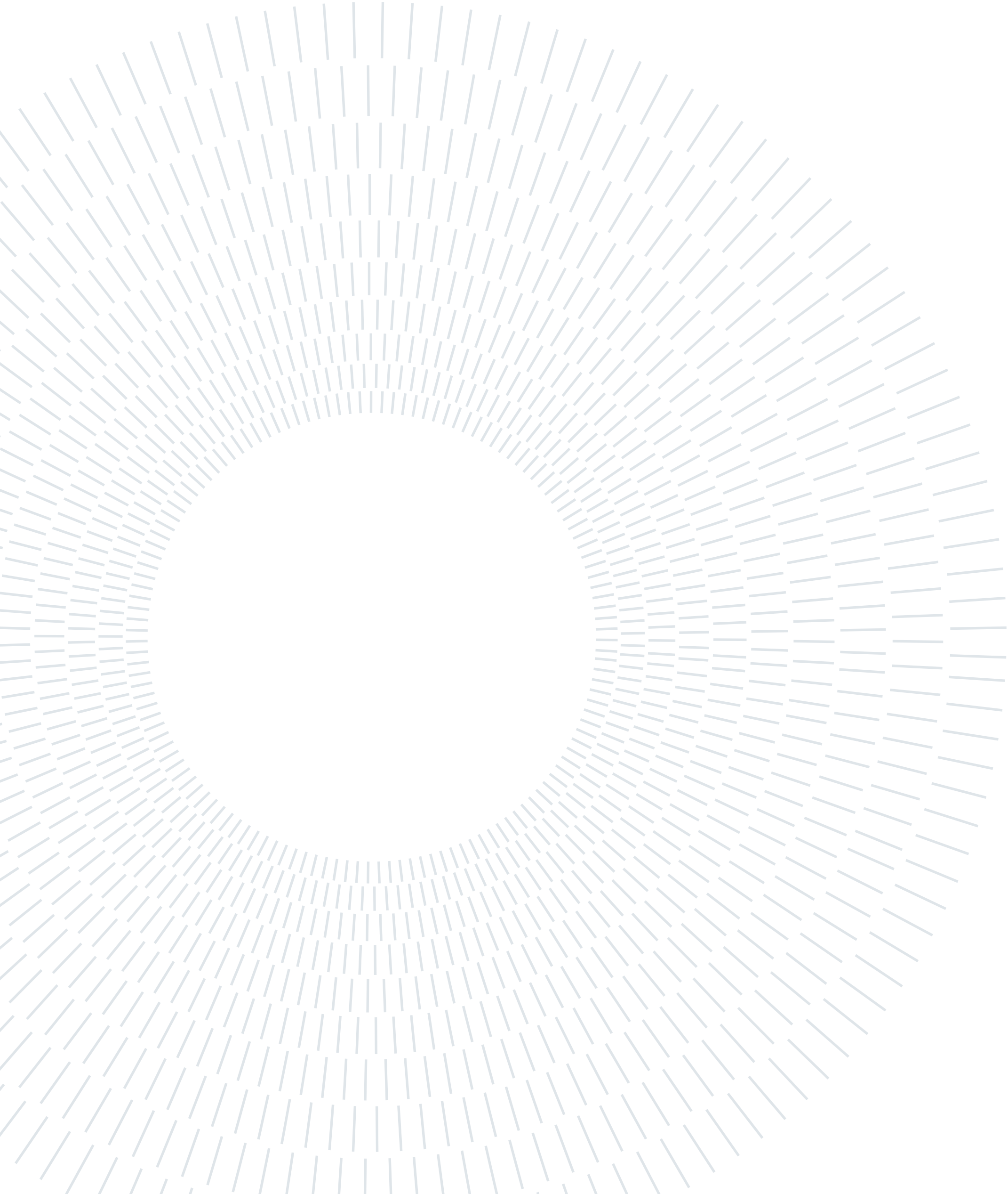

A | Outcomes of the simulations with modified drag coefficient

This appendix contains additional results for the three simulations performed for the casualty expectancy estimation in Section 5.5. Each of the following section shows the distributions of the most relevant outcomes of each reentry case: breakup altitude, total casualty area and casualty area of each element.

A.1. Case 1: 2.248

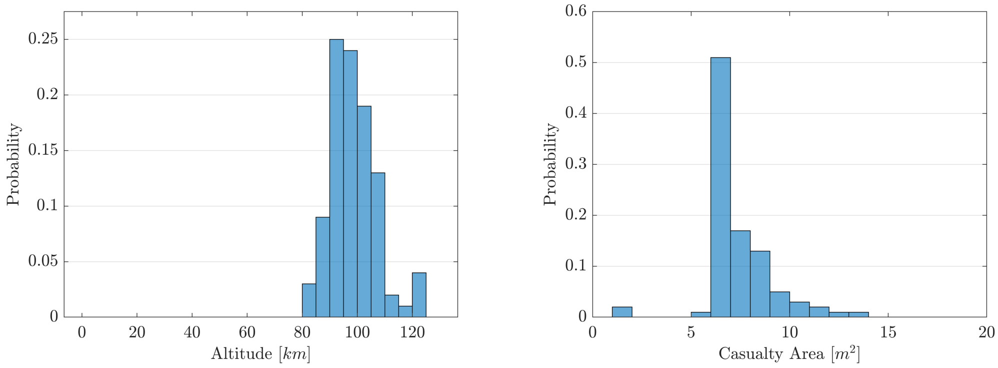

(a) Breakup altitude (b) Total Casualty Area

Figure A.1: Breakup altitude and total casualty area ($C_D = 2.248$)

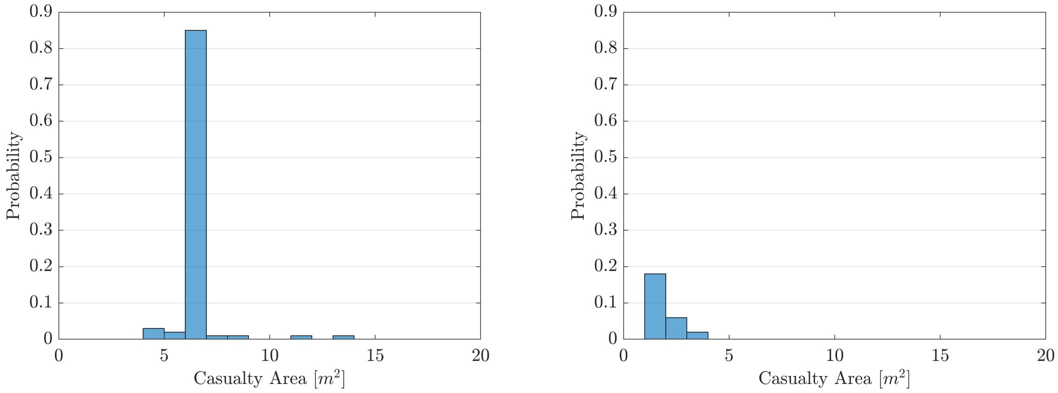

(a) Steel Tank (b) Titanium Large Sphere

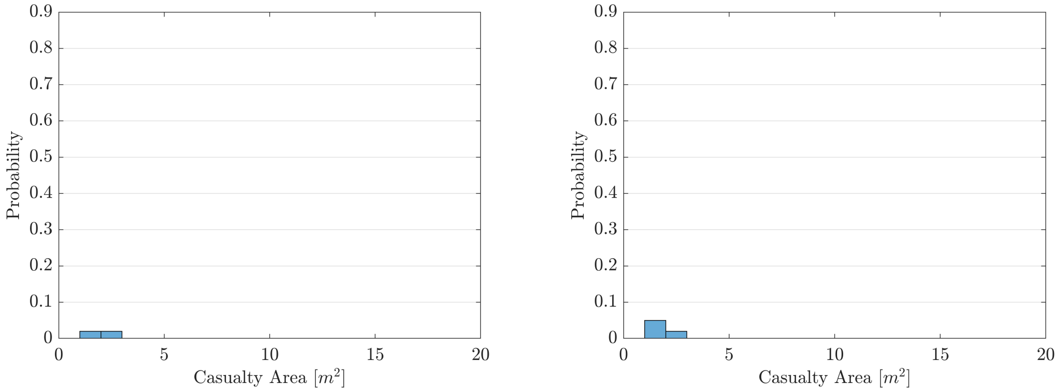

(c) Titanium Small Sphere (d) Steel Combustion Chamber

Figure A.2: Casualty area of each element ($C_D = 2.248$)

A.2. Case 2: 1.814

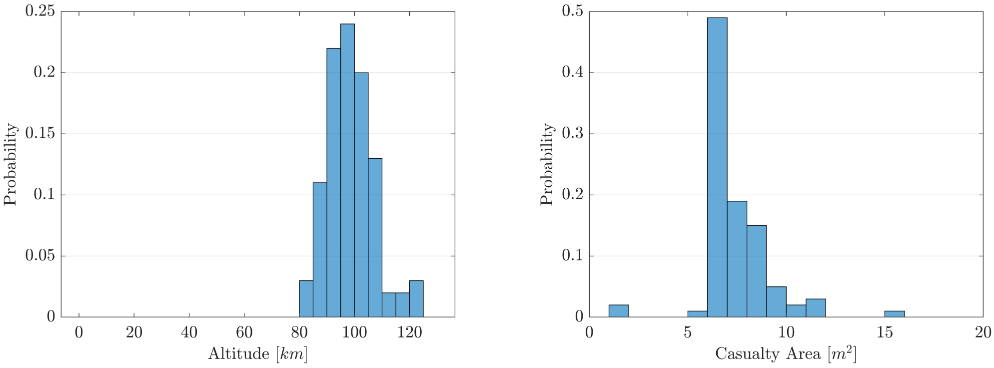

(a) Breakup altitude (b) Total Casualty Area

Figure A.3: Breakup altitude and total casualty area ($C_D = 1.814$)

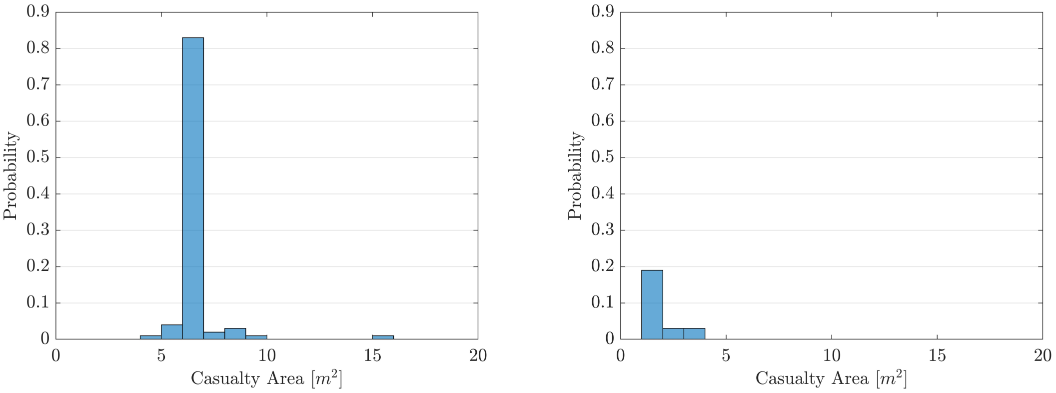

(a) Steel Tank (b) Titanium Large Sphere

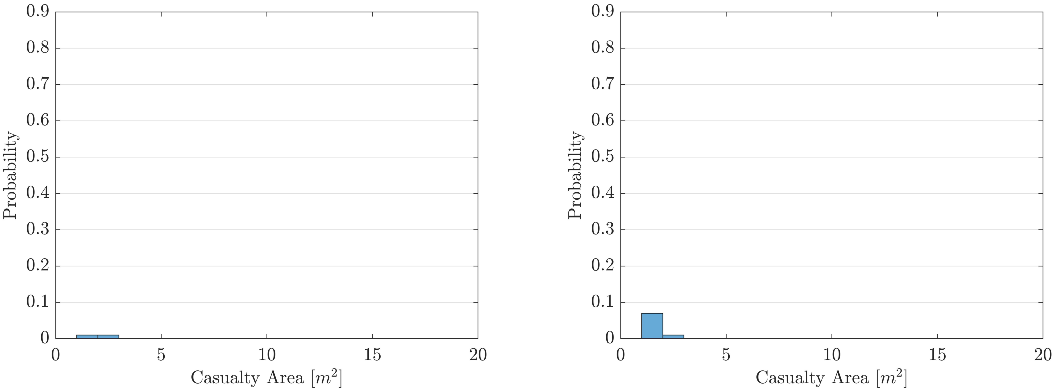

(c) Titanium Small Sphere (d) Steel Combustion Chamber

Figure A.4: Casualty area of each element ($C_D = 1.814$)

A.3. Case 3: 2.584

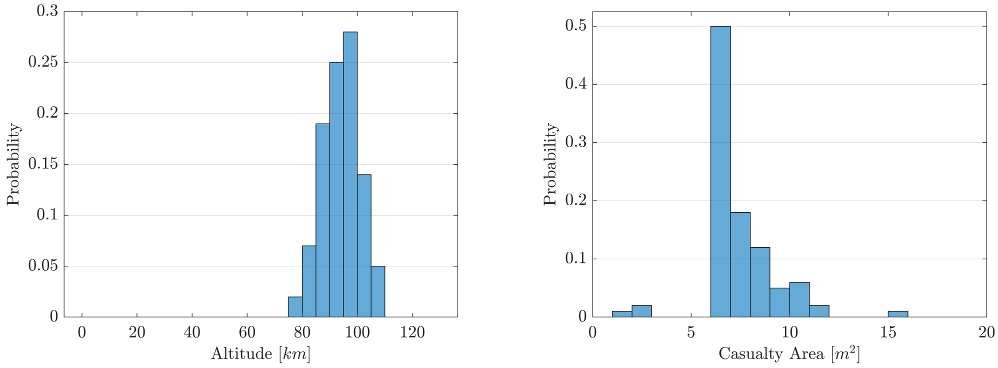

(a) Breakup altitude (b) Total Casualty Area

Figure A.5: Breakup altitude and total casualty area ($C_D = 2.584$)

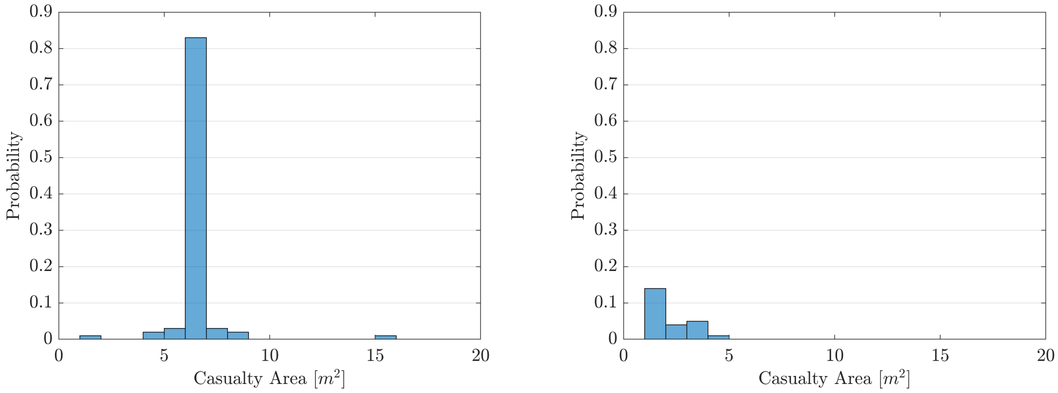

(a) Steel Tank (b) Titanium Large Sphere

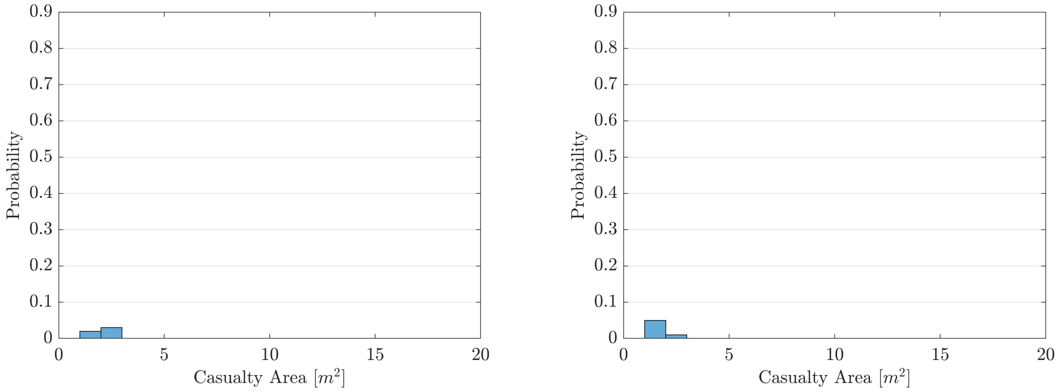

(c) Titanium Small Sphere (d) Steel Combustion Chamber

Figure A.6: Casualty area of each element ($C_D = 2.584$)

B | Sensitivity analysis on Small Sphere and Combustion Chamber

This appendix contains the results of sensitivity analysis performed on the titanium small sphere and on the steel combustion chamber.
As in Section 5.6, only the most significant graphs are reported.
For practical purpose, the names of the elements are sometimes abbreviated as SS for the small sphere and CC for the combustion chamber.

B.1. Sensitivity to structure fusion temperature

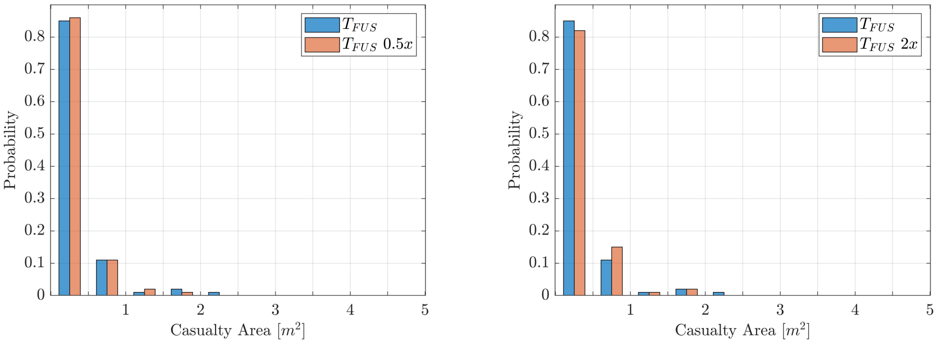

(a) Half standard deviation (SS)   (b) Twice standard deviation (SS)

Figure B.1: Sensitivity of casualty area to fusion temperature of the structure

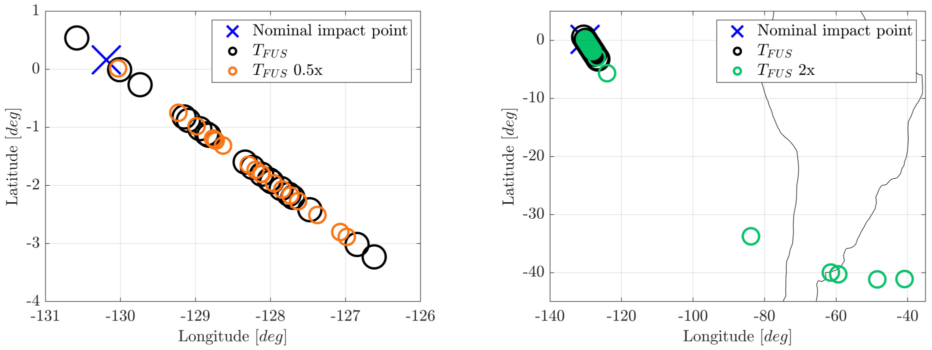

(a) Half standard deviation (SS)   (b) Twice standard deviation (SS)

Figure B.2: Sensitivity of footprint to fusion temperature of the structure

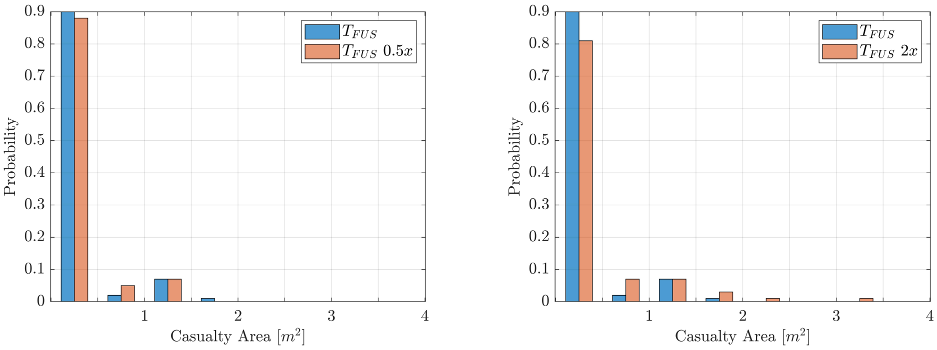

(a) Half standard deviation (CC)   (b) Twice standard deviation (CC)

Figure B.3: Sensitivity of casualty area to fusion temperature of the structure

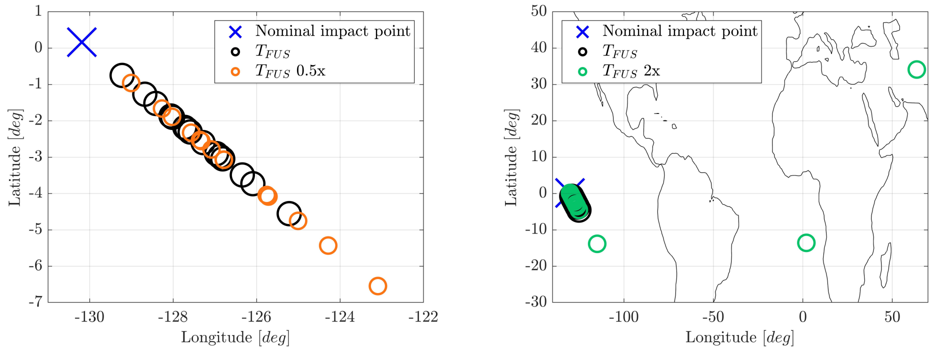

(a) Half standard deviation (CC)

(b) Twice standard deviation (CC)

Figure B.4: Sensitivity of footprint to fusion temperature of the structure

B.2. Sensitivity to structure orientation factor

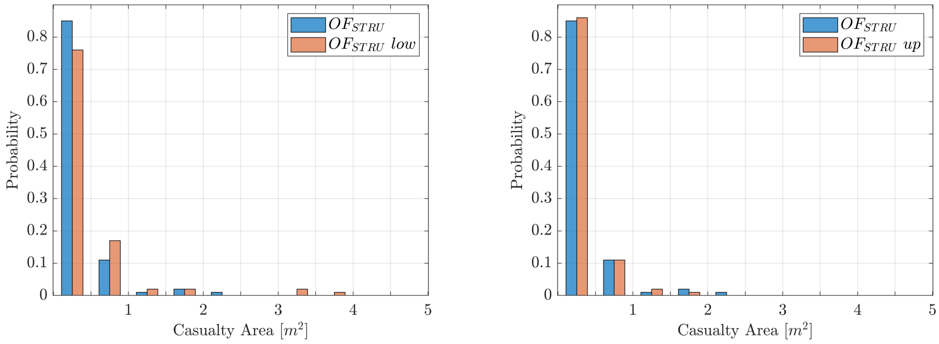

(a) Lower bound (SS)

(b) Upper bound (SS)

Figure B.5: Sensitivity of casualty area to Orientation Factor of the structure

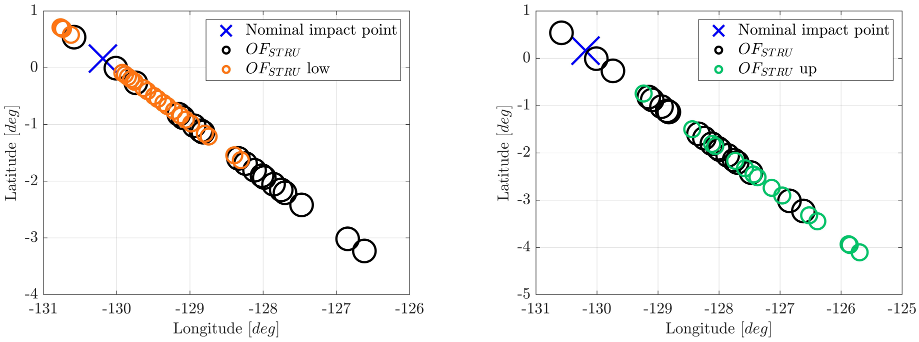

(a) Lower bound (SS)

(b) Upper bound (SS)

Figure B.6: Sensitivity of footprint to Orientation Factor of the structure

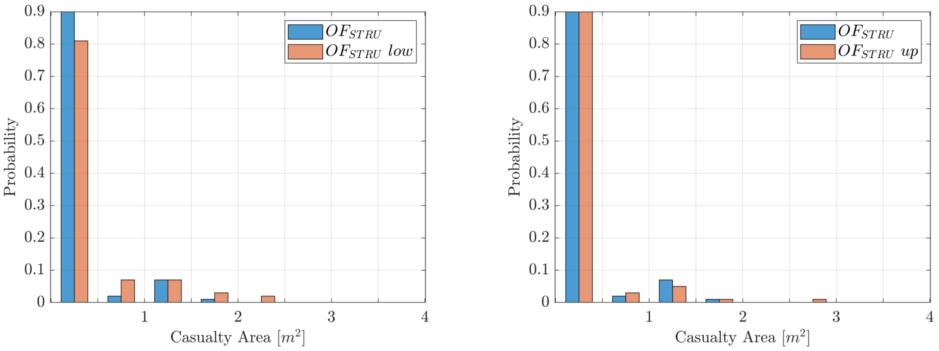

(a) Lower bound (CC) (b) Upper bound (CC)

Figure B.7: Sensitivity of casualty area to Orientation Factor of the structure

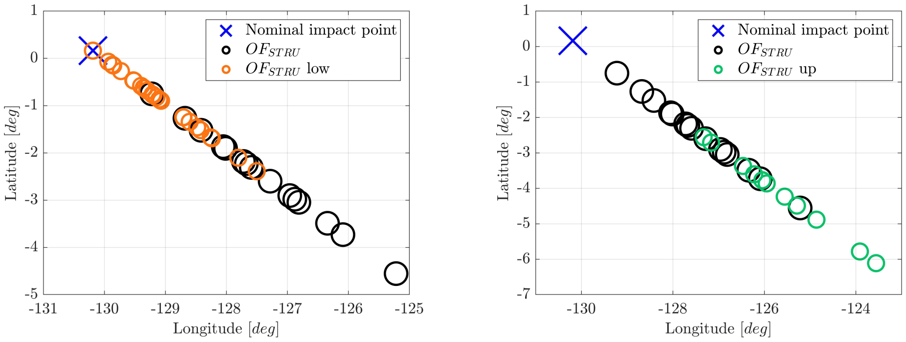

(a) Lower bound (CC) (b) Upper bound (CC)

Figure B.8: Sensitivity of footprint to Orientation Factor of the structure

B.3. Sensitivity to element fusion temperature

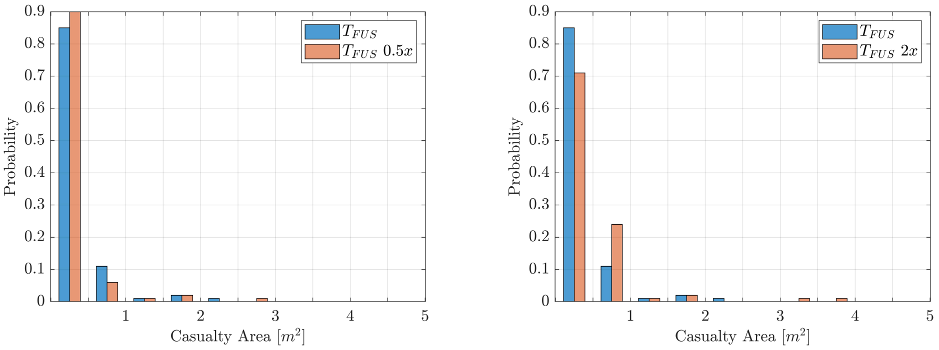

(a) Half standard deviation (b) Twice standard deviation

Figure B.9: Sensitivity of casualty area to fusion temperature (Small Sphere)

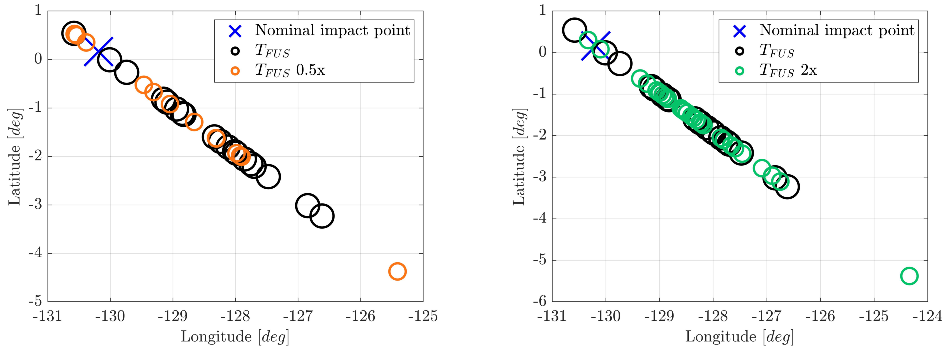

(a) Half standard deviation (b) Twice standard deviation

Figure B.10: Sensitivity of footprint to fusion temperature (Small Sphere)

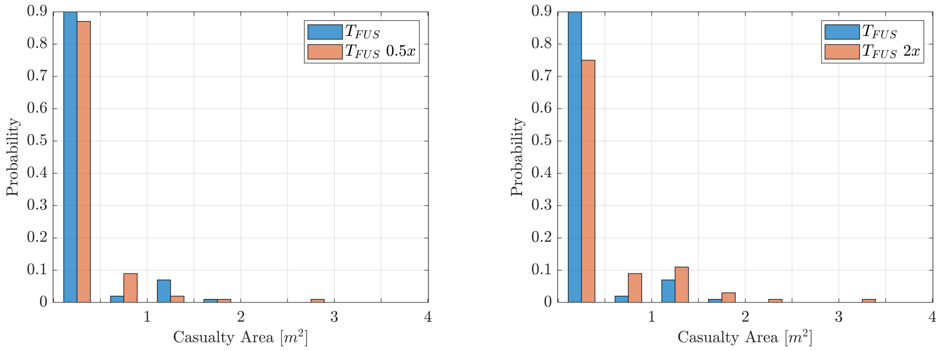

(a) Half standard deviation (b) Twice standard deviation

Figure B.11: Sensitivity of casualty area to fusion temperature (Combustion Chamber)

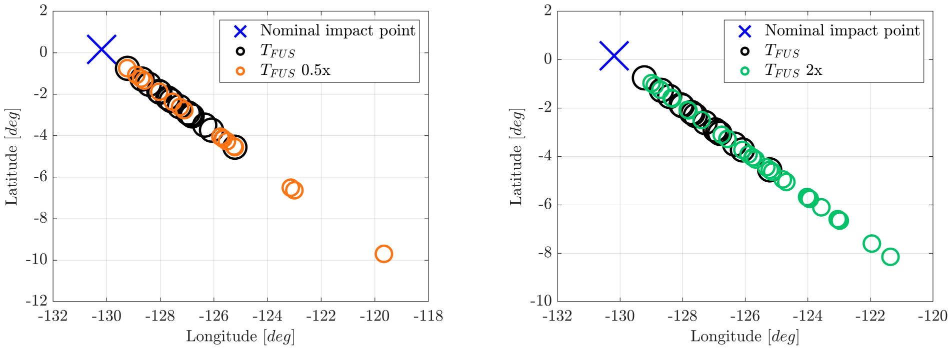

(a) Half standard deviation (b) Twice standard deviation

Figure B.12: Sensitivity of footprint to fusion temperature (Combustion Chamber)

B.4. Sensitivity to element orientation factor

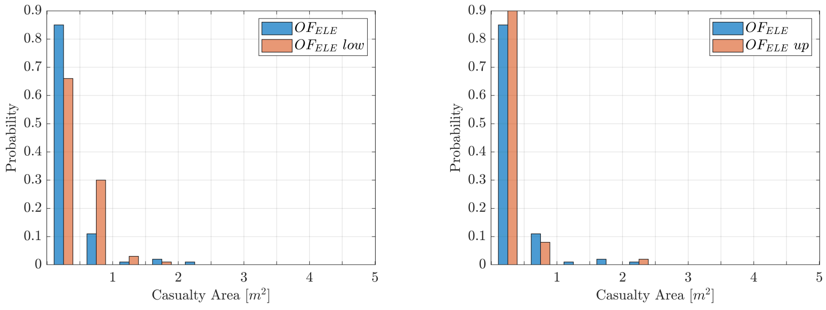

(a) Lower bound (b) Upper bound

Figure B.13: Sensitivity of casualty area to Orientation Factor (Small Sphere)

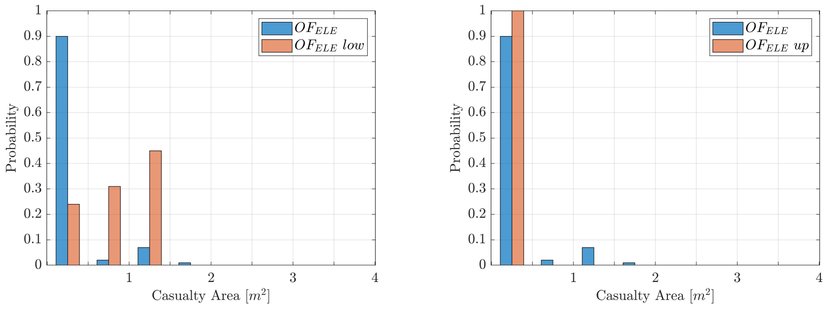

(a) Lower bound (b) Upper bound

Figure B.14: Sensitivity of casualty area to Orientation Factor (Combustion Chamber)

B.5. Sensitivity to drag coefficient of the element

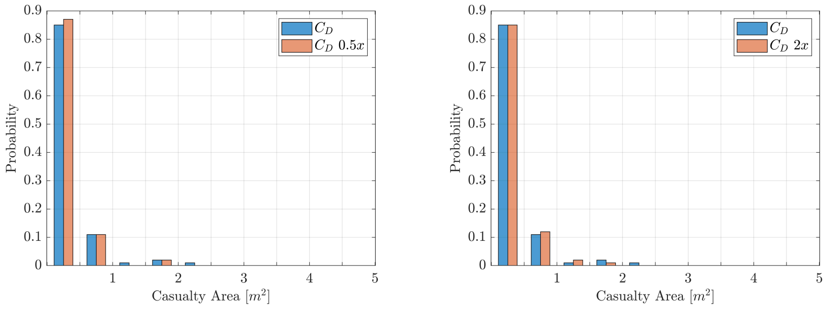

(a) Half standard deviation (b) Twice standard deviation

Figure B.15: Sensitivity of casualty area to drag coefficient (Small Sphere)

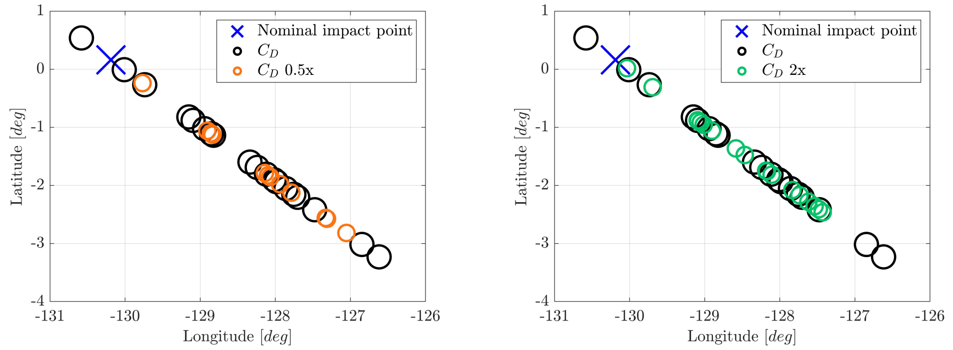

(a) Half standard deviation (b) Twice standard deviation

Figure B.16: Sensitivity of footprint to drag coefficient (Small Sphere)

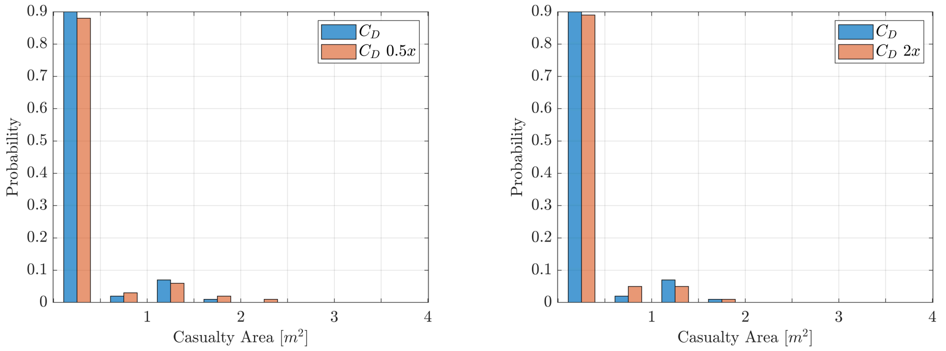

(a) Half standard deviation (b) Twice standard deviation

Figure B.17: Sensitivity of casualty area to drag coefficient (Combustion Chamber)

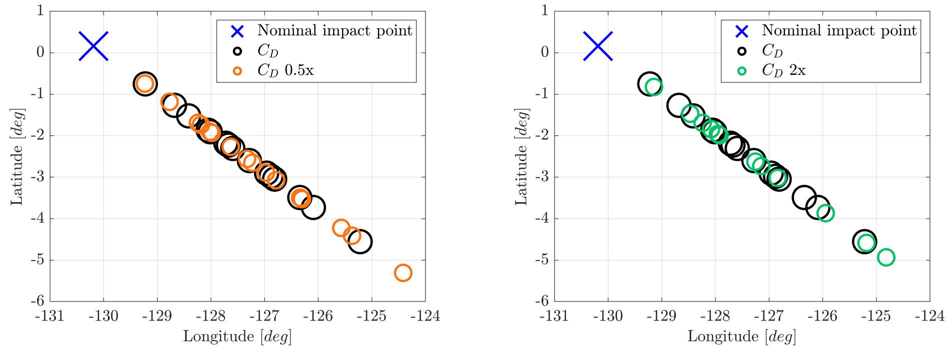

(a) Half standard deviation (b) Twice standard deviation

Figure B.18: Sensitivity of footprint to drag coefficient (Combustion Chamber)

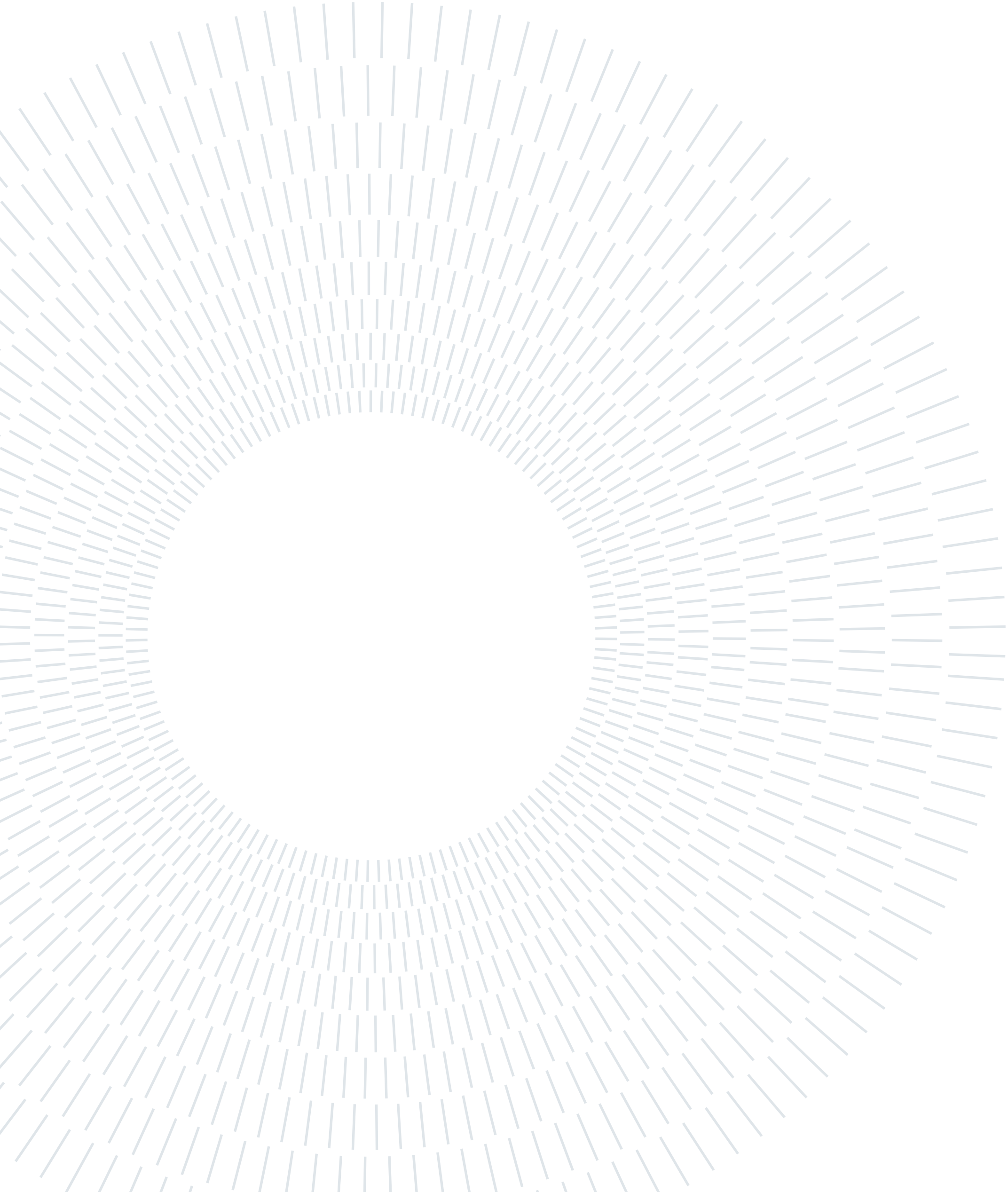

List of Figures

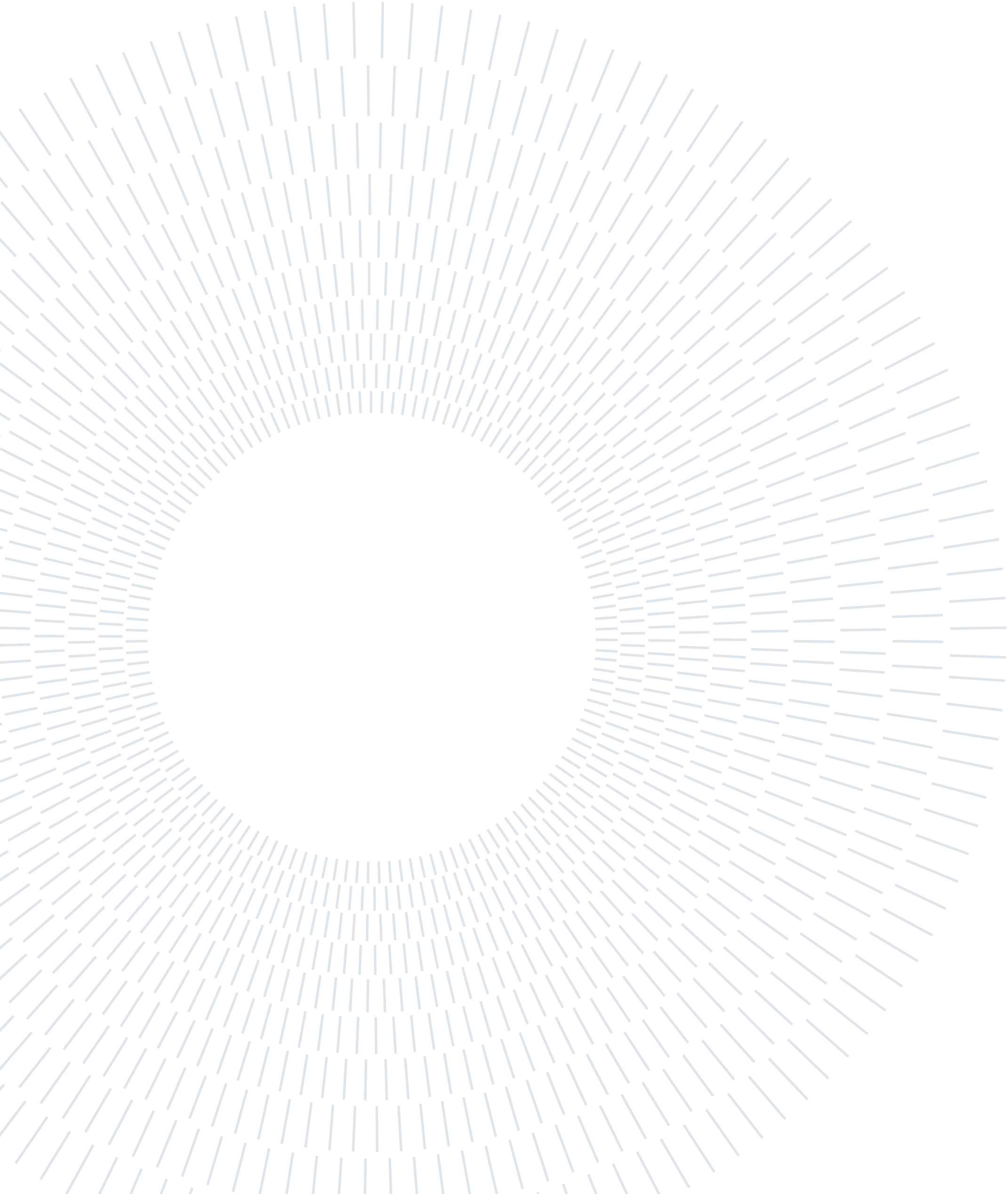

List of Tables

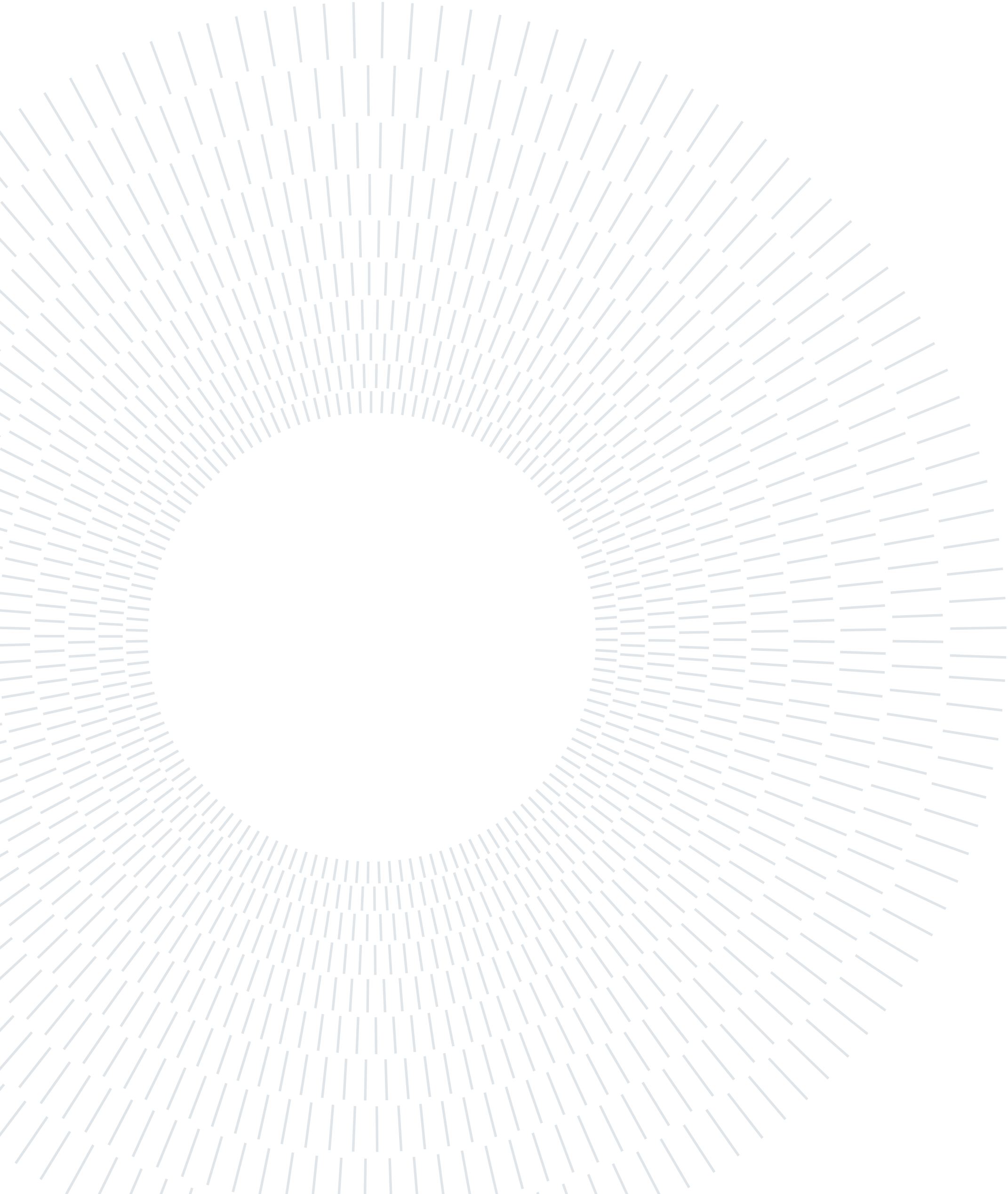

List of Symbols

Variable	Description	SI unit
$\boldsymbol{A}_C$	casualty area	m^2
$\boldsymbol{A}_{cross}$	area of the cross section	m^2
$\boldsymbol{A}_{tot}$	external surface of an item	m^2
$\boldsymbol{C}_D$	drag coefficient	-
$\boldsymbol{e}$	eccentricity of the orbit	-
$\boldsymbol{E}_C$	casualty expectancy	-
$\boldsymbol{\varepsilon}$	emissivity	-
$\boldsymbol{h}_{conv}$	coefficient of convective heat transfer	-
$\boldsymbol{h}_{FUS}$	altitude at which an item reaches the melt temperature	km
$\boldsymbol{i}$	inclination of the orbit	deg
$\dot{\boldsymbol{m}}$	mass rate due to ablation	$\frac{kg}{s}$
$\boldsymbol{M}_{fin}$	final mass of an item	kg
$\boldsymbol{n}_{max}^{frag}$	maximum number of potential fragments	-
$\boldsymbol{OF}$	heat transfer orientation factor	-
$\boldsymbol{OF}_{ELE}$	heat transfer orientation factor of an element	-
$\boldsymbol{OF}_{STRU}$	heat transfer orientation factor of the structure	-
$\boldsymbol{P}_i$	probability of i event	-
$\boldsymbol{Q}_{flux}$	net heat flux	$\frac{J}{s}$
$\boldsymbol{\sigma}$	standard deviation	-
$\dot{\boldsymbol{T}}$	temperature rate due to heating	$\frac{K}{s}$
$\boldsymbol{T}_{FUS}$	fusion temperature	K
$\boldsymbol{t}_{SEP}$	separation (breakup) instant	s
$\boldsymbol{V}$	magnitude of the velocity vector	$\frac{km}{s}$